AD-A272 446

(2)

PL-TR-93-2131

ANALYSIS OF THE EFFECTS OF EURASIAN CRUSTAL AND UPPER MANTLE STRUCTURE ON REGIONAL PHASES USING BROADBAND SEISMIC DATA

Jos Beckers
Susan Schwartz
Thorne Lay

University of California, Santa Cruz
Institute of Tectonics
Santa Cruz, CA 95064

8 June 1993

Final Report
July 1990 - March 1993

Approved for public release; distribution unlimited

PHILLIPS LABORATORY
Directorate of Geophysics
AIR FORCE MATERIEL COMMAND
HANSCOM AIR FORCE BASE, MA 01731-3010

The views and conclusions contained in this document are those of the authors and should not be interpreted as representing the official policies, either expressed or implied, of the Air Force or the U.S. Government.

This technical report has been reviewed and is approved for publication.

JAMES F. LEWKOWICZ
Contract Manager
Solid Earth Geophysics Branch
Earth Sciences Division

JAMES F. LEWKOWICZ
Branch Chief
Solid Earth Geophysics Branch
Earth Sciences Division

DONALD H. ECKHARDT, Director
Earth Sciences Division

This document has been reviewed by the ESD Public Affairs Office (PA) and is releasable to the National Technical Information Service (NTIS).

Qualified requestors may obtain additional copies from the Defense Technical Information Center. All others should apply to the National Technical Information Service.

If your address has changed, or if you wish to be removed from the mailing list, or if the addressee is no longer employed by your organization, please notify PL/IMA, 29 Randolph Road, Hanscom AFB MA 01731-3010. This will assist us in maintaining a current mailing list.

Do not return copies of this report unless contractual obligations or notices on a specific document require that it be returned.

REPORT DOCUMENTATION PAGE

Form Approved
OMB No. 0704-0188

1. AGENCY USE ONLY *(Leave blank)*

2. REPORT DATE
8 June 1993

3. REPORT TYPE AND DATES COVERED
Final (July 1990-March 1993)

4. TITLE AND SUBTITLE
Analysis of the Effects of Eurasian Crustal and Upper Mantle Structure on Regional Phases Using Broadband Seismic Data

5. FUNDING NUMBERS
PE 62101F
PR 7600
TA 09
WV AP
Contract F19628-90-K-0041

6. AUTHOR(S)
Jos Beckers, Susan Schwartz and Thorne Lay

7. PERFORMING ORGANIZATION NAME(S) AND ADDRESS(ES)
Institute of Tectonics
University of California, Santa Cruz
Santa Cruz, CA 95064

8. PERFORMING ORGANIZATION REPORT NUMBER

9. SPONSORING/MONITORING AGENCY NAME(S) AND ADDRESS(ES)
Phillips Laboratory
29 Randolph Road
Hanscom AFB, MA 01731-3010

Contract Manager: James Lewkowicz/GPEH

10. SPONSORING/MONITORING AGENCY REPORT NUMBER
PL-TR-93-2131

11. SUPPLEMENTARY NOTES

12a. DISTRIBUTION/AVAILABILITY STATEMENT
Approved for public release;
distribution unlimited

12b. DISTRIBUTION CODE

13. ABSTRACT *(Maximum 200 words)*

This report presents the results of the second phase of a two-year effort to investigate the effects of upper mantle structure on the propagation of regional phases. The first year investigation was directed at improving our understanding of the behavior of the PP phase at upper mantle distances, and developing methods to map large-scale variations in uppermost mantle velocity structure. During the second year investigation presented here, we successfully applied the techniques developed to a dataset of 45 PP waveforms for paths traversing China. We determined a first order P wave velocity model for the crust and upper mantle under China, which best explains the overall dataset. Next, we investigated the data on a path-by-path basis to constrain lateral deviations from this average model and to map large-scale variations in absolute velocities and velocity gradients in the uppermost mantle under China. Our final effort was directed at exploring the effect of our regionalized velocity models, on the propagation of the P_n and L_g regional phases to assess how variations in the velocity structure under China influence P_n/L_g ratios for earthquake and explosion sources.

14. SUBJECT TERMS
Upper Mantle Velocities
Regional Propagation
Regional Discrimination
Lateral Heterogeneity

15. NUMBER OF PAGES
108

16. PRICE CODE

17. SECURITY CLASSIFICATION OF REPORT	18. SECURITY CLASSIFICATION OF THIS PAGE	19. SECURITY CLASSIFICATION OF ABSTRACT	20. LIMITATION OF ABSTRACT
Unclassified	Unclassified	Unclassified	SAR

Contents

Illustrations

Illustrations

Tables

Summary

We model 45 P and PP waveforms at epicentral distances of 14^o to 40^o, primarily sampling western and central China, to determine regionalized P wave velocity variations for the crust and upper mantle in this region. The association between these variations and subsurface tectonic features is established. The regionalized velocity models are used to generate synthetic seismograms for explosion and earthquake sources at regional distances to examine the effect of crust and mantle lid variations on the propagation of the P_n and L_g phases.

Observed P and PP waveforms are matched by one dimensional forward modeling using the reflectivity technique. Our approach is to first find a homogeneous average velocity model for China which can match the observed broadband waveforms filtered with a long-period instrument response. This model is then used as a starting model for the matching of the broadband waveforms to interrogate the lateral velocity variations. Our preferred average model WCH has a 50 km thick crust with a velocity of 6.4 km/s, a P_n velocity of 8.15 km/s and a low velocity zone between 100 km and 175 km depth. It has intermediate characteristics between an active tectonic region and a stable shield, compatible with previous S wave modeling results. Modeling of the broadband waveforms indicates significant lateral deviations from model WCH. Paths traversing eastern China require a constant velocity lid of about 100 km thickness, a P_n velocity from 8.12-8.14 km/s and a crustal thickness between 27-35 km. For northern China a crustal thickness between 43-50 km, a P_n velocity of about 8.0 km/s and a 100 km thick lid with a positive velocity gradient are preferred. For the Tibetan plateau we observe large crustal thickness (50-60 km) and P_n velocity (8.15-8.25 km/s) in combination with a more pronounced low velocity zone than that of the average model WCH. Lower velocities may extend below 200 km depth. Our modeling indicates a thin lid of about 50 km thickness for this plateau. We infer from our results and previous work that crustal shortening and thickening is the most likely process responsible for the Tibetan plateau's thick crust and high average elevation. We suggest that the Indian plate has probably only underplated the southernmost part of the plateau. Mantle convection associated with the crustal shortening process has led to strong lateral heterogeneity in the upper mantle under Tibet. Higher P_n velocities in western Tibet might indicate that this region is presently undergoing crustal shortening.

The regional variations in lid structure predict large variability in regional wave amplitudes, particularly for the P_n/L_g discriminant. This ratio may vary by as much as an order of magnitude for crustal and upper mantle velocity variations typical for China. Short-period L_g is found to have very stable propagation characteristics; high frequency P_n rms amplitudes exhibit a more complicated behavior. For any of the regionalized Chinese velocity models, short-period P_n/L_g ratios for the explosive source are consistently higher than those for the earthquake source. However differences in this ratio between the explosion source and the earthquake source are considerably smaller than variations in P_n/L_g ratio resulting from propagation differences. Discrimination attempts based on this ratio should therefore be undertaken with care and propagation paths for both sources have to be similar. Broadband P_n/L_g ratios for the explosion source can be both higher or lower than those for the earthquake source making this passband poorly suited for discrimination purposes.

1. Introduction

Determination of upper mantle velocity variations in Eurasia has long been problematic due to the lack of seismic stations or data availability in China and the former Soviet Union. Early P wave velocity studies (e.g. King & Calcagnile, 1976; Given & Helmberger, 1980; Vinnik & Saipbekova, 1984) were limited to northwestern Eurasia, using Russian nuclear explosion data recorded at stations in western Europe. Recently, preliminary analyses using data recorded within the C.I.S. have been conducted (Goldstein et al., 1992; Garnero et al., 1992), refining earlier models for the P wave velocity structure under Russia. Because large parts of Eurasia are devoid of earthquake sources and most stations have been confined to the margins of this continent, studies of central and east Asia have mainly used multi-bounce S waves or surface waves which span longer distances than direct P and S waves. Grand & Helmberger (1985) used differential travel-times and general characteristics of long-period S, SS and SSS waveforms from southeast Asian earthquakes recorded at stations in western Europe, to explore radial and lateral variations in shear wave velocity structure in Eurasia. Lyon-Caen (1986) used S and SS waveforms sampling the Indian Shield and the Tibetan plateau to determine S wave velocity variations in this region. This work was extended by Zhao et al. (1991) using S, SS, Love and P_{nl} waveforms for paths traversing Tibet and eastern China. Many surface wave studies have been conducted to place constraints on the shear wave velocity structure beneath Eurasia, particularly for the Tibetan plateau (e.g. Chen & Molnar, 1975; Chun & Yoshi, 1977; Patton, 1980; Romanowicz, 1982,1984; Jobert et al., 1985; Brandon & Romanowicz, 1986; Bourjot & Romanowicz, 1992).

Most waveform modeling studies assume laterally homogeneous material properties to justify a one dimensional modeling approach. For long-period waveform analysis this assumption is often met and one dimensional earth models have given satisfactory fits to observed waveforms (e.g. Burdick, 1981; Grand & Helmberger,1984, 1985; Lyon-Caen, 1986, Lefevre & Helmberger, 1989). For this study we will rely on the same assumption on a path by path basis; however, since broadband data are much more sensitive to lateral inhomogeneity (Paulssen, 1987) and because the tectonic setting in southeastern Eurasia is very heterogeneous, we are required to use shorter and more geographically restricted paths than most previous studies. This is only viable using data collected within the region under study.

In 1986, the Chinese Digital Seismic Network (CDSN) of broadband stations was deployed, which together with the relatively high seismicity in this region offers for the first time an opportunity to study broadband P and PP waveforms at close enough distances to justify localized one dimensional modeling efforts. During the last 7 years of operation, the CDSN stations have accumulated a moderate number of high quality P waveforms sampling the upper mantle under

China, enabling a study of the mantle velocity structure with relatively high density path coverage. In late 1989 the broadband IRIS/IDA network began deployment in the C.I.S.. A preliminary analysis using data recorded by this network has been conducted by Goldstein et al. (1992). However, the amount of high quality data available for the IRIS/IDA stations is not yet large enough for a thorough study of the upper mantle under central Asia. We will therefore concentrate on resolving lateral variations in the upper mantle P wave velocity structure under China using broadband P and PP waveforms recorded at CDSN stations for earthquake sources with well constrained moment tensor solutions.

Analysis of the velocity structure under China is particularly interesting because of its strong tectonic heterogeneity related to the collision of the Indian and Eurasian plates 40-60 Ma ago, which initiated the Himalayan orogeny. The Tibetan plateau, a region of numerous fold belts in southwest China (Figure 1) with an average elevation of 5000 m above sea level, is certainly the most impressive feature related to this collision. Several deep refraction studies (Yuan et al., 1986; Mooney, 1992) as well as surface wave studies have indicated an average crustal thickness of 70 km for this plateau. The fold system continues into Nepal and northern India and is bordered to the south by the Indian stable shield. The northern part of China and Mongolia is also characterized by several fold belts. These are bordered to the north by the Siberian platform and are separated from the southwestern fold system by the Tarim basin to the west and the Sino-Korean platform to the east (Figure 1). Crustal thicknesses range from 50 km in northwest China to 35 km for the eastern platforms (e.g. Mooney, 1992).

Two very different mechanisms have been suggested to explain the evolution of the Tibetan plateau. Argand (1924) originally proposed that the whole of Tibet is underlain by the northern part of the Indian plate. Studies supporting this theory indicated that this underthrusting might extend as much as 1000 km into Eurasia (Barazangi & Ni, 1982; Ni & Barazangi, 1983). The buoyancy of the thick crust thus created would be able to support the weight of the overlying mountain range and give the Tibetan plateau its high average elevation. In contrast, others (e.g. England and Houseman, 1986) suggested that Tibet's crust was thickened and elevated due to folding and thrust faulting under the north-south compressional regime resulting from the collision. Molnar (1988) gave an extensive review of geophysical constraints used to infer the evolution of the Tibetan plateau and its surrounding regions. Seismological studies of the lid velocity structure under Tibet play an important role in resolving this evolution. A thick high velocity lid, associated with colder material, is viewed as evidence for underthrusting, while a thin or non-existing lid points to the absence of an underthrusted lithospheric plate and possibly upwelling warmer mantle material.

Studies of P wave velocities in the mantle directly beneath the Moho have found P_n values between 8.1 km/s (Molnar & Chen, 1984) and 8.43 km/s (Barazangzi & Ni, 1982) for the Tibetan plateau. Holt & Wallace (1990) put narrower constraints on P_n velocities for this region: 8.1 - 8.25

km/s. They find P_n velocities for northern India and southeastern China to be around 8.0 km/s. Holt & Wallace (1990) explain the sharp velocity jump of 0.2 km/s they observe for the transition zone between the Indian shield and the southern Tibetan plateau by increased pressures in the mantle at the base of the crust due to the doubling of the crustal thickness, assuming an unperturbed temperature regime. For southern Tibet they find that a 100 km thick lid with a positive lid velocity gradient best explains their data. Holt & Wallace (1990) infer that the southern half of Tibet is being underthrust by the Indian lithosphere. Lyon Caen (1986) finds a thin shear wave velocity lid underlain by a distinct low velocity zone for the central and northern Tibetan plateau. This indicates that this underthrusting has not taken place under the whole of Tibet. In contrast, the velocity model of Zhao et al. (1991) for similar paths through Tibet has a slower lid than Lyon-Caen's (1986) and does not exhibit a pronounced low velocity zone. The shear wave velocity model of Zhao et al. (1991) seems to be at least partly influenced by propagation through the Chang Thang province in north-central Tibet (Figure 1), a region for which Bourjot & Romanowicz (1992) indicated a thin high velocity crust together with a low S_n velocity. Ni & Barazangi (1983) also found a low Q value for this region, observations that can be correlated with recent volcanism (Gansser, 1980).

Less is known about upper mantle velocities and related subsurface tectonic features in other parts of China. Preliminary S wave results of Zhao et al. (1991) for eastern China indicate a distinct low velocity zone in the lid together with a higher S_n velocity than for their Tibetan model. The focus of this study is to analyze large scale lateral variations in the upper-mantle P wave velocity under China, establishing association with tectonic features related to the Indian-Eurasian collision.

The 1992 megaton explosion at the Lop Nor test site in the Tarim basin (Figure 1) emphasized that China remains an important region for nuclear test monitoring. P_n and L_g are often used as underground nuclear explosion discriminants and yield estimators. Variations in crustal and upper mantle velocity structure have pronounced effects on the propagation of these regional phases. For this purpose it is important to understand how the propagation of the P_n and L_g phases is affected by variations in the Chinese crust and upper mantle velocity structure. This will enable discrimination studies to correct for path effects and thus facilitate discrimination and improve yield estimates. The thickness and velocity structure of the crust strongly influence the propagation of L_g. For explosion sources, the excitation of L_g is governed by the P wave velocity near the source and S wave velocities in the uppermost mantle (Frankel, 1989). The ratio of these two velocities determines how much energy can be trapped in the crust (Xie & Lay, 1993). Along with crustal structure, the behavior of the P_n phase, which travels just below the Moho also depends on lid velocity gradients, with less P_n energy being lost by radiation into the mantle for positive velocity gradients. We will generate synthetic seismograms at regional distances to assess

how the P_n and L_g phases are influenced by our models of lateral variations in the crustal and upper-mantle P wave velocity under China.

2. Propagation characteristics
2.1 P and PP waveforms

Information on upper mantle structure can best be obtained from direct P phases at distances of 12.5° to 30°. In the 12.5° to 20° distance range, the timing and amplitude of the triplication arrivals related to the 420 km and 670 km discontinuities are sensitive to velocity gradients in the upper mantle (e.g. Burdick, 1981). At epicentral distances between 20° to 24° these triplication phases arrive in a very short time window and are not very diagnostic of velocity variations in the upper mantle. Beyond 24° the direct P phase traverses the uppermost mantle at a steep angle and is only sensitive to the average lid velocity structure.

Grand & Helmberger (1984) and Lefevre & Helmberger (1989) have demonstrated that multibounce P and S waves can greatly extend the distance range providing information on the upper mantle velocity structure. Since PP triplication phases arrive at twice the distance range of corresponding direct P wave triplications (25° to 60°), the branches associated with the triplication arrivals have twice the time separation making their identification much easier. In addition, differences between P and PP are very pronounced, with PP-P differential travel times and amplitudes yielding constraints on the velocity structure.

Several studies have concentrated on identifying these multibounce triplication phases and examining their sensitivity to upper mantle velocity structure (Grand & Helmberger, 1985; Lyon-Caen, 1986; Lefevre & Helmberger, 1989; Zhao et al., 1991). Using synthetic studies, Schwartz and Lay (1993) have shown that the presence and strength of precursors to the PP phase is highly diagnostic of velocity gradients in the lid. For positive lid velocity gradients strong arrivals are apparent between the P and PP wavetrains at distances of 25° to 34°, with less energy arriving in this time window for constant lid velocities and only weak energy for negative gradients. These precursors are associated with energy turning in the lid just below the crust, hugging the Moho (whispering gallery phases). Beyond 34° energy bottoming deeper in the upper mantle and multiply reflecting from the bottom side of the Moho becomes the dominant arrival preceding PP. This arrival is stronger for negative lid velocity gradients which force energy to turn deeper. Beyond 38° little precursory energy exists other than interactions with the transition zone (Neele & Snieder, 1991). At distances closer than 25° the presence of precursors to PP is obscured by late P triplication arrivals and associated coda. The whispering gallery phases appear as impulsive arrivals in the seismogram because much of their low-frequency energy is lost through tunneling in the lower velocity material directly beneath the lid (Menke & Richards, 1980). This makes

whispering gallery phases hard to discern on long-period recordings. The presence of strong lateral heterogeneity may also obscure the identification of these phases.

Schwartz & Lay (1993) showed that crustal reverberations contribute significantly to the later part of the PP wavetrain, while the late coda of PP is strongly affected by surface wave scattering (Neele & Snieder, 1991). PP-P differential travel times are also strongly influenced by crustal thickness, an important feature that can easily be misinterpreted as variations in lid velocity structure. The timing of the PP phase can also be confused with the arrival of the underside reflection from the Moho. Crustal thicknesses can, to some extent, be interrogated from the characteristic period of the early coda trailing the main P and PP arrivals, which is dominated by crustal reverberations. Using this information is difficult in the presence of strong lateral variations in crustal thickness, since for the P and PP phases these reverberation are generated at two or three locations along the earth's surface, respectively. The timing between the underside reflection off the Moho and the first energy of the PP phase puts another constraint on the crustal thickness at the midpoint of the raypath. Because the PP wave has distortion due to being a maximum time phase, it necessary to make synthetic seismograms to model the time differences. Since there are so many factors contributing to the timing of the PP phase it is often necessary to use a priori velocity structure information. For many regions detailed information on crustal thicknesses is available from other (e.g. refraction) studies. Constraining the crustal thicknesses in this way allows properties of the upper mantle to be more reliably determined.

2.2 Regional phases

The crustal and upper mantle characteristics that we attempt to model using the P and PP waveforms have a strong influence on the propagation of regional phases. The P_n and L_g phases in particular are often used to discriminate between earthquake and explosion sources and to estimate yields. For this purpose it is very important to understand how the excitation and propagation of regional phases is influenced by the local velocity structure in order to enable correction for propagation effects along the raypath.

The L_g phase is commonly used for discrimination purposes because of its stable propagation properties which have been thoroughly investigated (e.g. Hansen et al., 1990; Ringdal, 1991; Israelsson, 1992). The excitation of this phase, which strongly depends on how much S wave energy can be trapped in the crust, is very complicated. For an explosion source, the effectiveness of L_g excitation is governed by the P wave velocity near the source and the S wave velocity in the uppermost mantle (Frankel, 1989). If the P wave velocity at the source is lower than the S_n velocity the pS phase can be trapped in the crust by (post-)critical reflection at the Moho. In this case, the pS phase is the dominant energy in the L_g wavetrain. The amount of energy that can be

trapped in the crust decreases as the ratio of the P wave velocity near the source and the S wave velocity in the uppermost mantle approaches 1. This can be attributed to the fact that the slowness range (takeoff angles) that will lead to a critical reflection at the Moho narrows as this ratio increases (Xie & Lay, 1993). A similar observation can be made for sources that also radiate S wave energy. The respective criteria for P and S energy generated near the source to be trapped in the crust are:

$$\sin i_p \geq \frac{V_{Psource}}{V_{Smantle}} \tag{1}$$

$$\sin i_s \geq \frac{V_{Ssource}}{V_{Smantle}} \tag{2}$$

where i_p and i_s are the take-off angles of P and S waves. If the P wave velocity near the source is greater than the S wave velocity in the uppermost mantle pS cannot be trapped in the crust and energy will be lost through radiation to the mantle at each consecutive interaction with the Moho. In this case the non-geometrical S^* phase will be the main contributor to the L_g phase (Gutowski et al., 1984; Frankel, 1989). The propagation of L_g mainly depends on the thickness and structure of the crust; a thicker crust being a better waveguide for this phase because more modes can be trapped.

The P_n phase is critically reflected at the Moho and travels along the bottomside of the crust. The critical reflection of P_n energy at the Moho depends on the P wave velocity contrast directly below and above this interface. The amount of energy of this phase that can leak into the deeper mantle depends on the lid velocity gradients. Higher gradients retain more P energy trapped directly below the crust, resulting in higher P_n amplitudes. The propagation of P_n is thus strongly affected by the P wave velocity structure in the crust and uppermost mantle.

3. Data and modeling procedure

In order to obtain P and PP waveforms suitable for modeling of the crustal and upper mantle structure under China we searched the Harvard-CMT catalog for events with m_b larger than 5.2 in the southeast Asian region which were recorded within a 14^o to 40^o epicentral distance range by at least 2 of the CDSN stations. Data obtained from the IRIS database in Seattle were selected on quality of the P waveforms and subsequently deconvolved by the instrument response to yield displacement traces. We obtained recordings from 6 broadband seismic stations of the CDSN array which are mainly located in the northern half of China (Figure 2). Of the 54 events examined, we selected 13 earthquakes with simple waveforms and well determined focal mechanisms. This large data reduction is due to the requirement of having high quality data, necessary for a successful modeling effort. Without clearly identifiable phases, waveform modeling is likely to fail since

different characteristics of the data are easily confused. Most epicenters are located in the tectonically active regions of western and southern China. There is a total of 45 paths, primarily sampling western, central and northern China with virtually no coverage in the southeast (Figure 2). For the post-1988 period of our event search no high quality data in southeast Asia were found to eliminate the lack of coverage in this region. It will therefore be difficult to put constraints on the velocity structure of the eastern stable platforms. Our models are primarily for the active fold belts in southwestern China. Table 1 gives the source characteristics of the earthquakes used in this study.

We match the observed traces by one dimensional forward modeling. Our approach is to first model traces filtered with a long-period WWSSN instrument response. This filtering facilitates determination of the source parameters and simplifies identification of the triplication phases. The objective of this approach is to obtain a first-order velocity model that matches, to the extent possible, all long-period waveforms. This model then can serve as a starting model for matching the broadband data. Modeling of the broadband data refines the velocity structure information and resolves lateral velocity variations.

Focal mechanisms, source depths and source time functions are constrained by modeling P waveforms at teleseismic distances. As starting parameters we use the Harvard Centroid Moment Tensor (CMT) solutions. Our events range in magnitude from $m_b = 5.5$ to 6.8 with source durations of up to 7 seconds (Table 1). We use either trapezoids or half cycle sinusoids to model the source time functions. For events with magnitudes higher than about $m_b = 7.0$ such a simple representation is often inadequate and the more complex source time functions obscure the velocity structure information. Events smaller than about $m_b = 5.5$ suffer from poorly constrained focal mechanisms and a lower signal to noise ratio. For the events modeled, source complexity and signal to noise issues mainly complicate matching the broadband data; long-period waveforms are easier to match.

Differences between existing procedures for generating synthetic seismograms have been thoroughly investigated and are well understood (e.g. Burdick & Orcutt, 1979; Chapman & Orcutt, 1985). Because the WKBJ method of Chapman (1978) is exceptionally fast relative to other synthetic seismogram codes it is well suited for determining the source parameters from teleseismic P waves. These can be adequately matched with the inclusion of only the P, pP and sP ray paths. Though WKBJ can model PP-P differential travel-times and gross PP amplifications, it fails in matching PP waveform characteristics at upper mantle distances when the standard practice of including only primary ray paths is followed (Schwartz & Lay, 1993). Adding enough phases to adequately match observed PP characteristics is a time consuming and slowly converging process. The reflectivity technique developed by Fuchs & Müller (1971) completely accounts for all P-SV interactions in a multi-layered earth and can adequately match observed PP waveforms. After

determining source parameters using WKBJ modeling of teleseismic P waveforms, we therefore used reflectivity synthetics calculated on local SUN-sparc2 stations and CRAY or Stellar computers at Lawrence Livermore National Laboratory (LLNL) for modeling of the complete P and PP waveforms to obtain velocity structure information.

4. Results

4.1 Long-period modeling

Our first modeling objective is to establish a homogeneous reference velocity model which can match observed long-period waveforms on average for the whole of China. In order to assess what range of upper mantle velocities to expect for China, long-period synthetics were initially generated for a suite of 3 velocity models (Figure 3) ranging from the fast shield-type models S25 for the Canadian shield (Lefevre & Helmberger, 1989) and K8 for northwestern Eurasia (Given & Helmberger, 1980), to the slow T7 model (Burdick & Helmberger, 1978) for the active tectonic region of the western United States. Figure 4 shows P and PP waveforms at distances ranging from 28^{o} to 36^{o} for paths through different tectonic regions of China. The data and synthetic traces are aligned on their first motions, thus we do not consider absolute travel times. This makes the matching of observed waveforms by synthetics less sensitive to the exact event locations, thereby reducing the unknowns that have to be considered in the modeling process. Data and synthetics are normalized relative to their peak amplitudes. Comparison of synthetics generated for models K8 and T7 with the data shows that PP arrives too early for K8 and too late for T7. This proves to be generally true for observations in China. At distances closer than about 30^{o} few clear PP arrivals can be seen in the long-period data. PP-P differential travel times are strongly influenced by P wave velocities in the uppermost 200 km of the earth, the depth range where differences between models K8 and T7 are most pronounced.

In order to more reliably determine P wave velocities in the lid we constrain the crustal structure by using results of previous studies. Several refraction studies (Yuan et al., 1986; Mooney, 1992) have shown that crustal thickness exceeds 45 km for most of China, with maximum thickness of up to 70 km for the Tibetan plateau. Since most paths used in this study cross central and western China, a 50 km thick crust for our preferred model WCH (west China) is a good estimate to use for a first order velocity profile suitable for this region (Figure 3, Table 2). Holt & Wallace (1990) find P_n velocities for southern China ranging from 8.0 km/s for the southeast to 8.25 km/s for the Tibetan plateau. Model WCH has a P_n velocity of 8.15 km/s and a low velocity zone between 100 km and 175 km, necessary to slow down the first arrival of the PP wave train. Figure 4 shows that model WCH is able to explain PP-P differential travel times over a wide range of distances for markedly different tectonic regions.

The synthetics generated for model K8 show strong PP coda, a feature that is not observed in the data. This coda mainly consists of crustal reverberations (Schwartz & Lay, 1993), the strength of which is determined by P wave velocities directly below and above the Moho. The reflection coefficient at the Moho increases for higher P_n/P_{crust} ratios, thus increasing the energy of the crustal bounces. Since we adopted the same crustal velocity of 6.4 km/s as in model K8 the mantle lid velocity for our first order model WCH should be lower than that of model K8. The P_n velocity of 8.15 km/s for model WCH predicts the observed PP coda well. Also apparent from Figure 4 is that model T7 predicts too much energy in the later part of the PP arrival itself. The amplitude of the PP transition zone triplication phases, relative to shallow turning PP energy, is strongly influenced by P wave velocities in the lower lid. Lower velocities in this depth range tend to decrease the amplitude of the early part of the PP wavetrain for which the energy traverses the lower lid at a shallow angle. This indicates that our first order model needs higher velocities than those of model T7 in the lower lid. The less pronounced low velocity zone of model WCH indeed better predicts relative amplitudes of the PP triplication phases (Figure 4). Though difficult to discern in the long-period data, the energy arriving in the window between P and PP seems well modeled; another indication that velocity gradients in the WCH lid are suitable for the China region. Velocities between 200 km and the 420 km discontinuity of model WCH are similar to those of other models (Figure 3) and are constrained by differential travel times of the PP triplication phases and overall PP amplitudes (Figure 4). The effect of increasing velocities in this depth range is to decrease differential travel times of the PP triplication phases and to increase PP/P amplitude ratios. These features are in general well predicted by model WCH.

A P and PP travel-time curve for model WCH is shown in Figure 5. Figure 6 illustrates that model WCH can also match observed P triplication behavior for paths throughout China. Comparison with Figure 4 shows that waveform differences at P triplication distances predicted by the three models are considerably smaller than PP triplication differences. Beyond 18^{o}, differences in the synthetic waveforms for the different models are very small. Given the sparse data coverage, adding multibounce phases in the modeling effort is thus vital for a detailed study of the upper mantle velocity structure. Although individual features of the data may be better matched by one of the slower or faster models, overall WCH best explains the data. It is remarkable that in this very heterogeneous region complex long-period waveform characteristics for a large number of paths can, to a great extent, be explained by a single velocity model.

Although model WCH can match observed waveforms for paths throughout China (Figures 2,4 & 6) it is evidently more characteristic for the active tectonic region of southwestern China with its thick crust and fairly high P_n velocity, and lateral deviations from this average model may be expected. This first order model has a number of remarkable features making it unusual in character. It has a relatively thick crust (50 km), a feature that contrasts with what is commonly

observed for active tectonic regions (Mooney & Braille, 1989). Model WCH also has a P_n velocity (8.15 km/s) that is distinctly higher than normally seen for active tectonic regions. The lid velocity structure is not typical for an active tectonic region, or for a stable shield, but shows an intermediate behavior.

Indications of the range of variations in lid velocity structure we might expect beneath China can be seen from the long-period waveforms shown in Figure 7. The data for event 2, recorded at station KMI is best matched by model T7. The considerably slower crust and lid of this model pulls apart the P triplication arrivals enough to correctly predict the arrival of energy turning between the 420 and 670 km discontinuities (CD branch) relative to energy turning above the 420 km discontinuity (AB branch). The path from event 4 to station BJI is more complicated. The CD branch arrives shortly after the AB branch, a feature that is best predicted by model S25. Energy turning below the 670 km discontinuity (EF branch) is relatively slow which is best matched by model WCH. The shape and amplitude of the AB branch is best modeled by K8. Since the timing of energy turning between the 420 and 670 km discontinuities is influenced more by the shallow velocity structure than energy turning below the 670 km discontinuity this indicates that velocities in the lid should be higher than those of model WCH and that velocities at larger depths should be somewhat lower than those of model WCH to compensate for the effect of the higher lid velocities on the EF branch. Similar observations can be made for the raypath from event 4 to station WMQ. The P phase for this path is best explained by model S25 whereas the arrival of PP is best predicted by model T7, although the PP amplitude is overestimated by this model. The best match of the synthetic for model K8 to the data of event 8, observed at station BJI is explained by this path sampling basin type material over its whole extent (Figure 2). In summary, of the 45 paths we used in the long-period modeling process, 22 where best explained by model WCH, 5 paths were clearly faster and 1 path was slower, the remaining paths revealing no clear preference for any of the models considered. An overview of the complete long-period modeling results is given in appendix A. Faster and slower paths are not confined tc distinct regions, but are intermixed, indicating that the structure of the crust and upper mantle under China cannot simply be subdivided into typical shield type (S25, K8) regions or typical active tectonic regions (T7) but instead shows a more complex intermediate behavior. Using the broadband waveforms we will try to discriminate regionalized deviations from the average model WCH.

4.2 Broadband modeling

Equipped with a good model for the average lid velocity we can use precursors to PP to interrogate velocity gradients in the upper mantle directly below the crust. Energy in the window between P and PP is most sensitive to these gradients and will therefore suffer least from non-

uniqueness of the velocity information we can extract from the data. Two examples of how we can use precursors to PP to determine the lid velocity gradients are shown in Figure 8. Model WCH predicts too much energy preceding PP relative to the observed waveform of event 12 at station BJI. By flattening the low velocity zone this energy is effectively reduced. The reason for the reduced velocities in the 200-400 km depth range is to optimize the timing of the PP triplication arrivals, the thinner crust better matches the timing between energy reflected off the Moho and energy reflected off the crust. The WCH synthetic for the same event observed at station HIA underpredicts the energy arriving directly before PP. This amplitude can be increased by making the low velocity zone more pronounced, thus increasing the velocity gradients at both the top and bottom of the low velocity zone. Considerably higher gradients are needed to significantly increase the precursory energy. Since model WCH correctly predicted the timing of the PP arrival, the average velocity in the lid needs to remain the same, requiring an increased P_n velocity. Thus by changing the shape of the low velocity zone we can control the amount of energy arriving in the time window between the P and PP phases. Increasing the negative velocity gradient causes more energy to turn deeper in the mantle in the positive velocity gradient below the low velocity zone. This leads us to conclude that, even at distances as close as 31^{o}, energy turning below the lid and multiply reflecting off the bottom side of the Moho is the dominant arrival in this time window.

More evidence for deviations from model WCH in the southwestern part of China can be seen for other recordings of event 12 (Figure 9). At about 15^{o} the P triplication arrivals are clearly separated (Figure 5), with the AB branch arriving first and the EF branch arriving last. Near 22^{o} the AB branch almost coincides with the CD branch for model WCH, both arriving about 7 seconds before EF. The AB and CD branches together form the first upswing in the LZH seismogram followed by the CD depth phases which can be seen as distinct negative arrivals, the EF branch being only a weak arrival in the seismogram. The P triplication phases as predicted by model WCH arrive in a too short time window for both waveforms shown in Figure 9. Lowering the velocities at depths greater than 200 km effectively pulls apart the triplication arrivals. A secondary effect of these lower velocities on the synthetic waveform for station WMQ is that the energy of the AB branch is reduced. This can be counteracted by increasing velocities in the lid. These higher lid velocities only slightly affect the timing of the triplication arrivals because the P energy traverses this part of the mantle at a steep angle. The added crustal thickness for this path gives a good fit to the observed P wave coda. The increased P_n velocity for the waveform recorded at station LZH optimizes the timing between energy turning above the 420 km discontinuity and the depth phases associated with energy turning between the 420 and 670 km discontinuities.

The velocity structure of the stable eastern platforms can be interrogated to a limited extent using paths branching to the northeast from event 3, partially traversing these platforms (Figure 2). The strongest indications for the lid velocity structure can again be derived from modeling PP

characteristics. For both waveforms shown in Figure 10 the timing and general shape of the PP phase can best be explained by a constant velocity lid and crustal thicknesses that are considerably smaller than 50 km. For the path to station MDJ a somewhat lower P_n velocity (8.12 km/s) is needed to match the timing of PP energy. The thin crust (27 km) for this path also matches the crustal reverberations trailing the PP wavetrain.

Event 4 was used to investigate the crustal and upper mantle velocity structure in the fold belt region of northern China and Mongolia. The waveforms shown in Figure 11 reveal evidence for lower P_n velocities (8.0 km/s) combined with a positive velocity gradient in the lid. For the path from event 4 to station BJI model WCH predicts the second (CD) branch of the triplication arrivals to arrive too close after the first (AB) branch. The effect of the lower velocities in the 200-420 km depth interval is to pull apart these triplication arrivals. Higher velocities in the lower lid increase the amplitude of the CD relative to the AB branch. However, these higher velocities also shorten the time window of the triplication arrivals. The average lid velocity needs to remain equal to that of model WCH, requiring a lower Pn velocity and thus a positive gradient in the lid. The effect of this gradient on the synthetic waveform for station WMQ is to better predict the shape of the first positive upswing in the P arrival. A lid with a positive velocity gradient also better matches the observed arrival of the second (CD) branch of the PP triplication which was predicted too late for model WCH. The second negative peak of this branch, a depth phase, is still poorly predicted however. We did not try to improve the match because it might also be caused by a slightly erroneous focal mechanism. This is not unlikely since the amplitude overprediction of the onset of the P phase can also be attributed to a focal mechanism error. We infer this because the mismatch is consistently present for synthetics generated with velocity models as different as S25 and T7. The onset of PP arriving shortly after P and energy in between these two phases does seem better matched by the gradient lid model.

We have found significant deviations in crustal and upper mantle structure from the average China model WCH. Figure 12 shows our preferred models for the Tibetan plateau (TP), the eastern platforms (CHE) and northern China (NCH) together with the average model WCH and P and S wave models of previous studies; Figure 13 summarizes lateral variations in the upper mantle velocity structure under China at different depth intervals. While the model variations are not unique we emphasize the more robust features. An overview of the modeling results is given in appendix B. A total of 6 events (19 paths) were used for broadband modeling. Source mechanisms of the other events could not be constrained well enough to confidently match the broadband data. In contrast to the long-period synthetics which are not very sensitive to small variations in source mechanism, details of the broadband synthetic waveforms can change significantly.

Though absolute lid velocities of the Russian P wave model CE200 (Figure 12) of Garnero et al. (1992) are higher than those of model WCH, the lid velocity gradients of the two models are

very similar. The most striking difference is the 220 km discontinuity their model indicates. We included a 220 km discontinuity in our models to see whether the presence of such a velocity jump was required by our data. However, a velocity contrast similar to that of model CE200 changed only minor details of the broadband synthetics. We therefore cannot discern whether or not a 220 km discontinuity is present in the upper mantle under China. The presence of multilayering and lateral heterogeneity in the crust has been well documented (e.g. Mangino & Ebel, 1992; Mooney, 1992). We investigated the effect of a multilayered crust on the broadband synthetics and found that we could not confidently constrain depth dependent velocity information in the crust with our dataset. Furthermore, no evidence for lateral variations in crustal velocity was observed, although S wave velocities in Tibet are believed to be anomalously low (F.T. Wu, personal communication, 1993).

Figure 13a shows that crustal thicknesses average 50 km in the Tibetan region with 2 paths indicating thicknesses exceeding this value. Somewhat lower crustal thicknesses (43-50 km) are found for the northern fold system and considerably lower thicknesses (27-35 km) for 3 paths partly traversing the eastern platforms. These values are somewhat lower than results of previous studies (e.g. Yuan et al., 1986; Mooney, 1992), but we have limited resolution of crustal thickness. A study of the receiver structure beneath the 6 CDSN stations by Mangino & Ebel (1992) revealed 10-20 km thick transition zones between the crust and upper mantle, with velocities sharply increasing from about 6.0-6.4 km/s to a fixed preassumed local P_n velocity, for a number of these stations. Such a transition zone cannot be resolved by our data and its existence might be responsible for the shallower Moho depths of this study. Average crustal velocities of 6.4 km/s are suitable for all the paths used in this study.

We find P_n velocities (Figure 13b) ranging from 8.15-8.25 km/s for the Tibetan plateau and as low as 8.0 km/s for the northern fold belt. Paths traversing northeastern China need P_n velocities of about 8.12-8.14 km/s. Our P_n velocity range found for the Tibetan plateau agrees well with results of previous studies (e.g. Holt & Wallace, 1990; Mooney, 1992). Highest P_n velocities (8.20-8.25 km/s) can be observed for path originating in the western part of the plateau, compatible with the unusually high Rayleigh wave phase velocities found by Brandon & Romanowicz (1986) for this part of Tibet. Refraction studies indicate P_n velocities averaging 8.0 km/s near BJI and values up to 8.2 km/s north of KMI, a velocity range that is in agreement with P_n velocities we find for the easternmost paths. Besides a single refraction profile in the Tarim basin which indicates a P_n velocity of 7.9 km/s (Mooney, 1992) no values have been reported for the northern part of China and Mongolia.

This study indicates that the Tibetan plateau has a thin lid underlain by a low velocity zone with lower velocities extending below 200 km depth (Figure 13c,d). This observation is very similar to S wave velocity results (Figure 12) of Lyon-Caen (1986) and Wang et al. (1989, not

shown). The low velocity zone in our model TP is located somewhat deeper than in Lyon-Caen's (1986) model, and indicates a lid of about 50 km thickness. Given previous evidence for high P_n velocities under the Tibetan plateau, the timing of PP relative to P for observed waveforms of paths traversing this region requires the presence of a distinct low velocity zone in the upper mantle. The sensitivity of precursors to PP to velocity gradients in the uppermost mantle puts constraints on the Tibetan lid velocity structure and thereby also on the location of the low velocity zone (Figure 8).

Using P_n/P_l ratios Holt & Wallace (1990) determined positive lid velocity gradients of 0.18-0.25 km/s per 100 km with a 100 km thick lid for southern Tibet. Although our sources are located in their region of study their result is not necessarily in disagreement with what we find since most of our paths extend well north of this region. Two paths from our southernmost event 2 mainly traversing the Tibetan plateau indicate either no (station LZH) or a shallow low velocity zone (WMQ) indicating that a transition zone from a shield type lid in southernmost Tibet, as inferred from Holt & Wallace's data, to a weaker lid in central and northern Tibet may exist. However, due to a lack of paths purely traversing southern Tibet we cannot clearly resolve this.

From our results we infer that the greater part of the Tibetan plateau is presently not underlain by a shield-type structure. Thus, if the whole of Tibet were originally underthrust by the Indian plate this observation requires that the cold lithospheric material has disappeared in a relatively short time period. The high P_n and S_n velocities observed for the Tibetan plateau do not necessarily imply the underthrusting of cold lithospheric material. Crustal shortening and thickening requires that the underlying mantle material also undergoes shortening and thickening, moving cold isotherms downward. In this way higher velocities in the uppermost mantle can be produced by increased pressures due to the added crustal thickness in the absence of higher temperatures (Black & Braille, 1982; Holt & Wallace, 1990). We prefer the crustal shortening model for the evolution of the Tibetan plateau because it is able to explain a wide range of observations on the crustal and upper mantle structure in this region. Underthrusting seems to have only played a role in the shaping of the southernmost part of the plateau and the Himalayas (Molnar, 1988).

Lowered temperatures in the lid below Tibet will lead to horizontal temperature gradients in the mantle. These are likely to introduce thermal convection with horizontal motions directed toward the colder material beneath central Tibet. This requires upwelling warmer mantle material in the neighboring regions. A cartoon illustrating this scenario is given in Figure 22 of Molnar (1988). A recent tomographic study of lateral variations in P wave velocity beneath the Tibetan plateau by Zhao & Xie (1993) reveals a velocity image with highs and lows coinciding with proposed locations of upwelling and downwelling in the evolution model of Molnar (1988). Surface evidence for mantle upwelling can be seen from Quaternary volcanism in the Chang Thang region in north-central Tibet. A shallower crust together with lower Q and S_n values for the lid,

related to higher upper mantle temperatures, has been documented (e.g. Ni & Barazangi, 1983; Bourjot & Romanowicz, 1992) for this region. The S wave velocity model of Zhao et al. (1991) with its higher crustal velocity and slower lid than Lyon-Caen's (1986) in which a low velocity zone is virtually absent (Figure 12) also seems appropriate for the Chang Thang region. While we find evidence for the presence of lateral heterogeneity in the Tibetan lid (Figure 13a,b), the length and orientation of our paths is such that we cannot constrain the location and extent of such inhomogeneities. Combining lid thicknesses inferred by Lyon-Caen (1986) and Holt & Wallace (1990) with ours, indicates a northward thinning of the Tibetan lid. This suggests southward motion of warmer mantle material from the Chang Thang region, gradually weakening the lid from below. Molnar (1988) theorizes that the extremely high phase velocities found for westernmost Tibet (Brandon & Romanowicz, 1986), which are confirmed by high P_n velocities we find for that region, might indicate active crustal shortening accompanied by the sinking of cold material. Our modeling results show lower than average velocities between 200-420 km depth for the whole of Tibet (Figure 13d). These indicate the presence of warmer mantle material in a broad region in this depth range. Thus, very strong lateral heterogeneity in upper mantle temperatures seems to exist below the Tibetan plateau.

Holt & Wallace (1990) find strong evidence for a zero gradient model with a 100 km thick lid below southeastern China, similar to what our models infer for eastern China (model CHE, Figure 12). In contrast, Zhao et al. (1991) indicate an S wave model with a pronounced low velocity zone for the Yangtze and Sino-Korean platforms. However, since their sources are located at the edge of the Tibetan plateau and their stations are mostly underlain by oceanic lithosphere, their paths cross three very different tectonic provinces. A P wave velocity lid similar to the model of Zhao et al. (1991) would slow down the PP phase too much, unless such a lid was accompanied by a higher P_n velocity. Our P_n velocity range of 8.12-8.14 km/s for the easternmost paths is in agreement with the range found by deep refraction studies (Mooney, 1992). Furthermore, the constant velocity lid predicts hard to match details of observed broadband PP behavior well (Figure 10). We therefore infer that the eastern Chinese platforms can be characterized by a thick constant velocity lid indicating a stable evolution for the upper mantle in this region in recent times.

The positive lid velocity gradient model this study finds for northern China and Mongolia is preliminary and should be viewed with care. We only modeled 3 paths traversing this region and, given the uncertainty in the mechanism of event 4, the evidence for a positive lid velocity gradient model is not very strong. Further, no evidence either confirming or contradicting this observation has been found.

4.3 Propagation of regional phases

Having established regionalized velocity models for China we perform a synthetic study to assess how these velocity models affect the propagation of regional phases. P_n and L_g phases are often used in regional discrimination of explosion and earthquake sources. We will therefore analyze these phases using synthetics generated for the regionalized velocity models and explore differences in propagation for the different models.

The reflectivity technique of Fuchs & Müller (1971) was used to generate synthetic seismograms at regional distances. We used an explosive source located at 500 m depth and an earthquake source at 5 km depth, both with a source duration of 1.5 seconds. We calculated seismograms at distances of 1^o to 10^o at 1^o intervals. The station azimuth for the earthquake source is taken to be 22.5^o. Due to computational limits we were required to limit the maximum frequency of the synthetic seismograms to 2 Hz. Observed regional waveforms are known to have a frequency content of up to 5 Hz. Though this somewhat limits us in the extent to which we can quantify the effect of the regionalized models on the propagation of the P_n and L_g phases, most of their spectral energy is usually concentrated well below 2 Hz. In order to effectively generate the L_g phase for the explosion source we include a thin crustal layer at the free surface with a low enough velocity to capture the pS phase in the crust (Frankel, 1989). We use a 3 km thick layer with a P wave velocity of 4.4 km/s. The presence of such low velocities in the uppermost crust is well documented (e.g. Mangino & Ebel, 1992) but in general cannot be resolved by P and PP waveform modeling. The low velocity layer does not have a significant effect on the P and PP waveforms we used in this study because of its limited thickness.

We generated synthetics for model WCH and models typical for the Tibetan plateau (TP) and eastern (CHE) and northern (NCH) China (Figure 12). P_n/S_n velocity ratios in the lid are 1.731 for all models. Synthetic broadband vertical component displacement waveforms for model WCH and the explosive source are shown in Figure 14. The synthetics exclude phase velocities smaller than 3.3 km/s to eliminate the high amplitude Rayleigh wave arrivals from the seismograms. We define several windows for making measurements of the regional phase energy. The P_n window is a constant time window starting just ahead of the onset of P_n (we let the start time depend on the velocity model used) with a time length of 10 s; the L_g phase arrives in the 3.3-3.7 km/s velocity range. As can be seen from Figure 14, the P_n window is not very useful at distances closer than 4^o because other, higher energy phases (e.g. P_g) enter the window. The first distinct arrival outside this window is P_nP_n. P_g marks the onset of high frequency energy in between the P_n and L_g windows. The long-period component in the Lg window consists of low order Rayleigh wave modes. The onset of Rayleigh wave energy can be identified at a phase velocity of about 4.2 km/s. The higher frequency components superimposed on the long-period motions are the actual Lg energy.

The long-period Rayleigh wave signals are not recorded by the short-period instruments which are most commonly used to record regional waveforms. In order to simulate the response of such an instrument we convolve the synthetic displacement traces with the response of the Obninsk (OBN) Kirnos instrument, typical of instruments operating in the C.I.S.. The effect of this filtering in the frequency domain is shown in Figure 15. The frequency band of the instrument extends to about 8 Hz, leaving the high frequency component of the synthetics unchanged. The filtered waveforms are presented in Figure 16. The high frequency arrivals between the P_n and L_g windows have now become the largest arrivals in the seismograms. The long-period Rayleigh wave energy has disappeared from the L_g window and the P_n phase has become more impulsive and complex. Because many regional waveforms are now being recorded by broadband instruments we investigate propagation characteristics of the P_n and L_g phases for both the broadband and the short-period signals. We do this by calculating root mean square amplitudes for the 2 time windows as a function of epicentral distance.

Figure 17 shows the root mean square amplitudes in the P_n and L_g windows for the short-period waveforms generated with the 4 velocity models derived in this study. Amplitude differences for the average model WCH and model TP are very small for both P_n and L_g indicating that the higher P_n velocity of the latter model does not change the propagation characteristics of these phases significantly. At distances closer than 4^o the P_n window is contaminated by the inclusion of other phases in the rms window and we will therefore only comment on propagation characteristics at greater distances. Between 4^o and 10^o the increased amplitude of the P_n phase for model CHE relative to the average model WCH can be attributed to the reduced crustal thickness. The effect of the lower P wave velocity in the uppermost mantle for this model is to decrease the P_n amplitude because the increase in ratio between the source P wave velocity and the P_n velocity narrows the range of takeoff angles that will give a critical reflection at the Moho and thus more energy will be lost through radiation into the mantle. Thus, the effect of changes in crustal thickness appear more important than baseline shifts in lid velocity.

We would expect P_n amplitudes for model NCH to be lower than for model CHE because NCH has both a thicker crust and a lower P_n velocity. However, in contrast we find higher P_n amplitudes increasing with distance. These observations are explained by the positive velocity gradient in the lid for model NCH. The positive lid gradient causes less P_n energy traveling along the bottom side of the Moho to be lost through radiation into the upper mantle. Another effect is that energy that is almost critically reflected at the Moho and penetrates into the lid at near horizontal angles, turns at very shallow depth and can contribute to energy in the P_n window. This latter effect increases with distance accounting for the gain in P_n energy with distance. This increase seems to flatten off near 10^o indicating that effects of damping and geometrical spreading are becoming equally important. Though baseline shifts in P velocities in the uppermost mantle do

not influence P_n propagation characteristics very much, variations in lid velocity gradients can significantly change observed P_n amplitudes.

The small difference in L_g energy between models WCH and TP and the significant decrease for models NCH and CHE indicates that, like for P_n, crustal thickness is the most important factor controlling L_g energy, with a thicker crust being a better waveguide for this phase. Variations in lid velocities seem to have only a minor effect on the propagation of L_g. Although some scatter is visible, the propagation of L_g seems very stable and the amplitude decay with distance can be well matched by a simple power law equation. The powers of the distance decay rates are given in table 3. For the different models these range from 2.35 to 2.46. This range is in agreement with observations by Blandford (1981) who finds empirical L_g decay rates of r^{-3} for the active tectonic region of the western United States to r^{-2} for the stable eastern United States. Figure 17 further shows that differences in propagation for the different models can change P_n/L_g ratios by as much as an order of magnitude. At distances larger than 4^o P_n/L_g ratios increase with distance because the decay of L_g with distance is faster than that of P_n, with the slope of the increase depending on the difference in the decay rates of the 2 phases.

Figure 18 shows identical measurements for the broadband waveforms. The P_n amplitude curves for this case are much simpler. Except for model NCH they can all be characterized by simple power law decays (Table 4). Also, differences in rms P_n amplitudes for the different models are much smaller than for the short-period waveforms. The amplitude decay in the L_g window can again be characterized by power law equations (Table 3) with decay rates being significantly smaller than for the filtered waveforms. The long-period Rayleigh wave energy that now dominates in this window (Figure 14) damps out less rapidly than the higher frequency L_g modes. P_n/L_g ratios now uniformly decrease with distance, except for model NCH. The behavior of this decrease is fairly simple and the slope differences are governed by variations in the L_g decay rates. Depending on the structure of the crust and upper mantle P_n/L_g ratios for the broadband synthetics vary by a factor 5.

The short-period waveform behavior for the earthquake source is very similar to that of the explosion source (Figures 17 & 19), overall amplitudes of both the P_n and L_g phase are down by about a decade but relative differences between the different models are quite small. The most marked difference is the change in slope of the L_g decay for the north and east China models (Table 3). In these cases the P wave velocity near the source is larger than the S wave velocity in the uppermost mantle and the pS phase cannot be captured in the crust. Therefore the main contribution to the L_g phase will come from direct excitation of S wave energy. Because the L_g variations between models WCH and TP are small the effect of velocity changes in the uppermost mantle appear to not be very important. Crustal thickness is the major factor governing the strength of L_g. The markedly slower L_g amplitude decay for model NCH can be attributed to S wave

energy that is not critically reflected at the Moho turning in the uppermost mantle and contributing to the energy in this window. P_n/L_g ratios beyond 4^o are overall somewhat lower for the earthquake source than those for the explosion source, with a stronger effect for the east and north China models.

Comparison of Figures 18 and 20 shows that the broadband P_n behavior for the earthquake source is very similar to that of the explosion source. Overall, broadband P_n depends less on velocity structure than L_g. The low order Rayleigh waves which dominate the broadband L_g window exhibit a complex behavior. At close distances the energy in this window is lowest for models NCH and CHE but because the amplitude decay for these models is slower than that for models WCH and CHE they give higher amplitudes at distances greater than 7^o. Model dependence of P_n/L_g ratios in this case is very small.

For discrimination between earthquakes and underground nuclear explosions we would like the P_n/L_g variations between earthquake and explosion sources to be pronounced and to have a simple predictable behavior. For discrimination purposes P_n/L_g ratios are often expected to be higher for nuclear explosions than for earthquakes, mainly due to enriched high frequency P_n energy for explosions and enriched L_g for earthquakes. However, the real earth is not that simple. Indeed, several observational studies have either confirmed higher P_n/L_g ratios for earthquake sources (e.g. Blandford, 1981, Chan et al., 1990) or found that P_n/L_g ratios have much more complicated behavior (e.g. Lynnes & Baumstark, 1991). Shown in Figure 21 is the quotient of these ratios for the explosion and earthquake synthetics. Because we use identical paths for the earthquake and explosion source this quotient is mainly sensitive to source radiation differences. For the short-period frequency band the explosion/earthquake quotient ranges roughly between 1 and 3 at distances larger than 4^o. While we find that explosion P_n/L_g indeed is higher than earthquake P_n/L_g for all of the regionalized Chinese velocity models, we should keep in mind that this difference is much smaller than the variations in P_n/L_g ratios caused by propagation differences, which may differ by as much as a factor 10. Attempts to discriminate between underground nuclear explosions and earthquakes based on P_n/L_g ratios in the passband of our synthetics should therefore be undertaken with care. For the broadband frequency range the explosion/earthquake quotient can be both smaller or larger than 1 depending on the velocity structure, making this frequency range poorly suited for discrimination purposes.

5. Conclusions

This study has shown that the PP phase can effectively be used to model crustal and upper mantle P wave velocity characteristics. Long-period PP waveforms can be clearly discerned beyond 28^o; in broadband data this phase can be identified at distances down to 25^o. The strength

of precursors to PP can be used to interrogate the lid velocity gradients. Long-period direct P waveforms are not as sensitive to changes in upper mantle velocity as the PP phase, but details of observed P triplication behavior in broadband data can be used to put constraints on the velocity structure.

Long-period modeling has revealed that the average velocity structure of the crust and upper mantle under China is distinctive in character, and is intermediate between models for active tectonic regions and for stable shields. Our preferred average model, WCH, has a 50 km thick crust with a velocity of 6.4 km/s, a P_n velocity of 8.15 km/s and a low velocity zone between 100 km and 175 km depth. Velocities at greater depths are similar to those of other upper mantle velocity models. This model can match the majority of observed long-period waveforms in the 14^{o}-40^{o} distance range across China. However, with its thick crust and relatively high P_n velocity it is more characteristic of the fold belt region of western China, which is preferentially sampled by most of the paths used in this study. These two features contrast with the thinner crust and lower P_n velocities that are commonly observed for active tectonic regions.

Modeling of broadband waveforms gives evidence for significant lateral deviations from model WCH. Paths traversing eastern China indicate a constant velocity lid of about 100 km thickness, an observation in agreement with results of Holt & Wallace (1990) for southeastern China. The P_n velocity in this region ranges from 8.12-8.14 km/s and crustal thickness from 27-35 km. For northern China crustal thickness is between 43-50 km and a P_n velocity of about 8.0 km/s. There is some preliminary evidence for a strong lid with a positive velocity gradient of about 100 km thickness. For the Tibetan plateau we observe greater crustal thickness (50-60 km) and higher P_n velocity (8.15-8.25 km/s) in combination with a more pronounced low velocity zone than that of the average model WCH. Lower velocities may extend below 200 km depth. These results are similar to those of the S-wave velocity study of Lyon-Caen (1986) and indicate a thin weak lid of about 75 km thickness. We infer from our and previous results that crustal shortening and thickening is the most likely process to have given the Tibetan plateau its thick crust and high average elevation. The Indian plate has probably only slid under the southernmost part of the plateau. Mantle convection associated with the crustal shortening process has led to strong lateral heterogeneity in the upper mantle under Tibet. Higher P_n velocities in western Tibet confirm anomalously high Rayleigh wave phase velocities found by Brandon & Romanowicz (1986) and might indicate that this region is presently undergoing crustal shortening.

Variations in crustal and upper mantle velocity structure under China have a strong influence on the propagation of the P_n and L_g phases; P_n/L_g ratios vary by as much as an order of magnitude for the regionalized Chinese velocity models. Of the model variations explored, crustal thickness is the most important factor governing the propagation of L_g; P_n rms amplitudes are strongly affected by crustal thickness and variations in the lid velocity gradient. Baseline shifts in

velocities of the uppermost mantle have only a minor effect on the propagation of P_n and L_g. Although we did not explore the effect of variations in crustal velocity this is also likely to be an important factor in the propagation of these phases. Short-period L_g has very stable propagation characteristics; high frequency P_n rms amplitudes exhibit a more complicated behavior. For the regionalized Chinese velocity models, short-period P_n/L_g ratios for the explosive source are consistently higher than those for the earthquake source However differences in this ratio between the explosion source and the earthquake source are considerably smaller than variations in P_n/L_g ratio caused by propagation differences. Discrimination attempts based on this ratio should therefore be undertaken with care. Broadband P_n/L_g ratios for the explosion source can be both higher or lower than those for the earthquake source making this passband poorly suited for discrimination purposes.

Acknowledgments.
We thank George Zandt, Bill Walter and Chuck Ammon for helping us utilize computer resources at Lawrence Livermore National Laboratory. The IRIS data management center provided access to the data used in this study, Cray and Stellar computer time was provided courtesy of the Institute of Geophysics and Planetary Physics at Lawrence Livermore National Laboratory. This research was supported by the Department of the Air Force, monitored by the Phillips Laboratory under contract F19628-90-K-0041. Facilities support was provided by the W.M. Keck foundation. This is contribution number 213 of the Institute of Tectonics and the C.F. Richter Seismological Laboratory.

References

Argand, E., 1924. La tectonique de l'Asie. *Intl. Geol. Cong. Rep. Sess*, 13:170-372.

Barazangi, M. & Ni, J., 1982. Velocities and propagation characteristics of P_n and S_n beneath the Himalayan and the Tibetan plateau: Possible evidence for underthrusting of Indian continental lithosphere under Tibet. *Geology,* 10: 179-185

Blandford, R.R., 1981 Seismic discrimination problems at regional distances. *NATO Advanced Study Institutes Series C*, Mathematical and Physical Sciences: 695-740.

Black, P.R. and Braille, L.W., 1982. P_n velocity and cooling of the continental lithosphere. *J. Geophys. Res.*, 87:10557-10568.

Bourjot, L. and Romanowicz, B., 1992. Crust and upper mantle tomography in Tibet using surface waves. *Geophys. Res. Lett.*, 19: 881-884.

Brandon, C. and Romanowicz, B., 1986. A "no lid" zone in the central Chang Thang platform of Tibet: Evidence from pure path velocity measurements of long-period Rayleigh waves, *J. Geophys. Res,*, 91: 6547-6564.

Burdick, L.J., 1981. A comparison of the upper-mantle structure beneath North America and Europe. *J. Geophys Res.*, 86: 5926-5936.

Burdick, L.J. and Helmberger, D.V., 1978. The upper mantle P velocity structure of the western United States. *J. Geophys Res.*, 83 : 1699-1712.

Burdick, L.J. and Orcutt, J., 1979. A comparison of the generalized ray and reflectivity methods of waveform synthesis. *Geophys. J. R. Astron. Soc.*, 58: 261-278.

Chan, W.W., Baumstark, R. and Cessaro, R.K., 1990. Spectral discrimination between explosions and earthquakes in central Eurasia. *Phillips Laboratory Annual Scientific Report*, GL-TR-90-0217:1-38, ADA 230048.

Chapman, C.H., 1978. A new method for computing synthetic seismograms. *Geophys. J. R. Astron. Soc.*, 57: 649-670.

Chapman, C.H. and Orcutt, J., 1985. The computation of body-wave synthetic seismograms in laterally homogeneous media. *Rev. Geophys*, 23: 105-163.

Chen W.P. & Molnar, P., 1975. Short-period Rayleigh wave dispersion accross the Tibetan plateau. *Bull. Seism. Soc. Am*, 65:1051-1057.

Chen, W.P. & Molnar, P., 1981. Constraints on the seismic wave velocity beneath the Tibetan plateau and their tectonic implications. *J. Geophys Res.*, 86 : 5937-5962

Chun, K.Y. and Yoshi, T., 1977. Crustal structure of the Tibetan plateau: A surface wave analysis. *Bull. Seism. Soc. Am*, 67:735-750.

England, P.C. and Houseman, G.A., 1986. Finite strain calculations of continental deformation. II. Comparison with the India-Asia collision. *J. Geophys. Res.*, 91:3664-3676.

Frankel, A., 1989. Effects of source depth and crustal structure on the spectra of regional phases determined from synthetic seismograms. *DARPA/AFTAC Annual Seismic Research Review*, FY 89: 97-118.

Fuchs, K. and Müller, G., 1971. Computation of synthetic seismograms with the reflectivity method and comparison with observations. *Geophys. J. R. Astron. Soc.*, 23: 417-433.

Gansser, A., 1980. The signification of the Himalayan suture zone. *Tectonophysisc*, 62:37-52.

Garnero, E.J., Helmberger, D.V. and Burdick, L.J., 1992. Preliminary observations from the use of US-Soviet joint seismic program data to model the upper mantle triplications beneath Asia. *Geophys. J. Int.*, 113:252-259.

Given, J.W., and Helmberger, D.V., 1980, Upper mantle structure of Northwestern Eurasia. *J. Geophys Res.*, 85: 7183-7194.

Goldstein, P., Walter, W. R. and Zandt, G. Upper mantle structure beneath central Eurasia using a source array of nuclear explosions and waveforms at regional distances. *J. Geophys Res.*, 97:14097-14113.

Grand, S.P. and Helmberger, D.V., 1984. Upper mantle shear structure of North America. *Geophys. J. R. Astron. Soc.*, 76: 399-438.

Grand, S.P. and Helmberger, D.V., 1985. Uppermantle shear structure beneath Asia from multibounce S waves. *Phys. Earth and Planet. Interiors.*, 41: 154-169.

Gutowski, P.R., Hron, F., Wagner, D.E. and Treitel, S., 1984. S^*, *Bull. Seism. Soc. Am.*, 74:61-78.

Holt, W.E. and Wallace, T.C., 1990. Crustal thickness and upper mantle velocities in the Tibetan plateau region from the inversion of Regional P_{nl} waveforms: evidence for a thick upper mantle lid beneath southern Tibet. *J. Geophys Res.*, 95: 12,499-12,525.

Israelsson, H., 1992. RMS L_g as a yield estimator in Eurasia, *Phillips Laboratory Final Report*, PL-TR-92-2117(I), ADA 256692.

Jobert, N., Journet, B., Jobert, G., Hirn, A. and Zhone, S. K., 1985. Deep structure of southern Tibet inferred from the dispersion of Rayleigh waves through a long-period seismic network, *Nature*, 313:386-388.

King, D.W. and Calcagnile, G., 1976. P-wave velocities in the upper mantle beneath Fennoscandia and western Russia. *Geophys. J. R. Astron. Soc.*, 46: 407-432.

Lefevre, L.V. and Helmberger, D.V., 1989. Upper mantle P velocity of the Canadian Shield. *J. Geophys Res.*, 94: 17749-17765.

Lynnes, C. and Baumstark, R., 1991. Phase and spectral ratio discrimination in North America. *Phillips Laboratory Final Report*, PL-TR-91-2212(II): 1-68, ADA 246673.

Lyon-Caen, H., 1986. Comparison of the upper mantle shear wave velocity structure of the Indian shield and the Tibetan plateau and tectonic implications. *Geophys. J. R. Astron. Soc.*, 86:727-749.

Mangino, S. and Ebel, J. 1992. The receiver structure beneath the Chinese digital seismograph network (CDSN) stations: preliminary results. *Phillips Laboratory Annual Scientific Report*, PL-TR-92-2149:1-93, ADA 256681.

Menke, W.H. and Richards, 1980. Crust mantle whispering gallery phases: a deterministic model of teleseismic Pn wave propagation. *J. Geophys Res.*, 85: 5416-5422.

Molnar, P., 1988. A review of geophysical constraints on the deep structure of the Tibetan plateau, the Himalaya and the Karakoram, and their tectonic implications. *Philos. Trans. R. Soc. London*, ser A, 326:33-88.

Molnar, P. and Chen, W.P.,1984. S-P wave travel time residuals and lateral inhomogeneity in the mantle beneath Tibet and the Himalaya. *J. Geophys Res.*, 89: 6911-6917.

Mooney, W.D., 1992. Complilation of several Chinese deep refraction studies , in preparation (personal communication).

Mooney, W.D., and Braille, L.W., 1989. The seismic structure of the continental crust and upper mantle of North America, in Bally, A.W. and Palmer, A.R., eds, *The geology of North America-An overview*, vol A:39-52.

Neele, F. and Snieder, R., 1991. Are long-period body wave coda caused by lateral inhomogeneity? *Geophys. J. Int.*, 107: 131-153.

Ni, J. and Barazangi, M., 1983. High frequency seismic wave propagation beneath the Indian shield, Himalayan arc, Tibetan plateau and surrounding regions: High uppermost mantle velocities and efficient S_n propagation beneath Tibet, *Geophys. J. Royal. Astron. Soc.*, 72: 665-689.

Patton, H.,1980. The crust and upper mantle structure of the Eurasian continent from the path velocity measurements and Q of surface waves. *Rev Geophys.*, 18: 605-625.

Paulssen, H., 1987. Lateral heterogeneity of Europe's upper mantle as inferred from modelling of broad band body waves. *Geophys. J. Royal. Astron. Soc.*, 91: 171-199.

Ringdal, F., 1991. RMS L_g analysis of Novaya Zemblya explosion recordings. in: Semiann Tech. Summ., 1 Oct 90 - 31 Mar 91, *NORSAR Sci. Rep.* 2-90/91, Kjeller, Norway.

Romanowicz, B.A., 1982. Constraints on the structure of the Tibet plateau from pure path velocities of Love and Rayleigh waves. *J. Geophys. Res.*, 87:6865-6883.

Romanowicz, B.A., 1984. Pure path attenuation measurements of long-period Rayleigh waves across the Tibet plateau. *Phys. Earth Planet. Inter.*, 36:116-123.

Schwartz, S.Y. and Lay, T., 1993. Complete PP-waveform modeling for determining crust and upper mantle structure. *Geophys. J. Int.*, 112:210-224.

Vinnik, L.P. and Saipbekova, A. M., 1984. Structure of the lithosphere and asthenosphere of the Tien Shan. *Annal Geophysicae*, 2: 621-626.

Wang, K. and Yao, Z.X., 1989. Preliminary study of upper mantle shear velocity structure of China. *Chinese J. Geophys.*, 32:49-60 (English edition published by Allerton Press Inc., New York).

Xie, X.B. and Lay, T., 1993. The excitation of explosion L_g, a finite-difference inverstigation, in preparation.

Yuan, X., Wang, L. Li. and Zhu, J., 1986. A global investigation of the deep structure in China, in Reflection seismology, A global perspective, *Geodynamics Series Volume 13,* American geophysical Union, Publication 0112, 151-160.

Zhao, L.S., Helmberger, D.V. and Harkrider, D.G., 1991. Shear velocity structure of the crust and upper mantle beneath the Tibetan plateau and southeastern China, *Geophys J. Int.*, 105:713-730.

Zhao, L.S. and Xie, J., 1993. Lateral variations in compressional velocity beneath the Tibetan plateau from P_n travel-time tomography. To be submitted to JGR.

Table 1. Earthquake source parameters

event no	date	lat (deg)	lon (deg)	depth (km)	strike/dip/rake (degs)	dur (sec)	mb
1	07/23/88	48.72	90.51	13	345/72/180[2]	2.8	5.5
2	08/20/88	26.78	86.61	57	230/23/2[1]	3.0	6.4
3	04/15/89	29.98	99.24	10	273/29/-73[1]	5.0	6.2
4	04/20/89	57.14	121.92	28	6/56/170[1]	4.7	6.0
5	04/25/89	30.04	99.45	10	273/29/-73[2]	2.4	6.1
6	05/03/89	30.07	99.48	17	273/29/-73[2]	5.2	5.9
7	01/14/90	37.77	91.89	8	302/82/105[2]	2.0	6.1
8	03/05/90	36.85	73.01	17	192/36/-46[1]	5.0	5.8
9	06/14/90	47.89	85.12	32	33/75/1[2]	6.5	6.2
10	08/03/90	47.95	84.96	34	113/53/173[1]	2.4	6.1
11	01/05/91	23.48	95.98	13	20/70/110[2]	3.0	6.3
12	10/19/92	30.85	78.79	16	112/78/84[1]	7.0	6.4
13	08/19/92	42.10	73.54	30	245/34/70[1]	6.0	6.8

Event locations and magnitudes from NEIC, depths and source durations (dur) from waveform modeling, focal mechanisms from 1) Harvard CMT and 2) waveform modeling.

Table 2. Model WCH

depth(km)	vel(km/s)	depth(km)	vel(km/s)
0.000	6.400	270.000	8.500
50.000	6.400	280.000	8.540
50.000	8.150	290.000	8.580
100.000	8.150	300.000	8.620
110.000	8.140	310.000	8.645
120.000	8.125	320.000	8.670
130.000	8.110	330.000	8.695
140.000	8.090	340.000	8.720
150.000	8.065	350.000	8.747
160.000	8.050	360.000	8.775
170.000	8.050	370.000	8.799
180.000	8.100	380.000	8.823
190.000	8.165	390.000	8.847
200.000	8.215	400.000	8.872
210.000	8.262	405.000	8.883
220.000	8.305	420.000	8.910
230.000	8.347	420.000	9.240
240.000	8.380	431.000	9.292
250.000	8.420	442.000	9.333
260.000	8.460	452.000	9.375

Table 3. Value of b for fit of $y=a \cdot x^b$ to L_g decay curves

source type	frequency band	WCH	Tibetan plateau	east China	north China
explosion	short-period	-2.38	-2.33	-2.46	-2.35
explosion	broadband	-1.70	-1.68	-1.08	-1.36
earthquake	short-period	-2.41	-2.42	-2.09	-1.81
earthquake	broadband	-1.69	-1.73	-1.81	-1.26

Table 4. Value of b for fit of $y=a \cdot x^b$ to P_n decay curve

source type	frequency band	WCH	Tibetan plateau	east China
explosion	broadband	-2.78	-2.86	-2.44
earthquake	broadband	-2.80	-2.79	-2.41

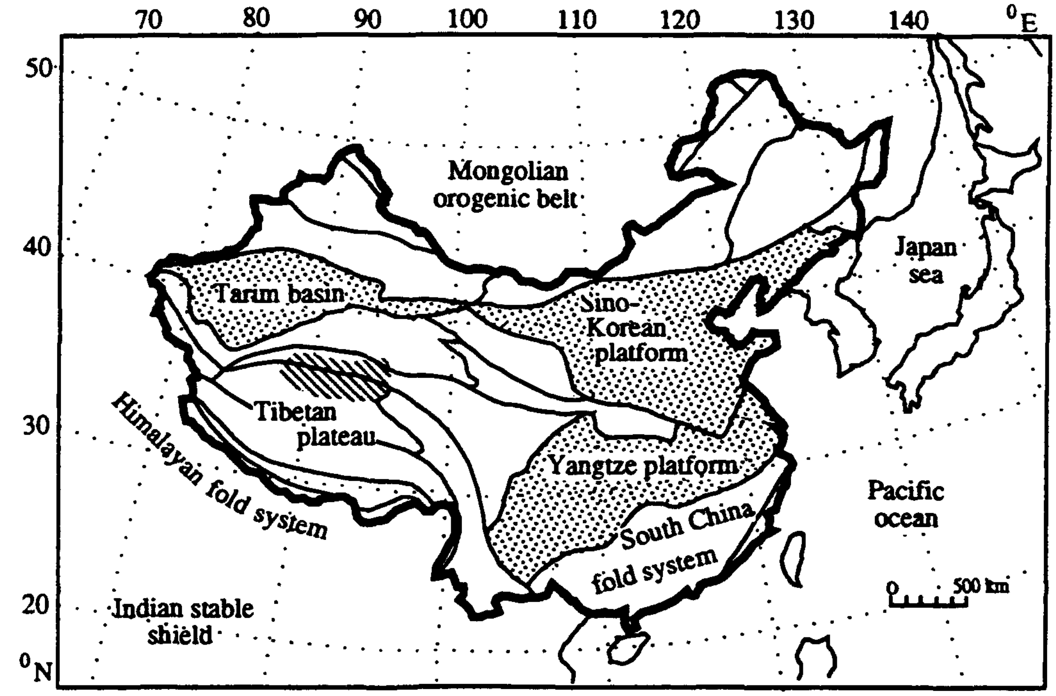

Figure 1. Tectonic structure sketch of China. Outlines of tectonic provinces are from Mooney (1992). Basin and platform material is shown in grey scale, active fold belts in white. The Chang Thang region in north-central Tibet which is characterized by Quaternary volcanism is indicated by the hatched lines.

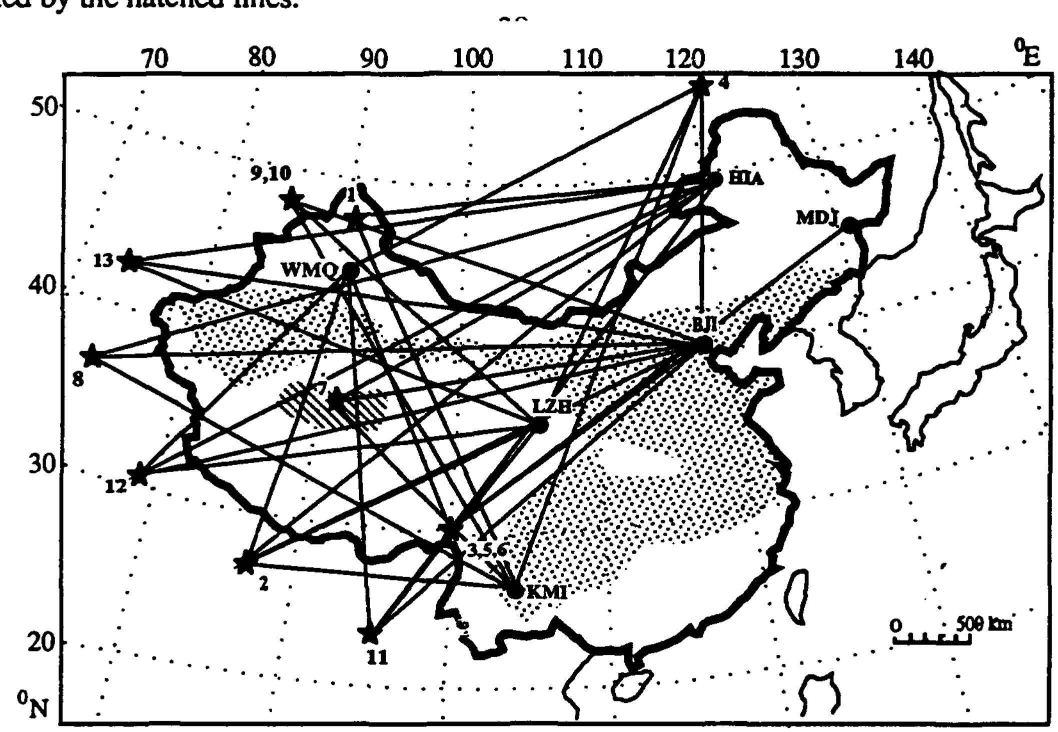

Figure 2. Map showing event locations (stars), CDSN broadband stations (circles with station codes) and paths used in this study. Tectonic areas are the same as in Figure 1. Event numbers correspond with those of Table 1.

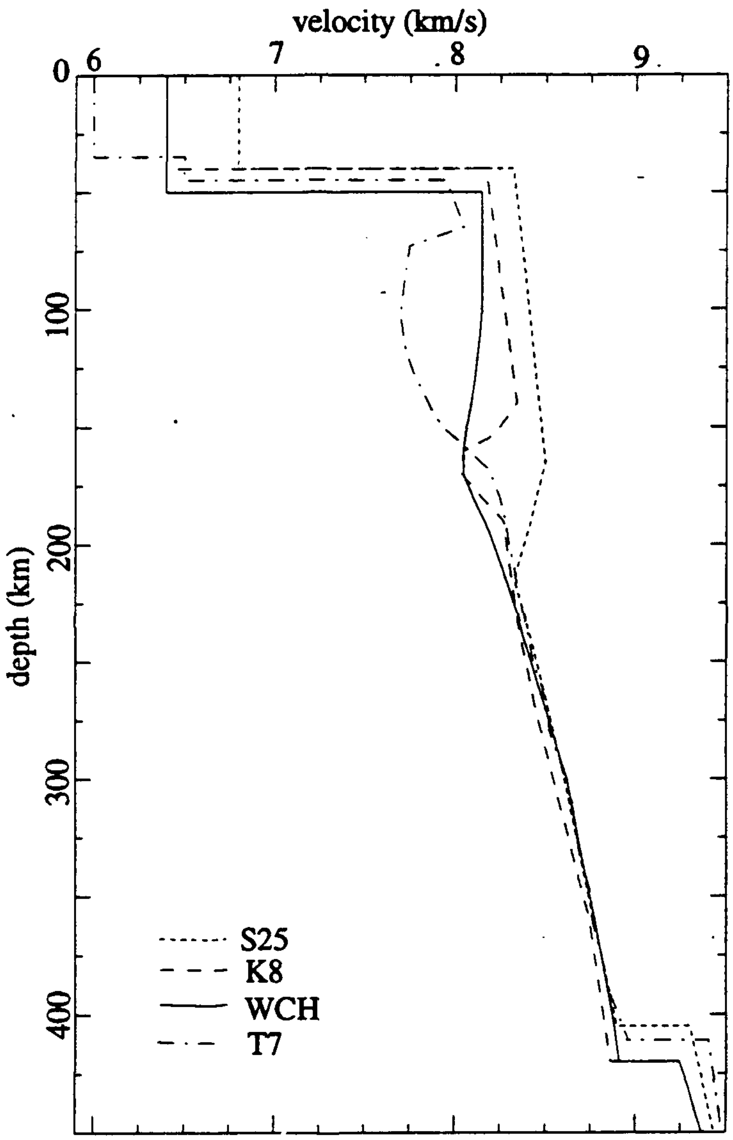

Figure 3. Suite of P wave velocity models used for initial long-period modeling.

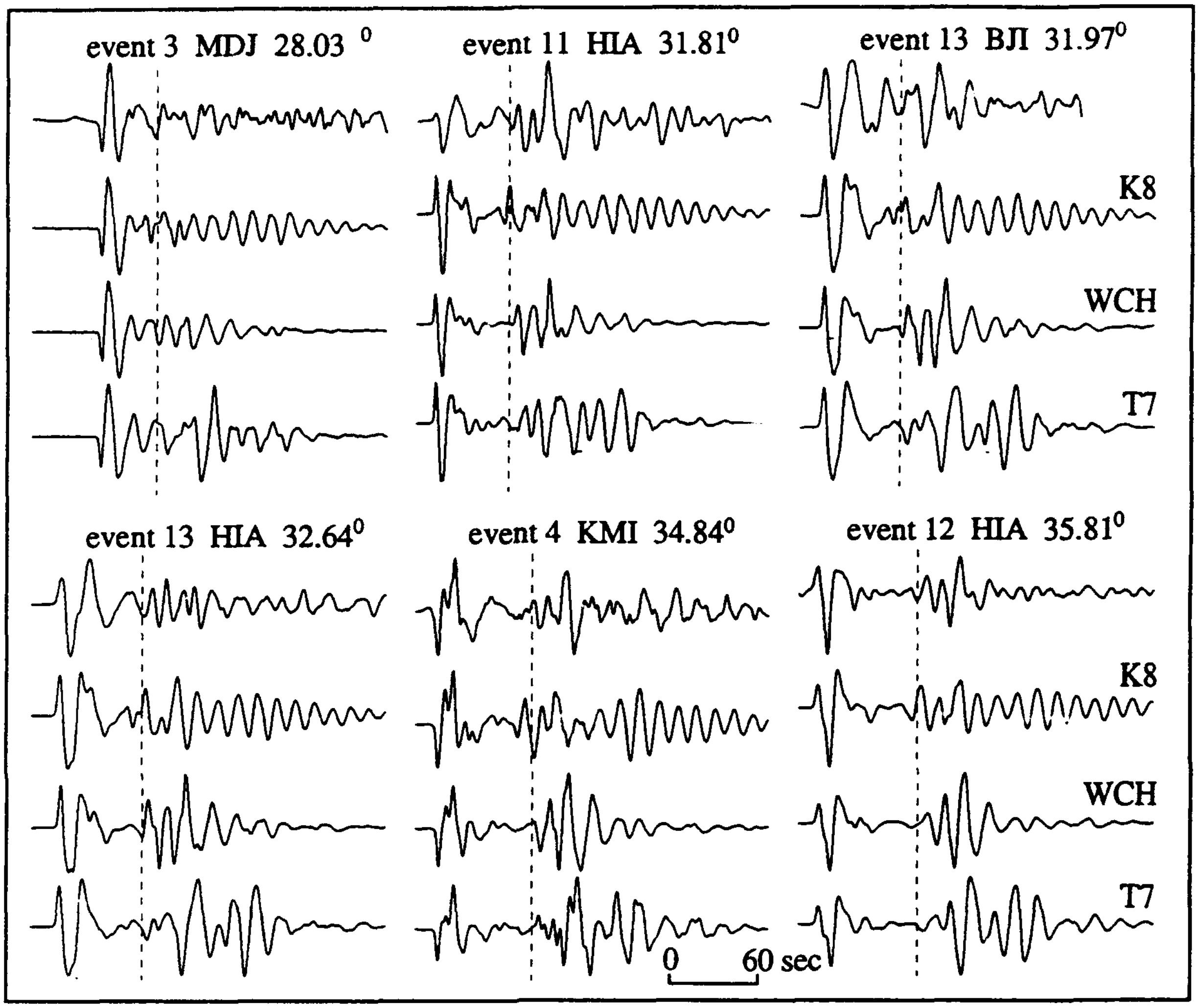

Figure 4. Comparison between observed and synthetic long-period P and PP waveforms for the velocity models shown in Figure 3 at PP triplication distances. Model WCH best matches general characteristics of these waveforms for paths traversing different tectonic regions. The first arrival of PP energy as picked from the data is indicated by the dashed vertical line. The corresponding paths can be identified from Figure 2.

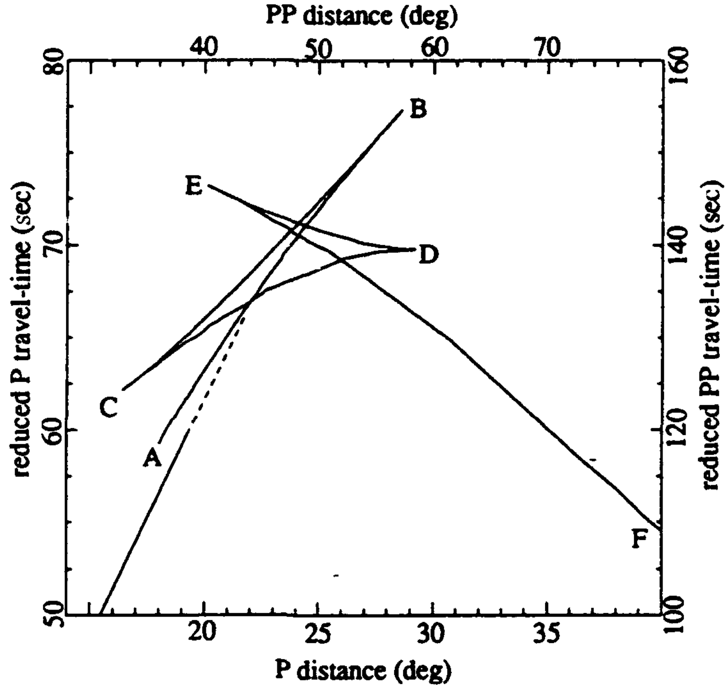

Figure 5. P and PP travel-time curve calculated for the first order model WCH and a surface source. The reduction velocity is 10 km/s. Triplication branches associated with the 420 and 670 km discontinuities are denoted in their normal convention. The dashed branch results from the low velocity zone triplication and has negligible energy associated with it.

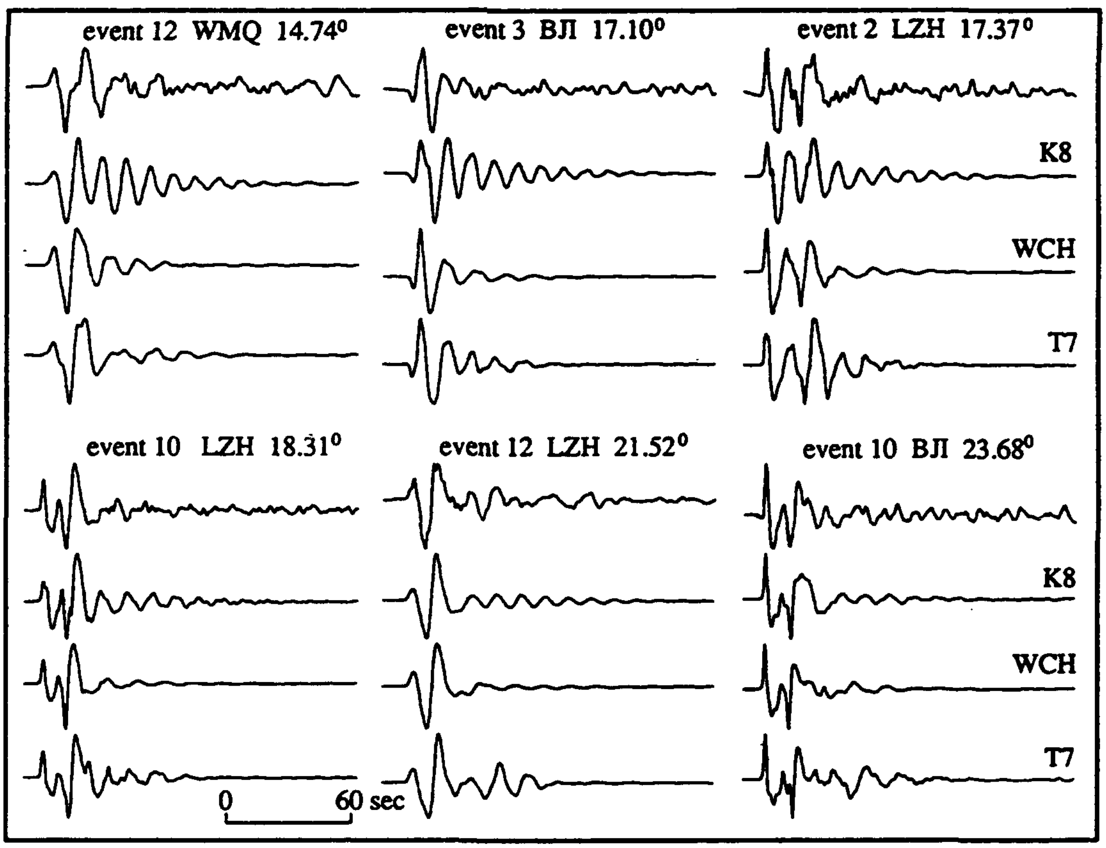

Figure 6. Comparison between observed and synthetic long-period P triplication waveforms for the velocity models shown in Figure 3 illustrating that model WCH can also match characteristics of these waveforms for paths throughout the China region.

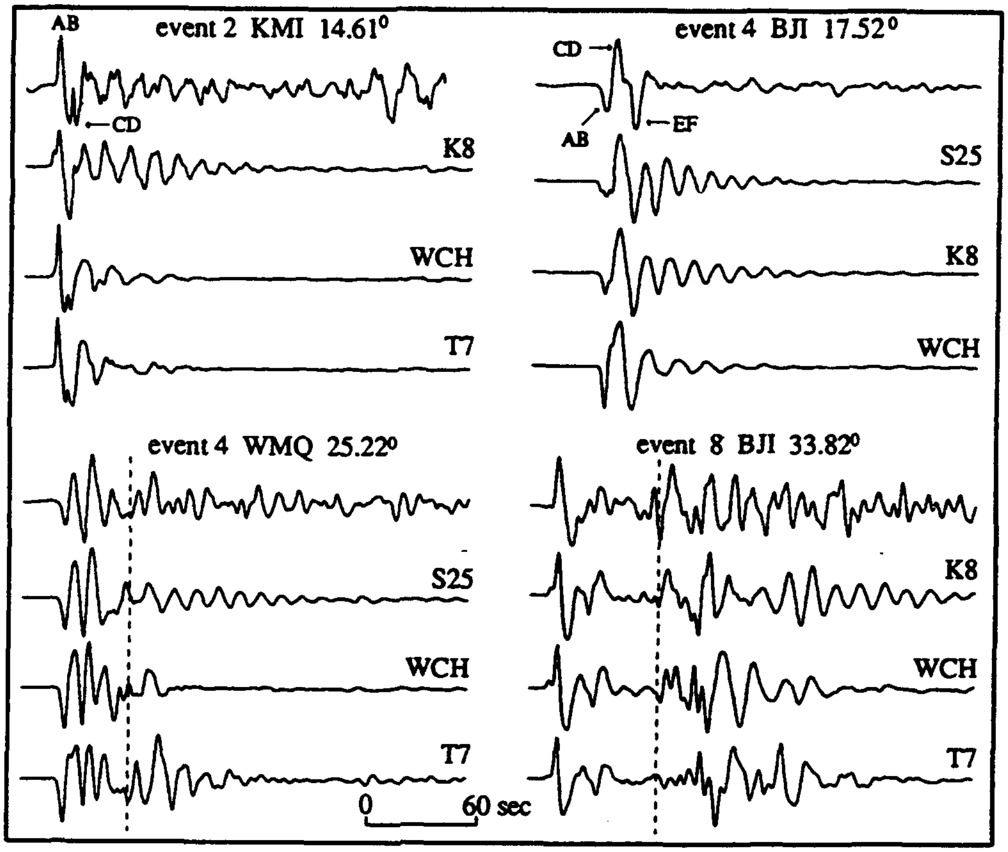

Figure 7. Similar comparisons to those of Figures 4 and 6 showing that deviations from the average velocity model WCH may be expected in the upper mantle under China. The first arrival of PP energy as picked from the data is indicated by the dashed vertical line. Branches of the P triplication arrivals correspond to those in Figure 5.

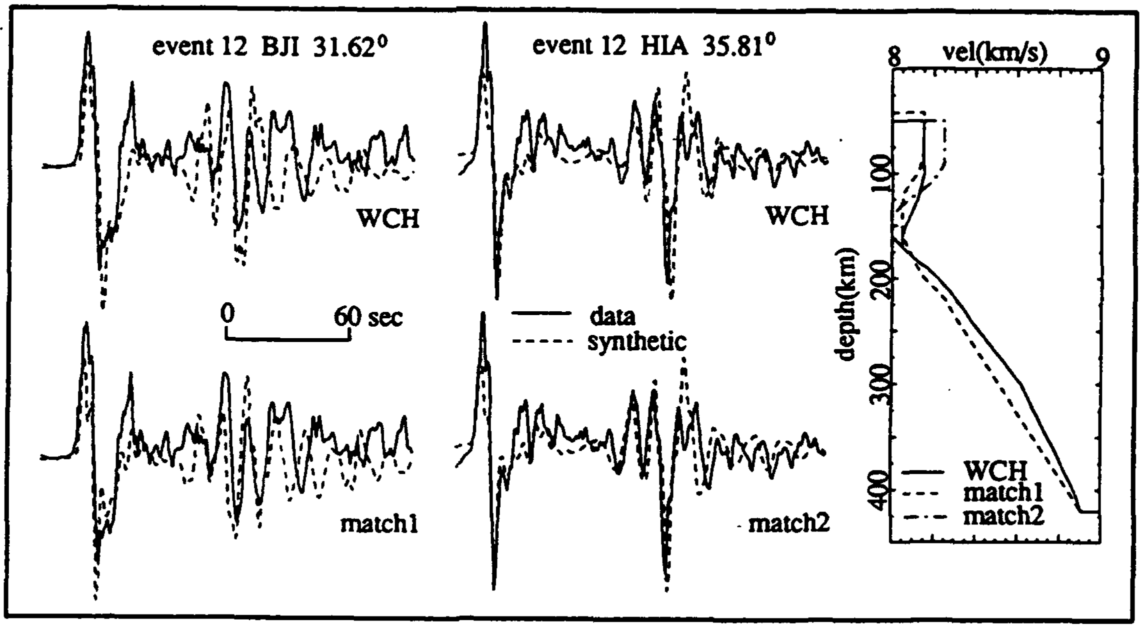

Figure 8. Comparison of observed and synthetic broadband P and PP waveforms for paths mainly traversing the Tibetan plateau. This illustrates that precursors to PP can be used to infer lid velocity gradients. Models used to generate synthetics are shown in the velocity profile.

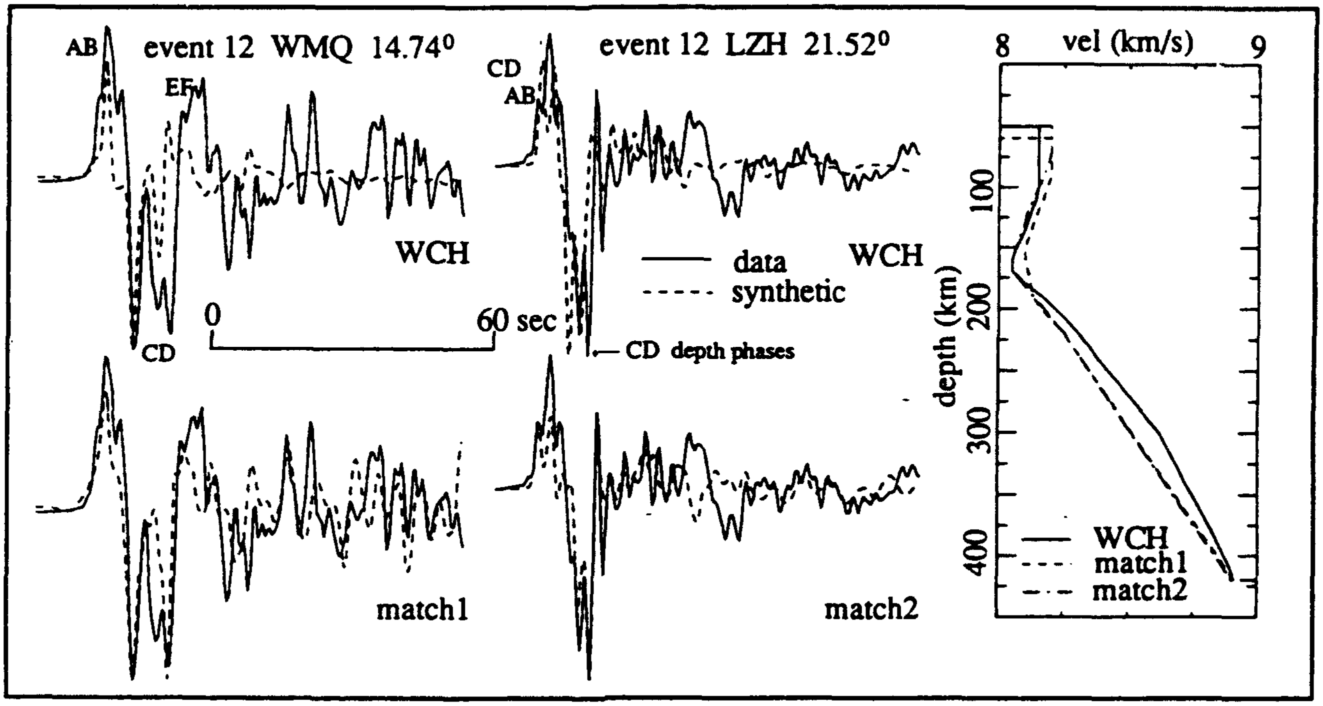

Figure 9. Similar comparison as Figure 8 for broadband P waveforms to show that the upper mantle under Tibet can be characterized by higher Pn velocities and lower velocities below 200 km depth relative to the average model WCH.

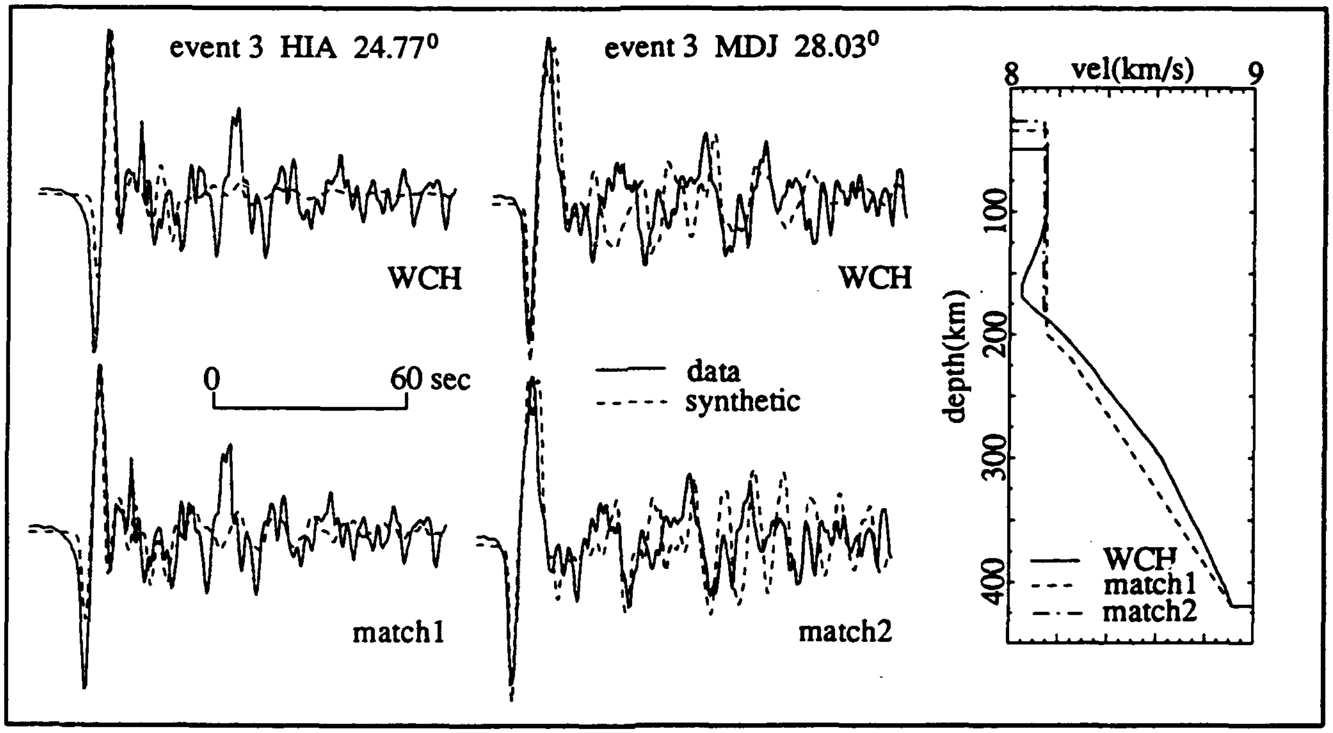

Figure 10. Same as Figure 8 but now for paths traversing eastern China. This region is characterized by a constant velocity lid and Pn velocities that are somewhat lower than those of model WCH.

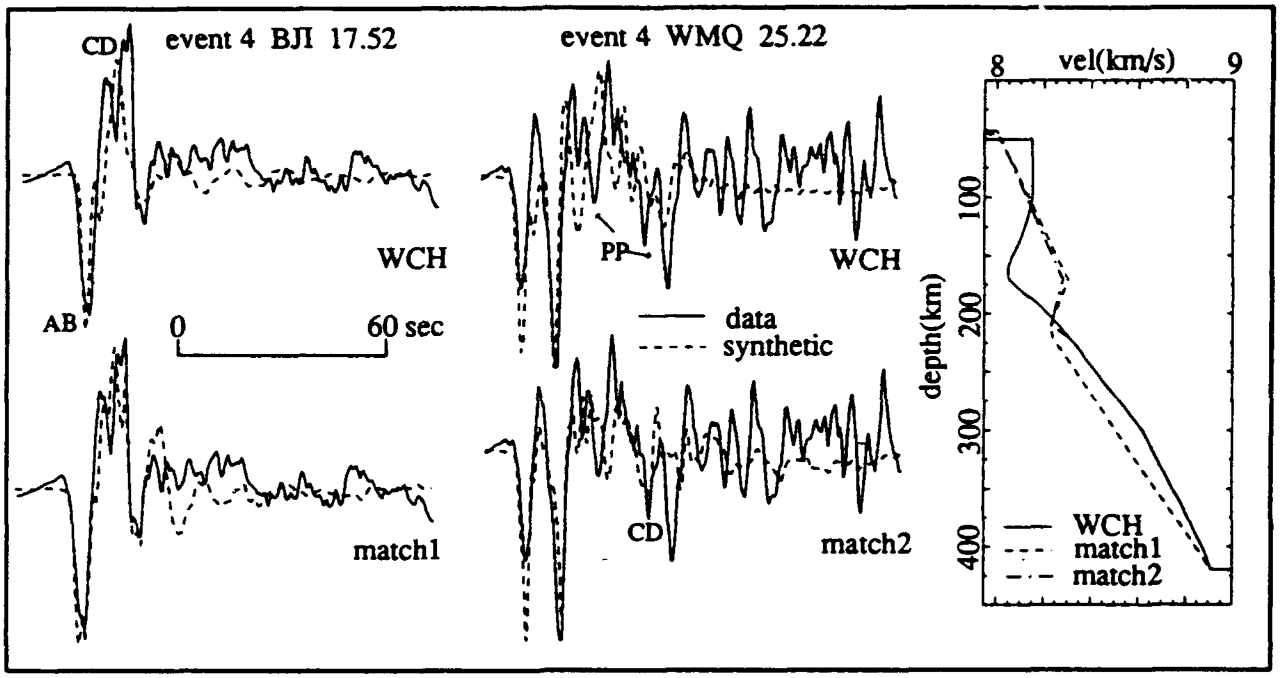

Figure 11. Similar comparison to that of Figure 8 for paths traversing the northern Chinese and Mongolian fold belts. These paths indicate a positive velocity gradient in the lid in combination with lower Pn velocities than those of model WCH.

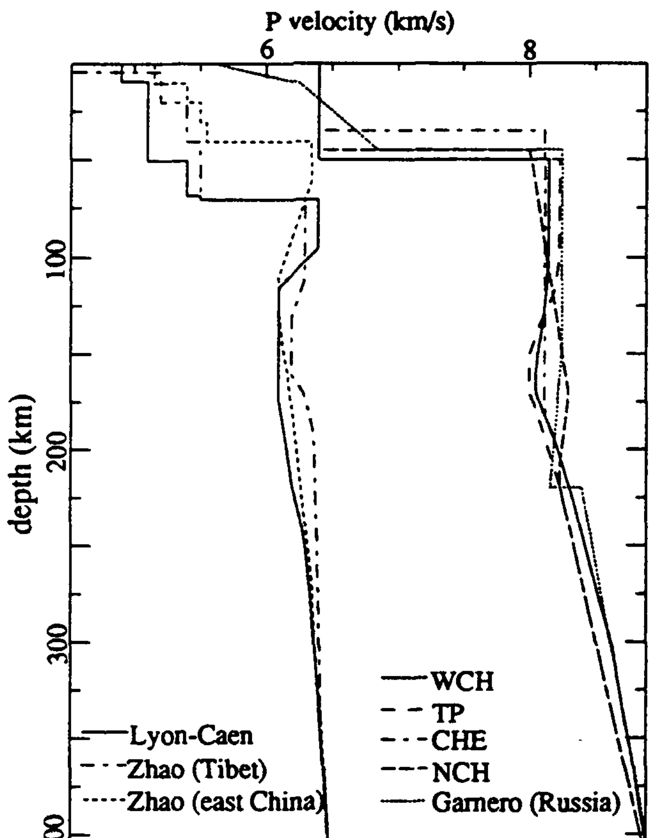

Figure 12. Comparison of the regionalized P wave velocity models derived in this study with P and S wave velocity models from previous studies.

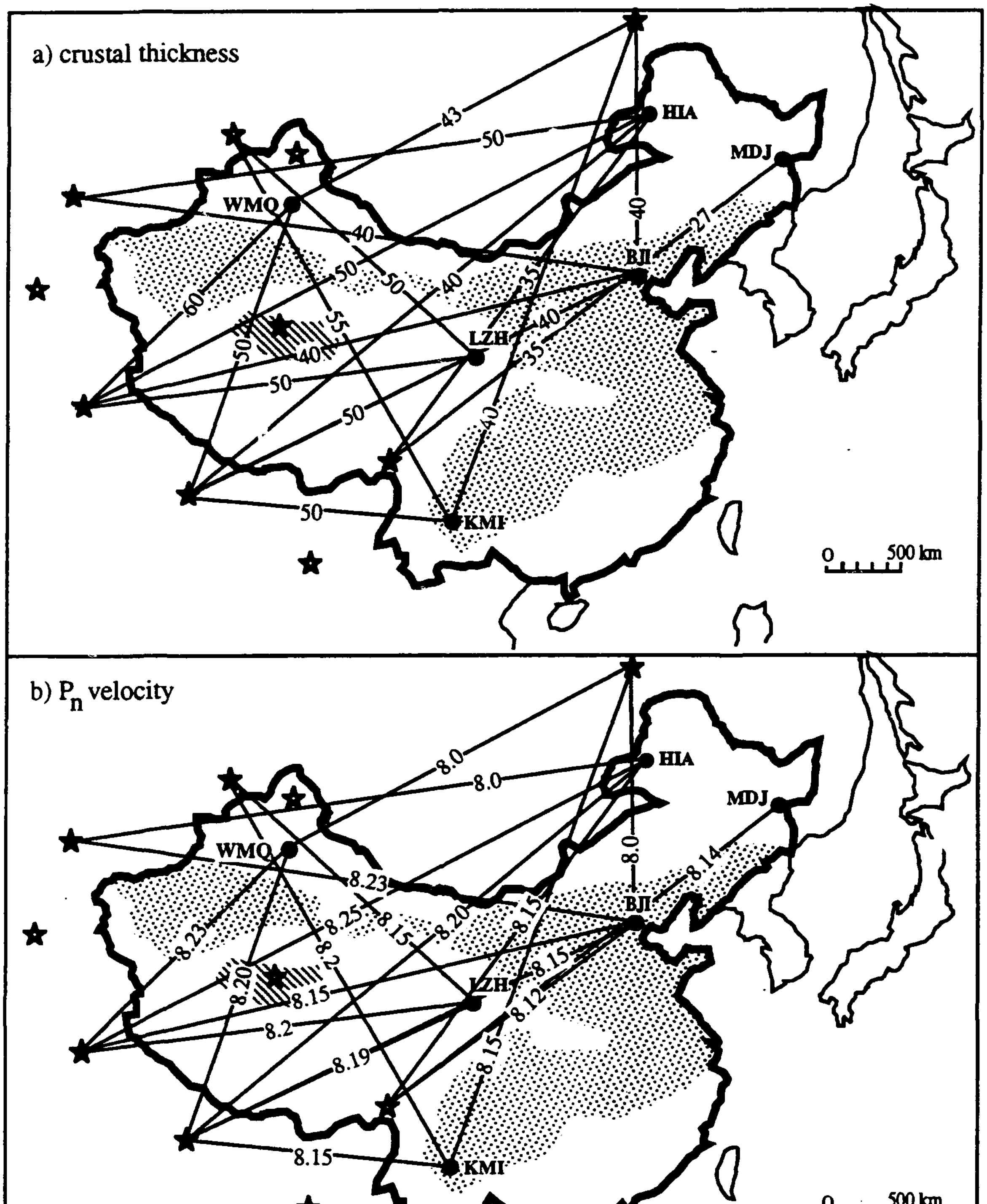

Figure 13. Summary of crustal and upper mantle characteristics under China at 4 depth ranges as derived from broadband waveform modeling. Tectonic areas correspond to those in Figure 1.

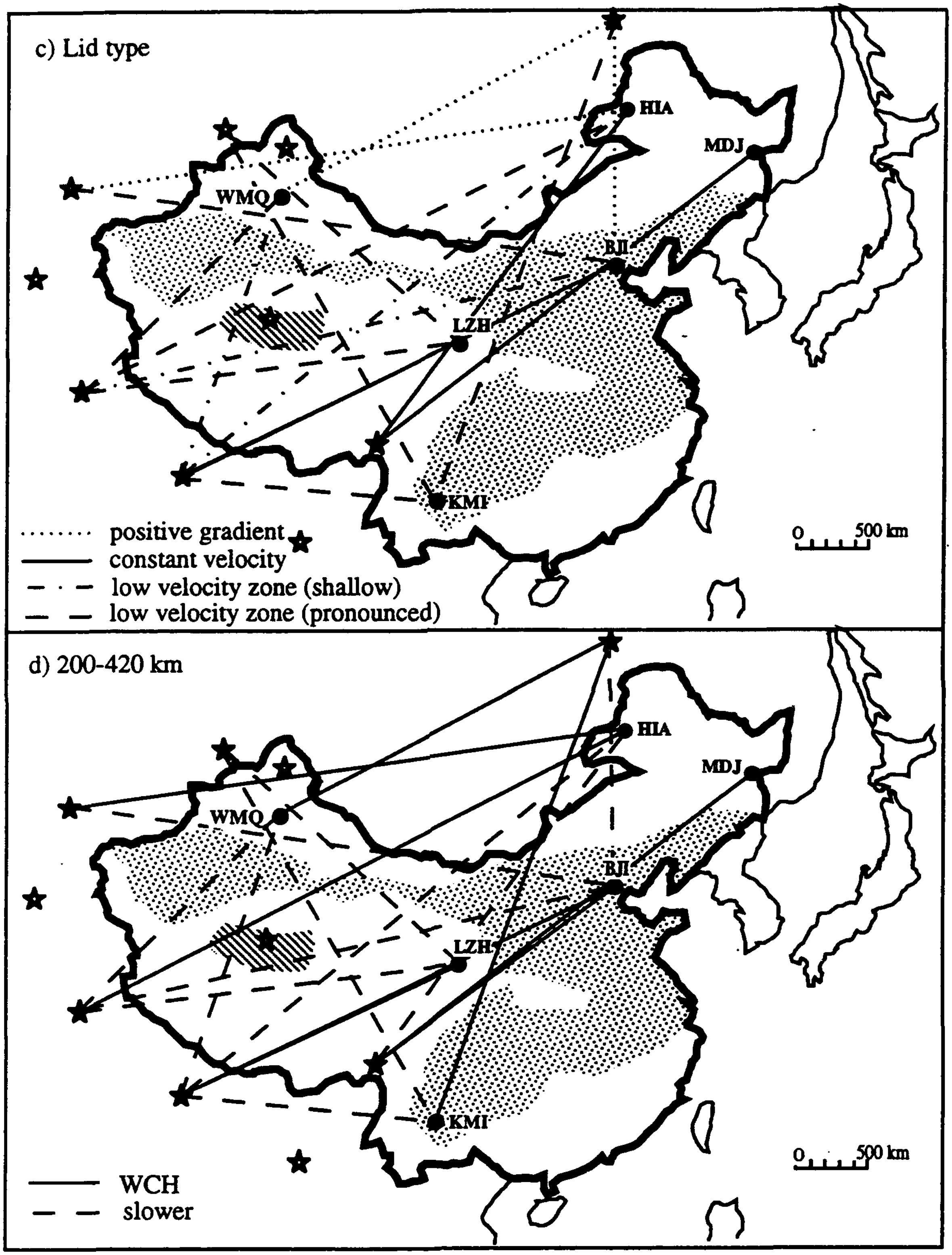

Figure 13 cont.

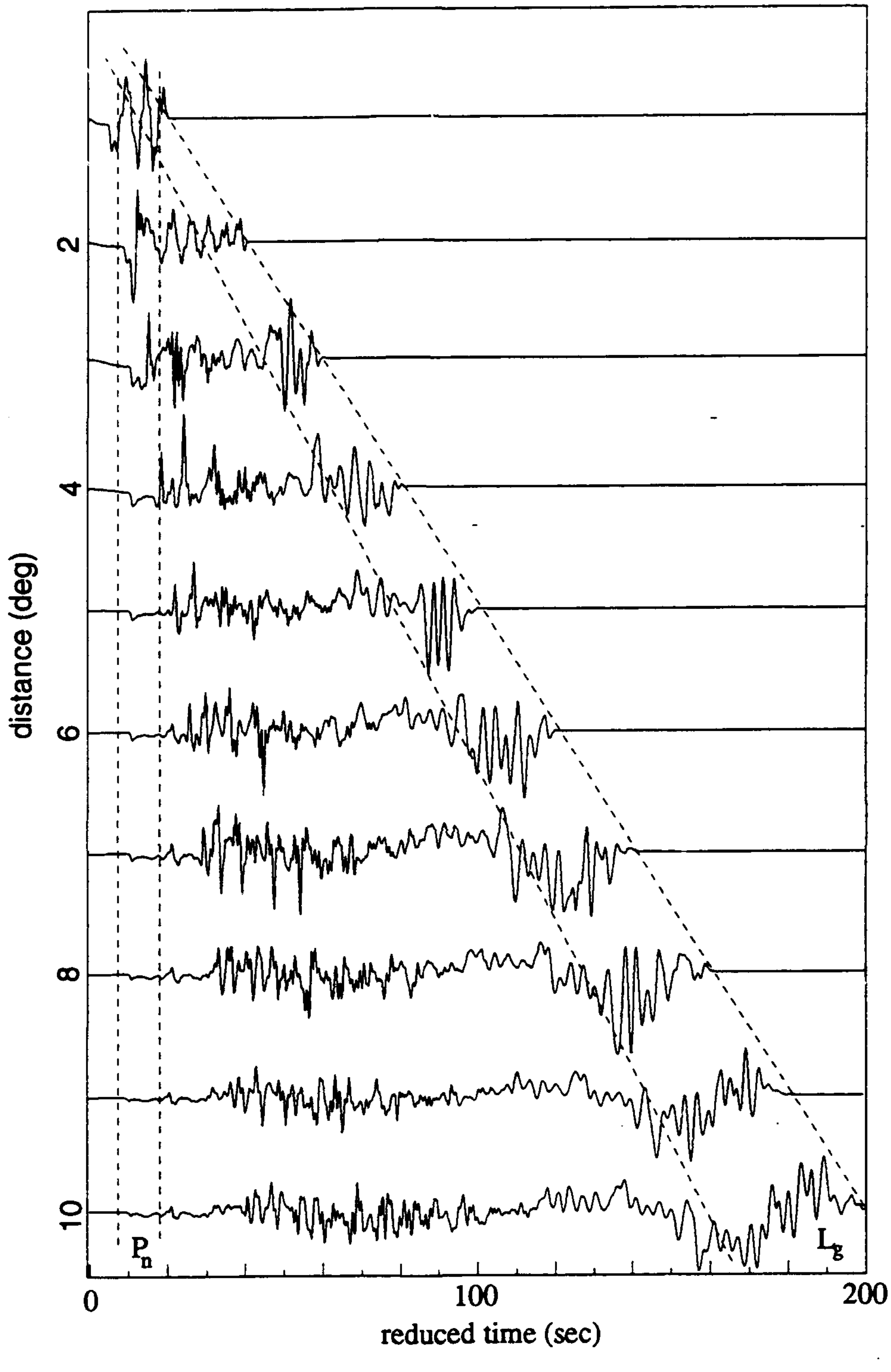

Figure 14. Synthetic broadband waveforms generated with model WCH and the explosive source. All traces are normalized to their maximum amplitude. The reduction velocity of 8.2 km/s aligns the P_n arrivals at almost constant time. The P_n and L_g windows used for the rms amplitude calculations are bounded by the dashed lines.

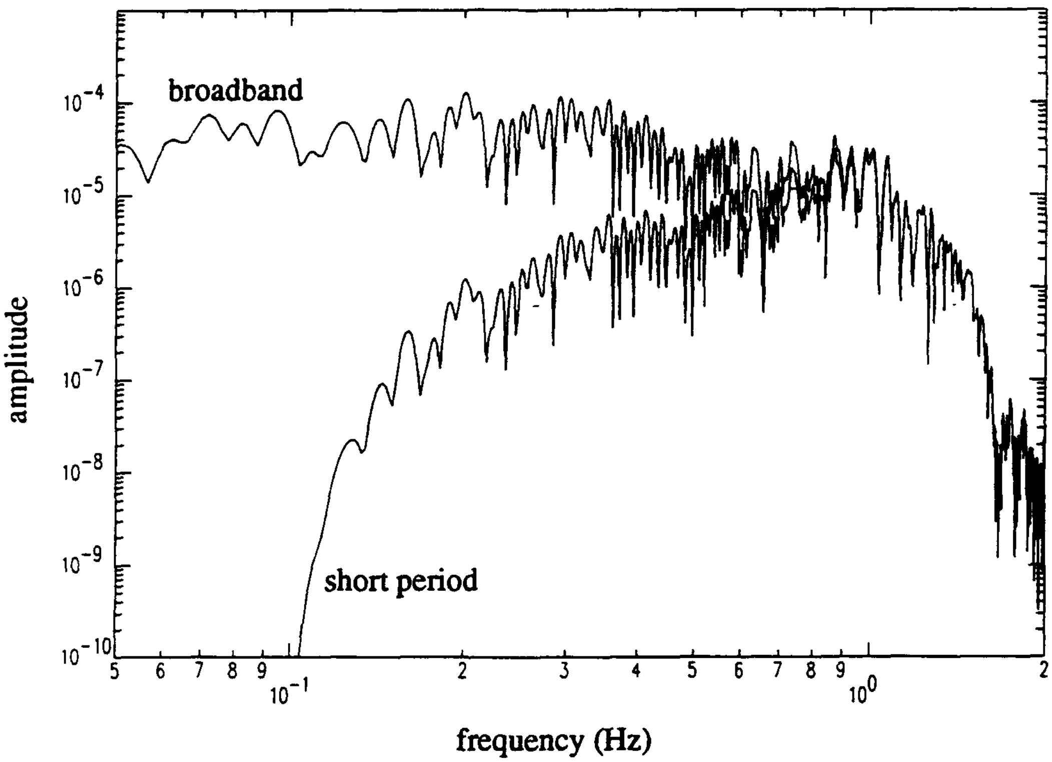

Figure 15. Spectra of the broadband synthetic waveform at 7° of Figure 14, and the same waveform filtered with the OBN Kirnos instrument. This illustrates the effect of the short-period filtering on the frequency content of the synthetic waveforms.

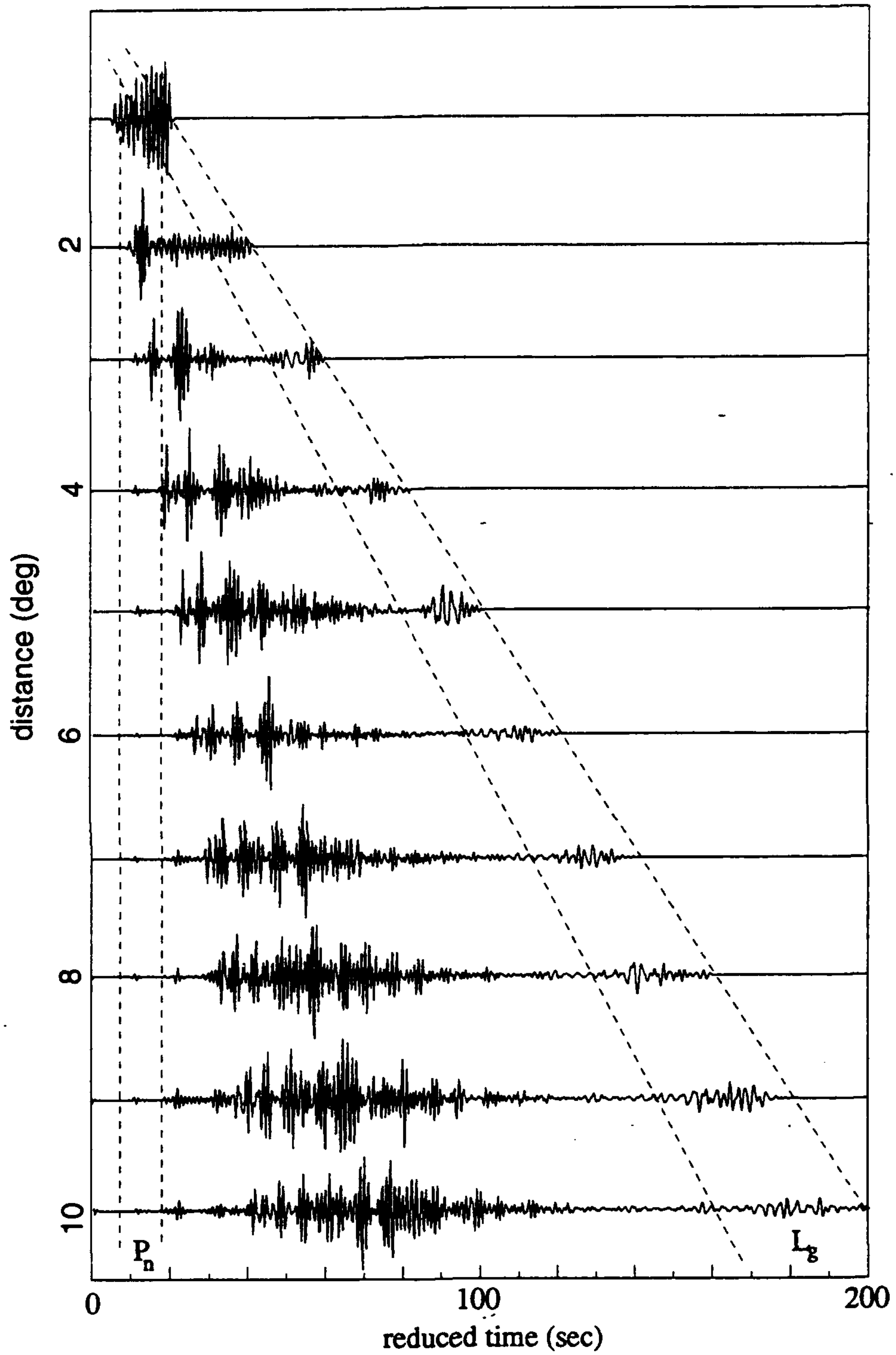

Figure 16. Same as Figure 14 but now for the waveforms filtered with the short-period response. Long-period Rayleigh wave modes have dissappeared from the L_g window and the P_n arrival has become more impulsive and complex.

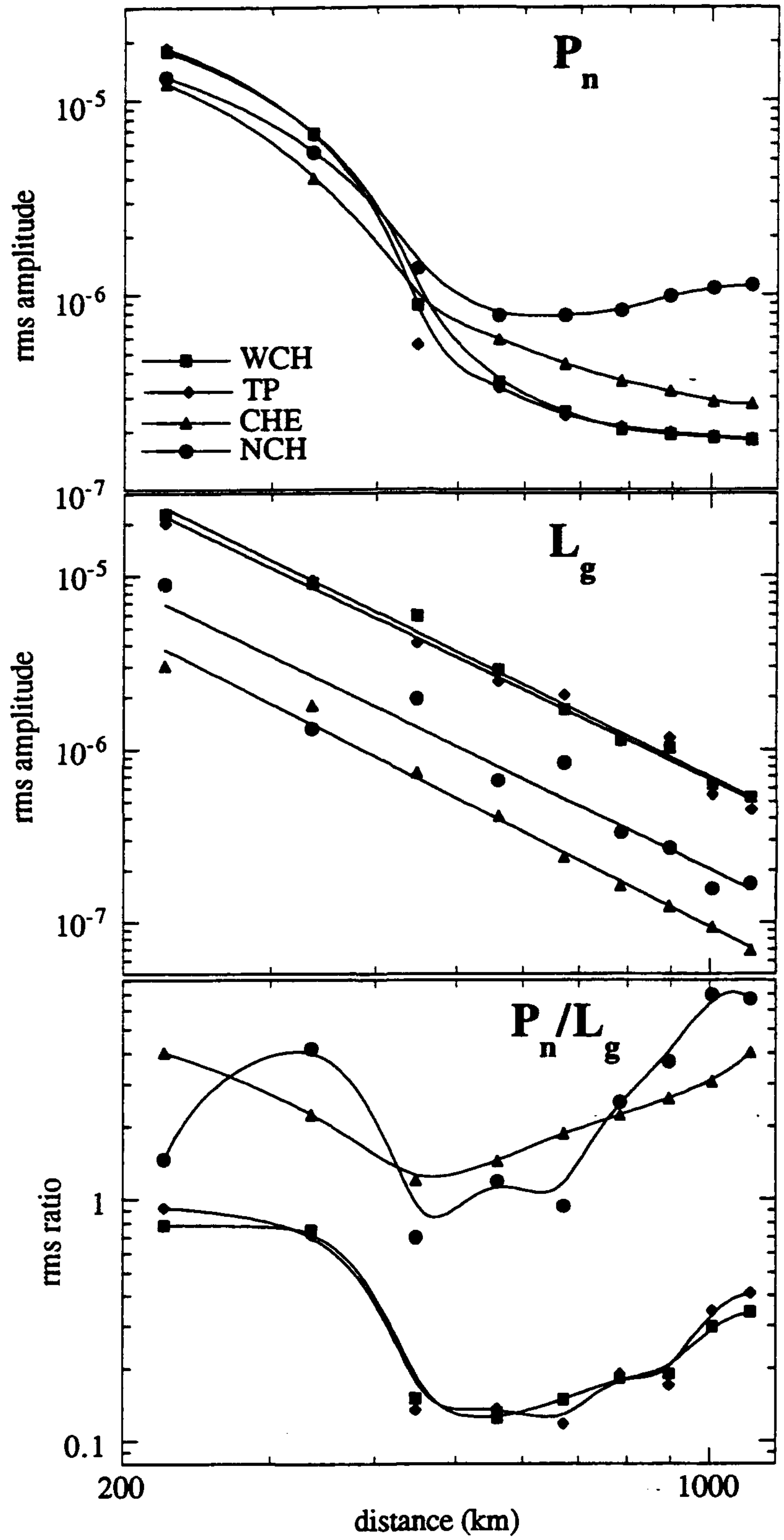

Figure 17. Short-period rms P_n and L_g amplitudes and their ratios versus distance for 4 different P wave velocity models and the explosive source. The velocity models can be identified in Figure 12; the synthetic waveforms for model WCH are shown in Figure 16.

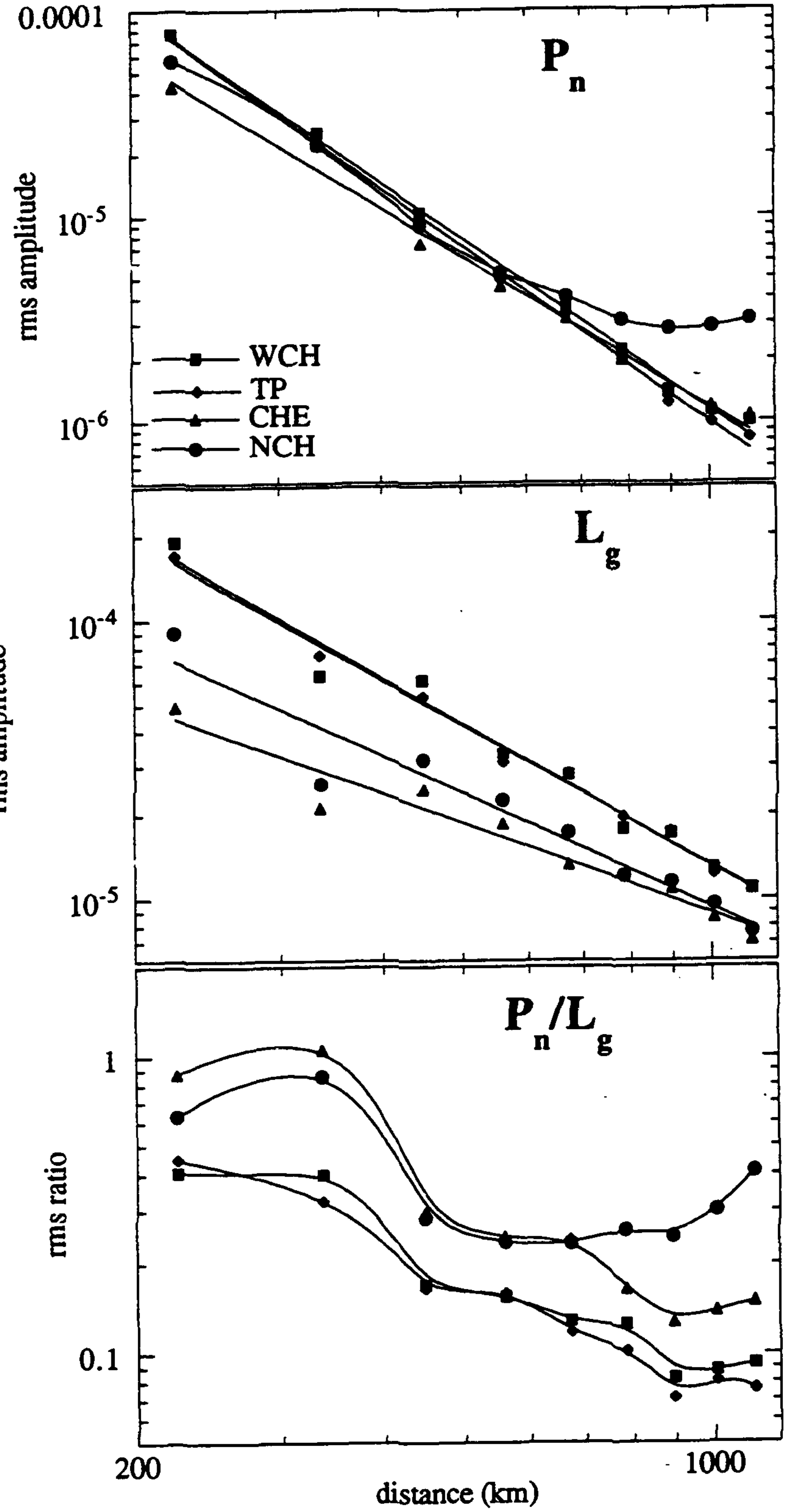

Figure 18. Broadband rms P_n and L_g amplitudes and their ratios versus distance for the same velocity models as Figure 17 and the explosive source. The synthetic waveforms for model WCH are shown in Figure 14.

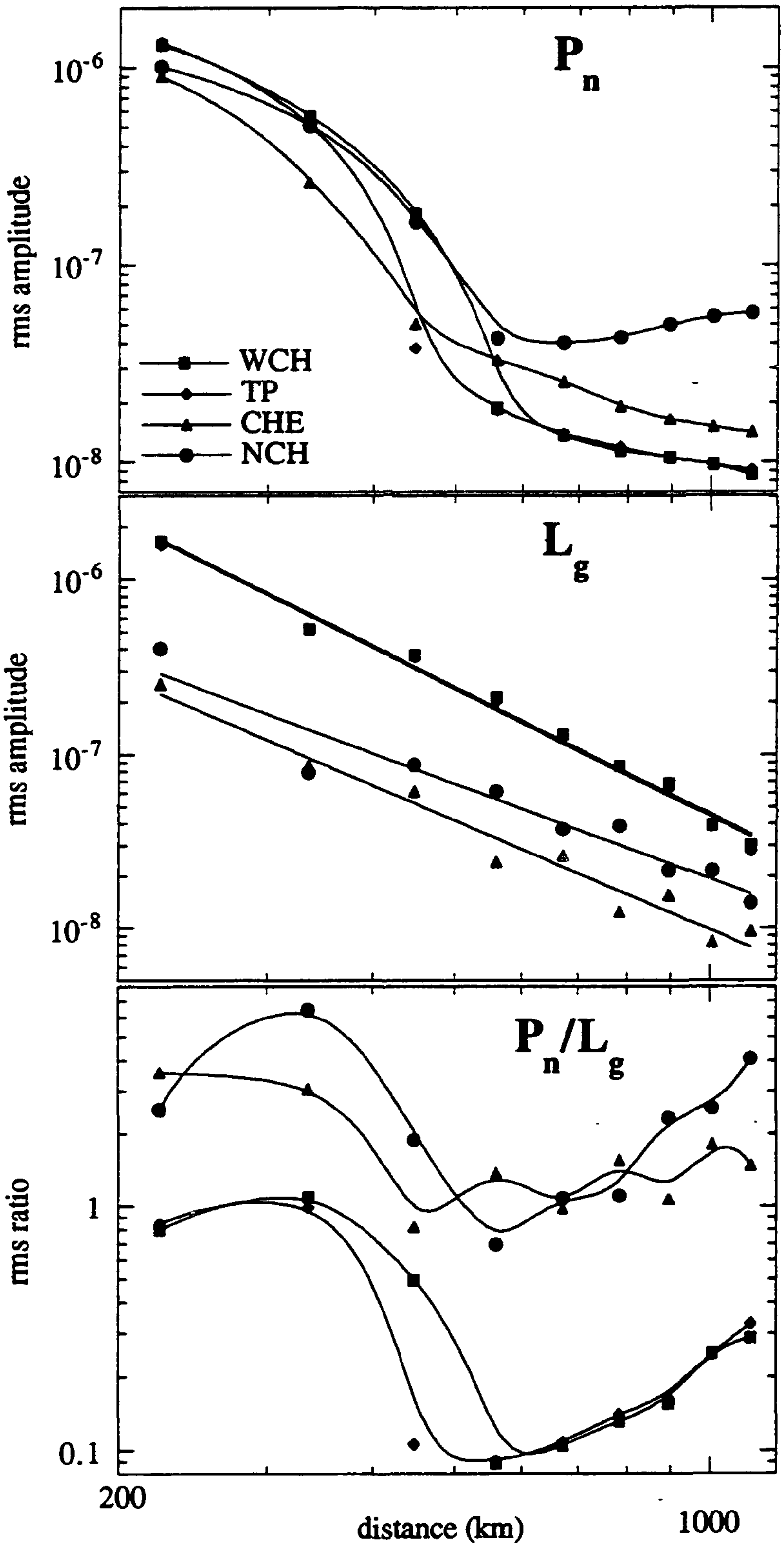

Figure 19. Same as Figure 17 but now for the earthquake source.

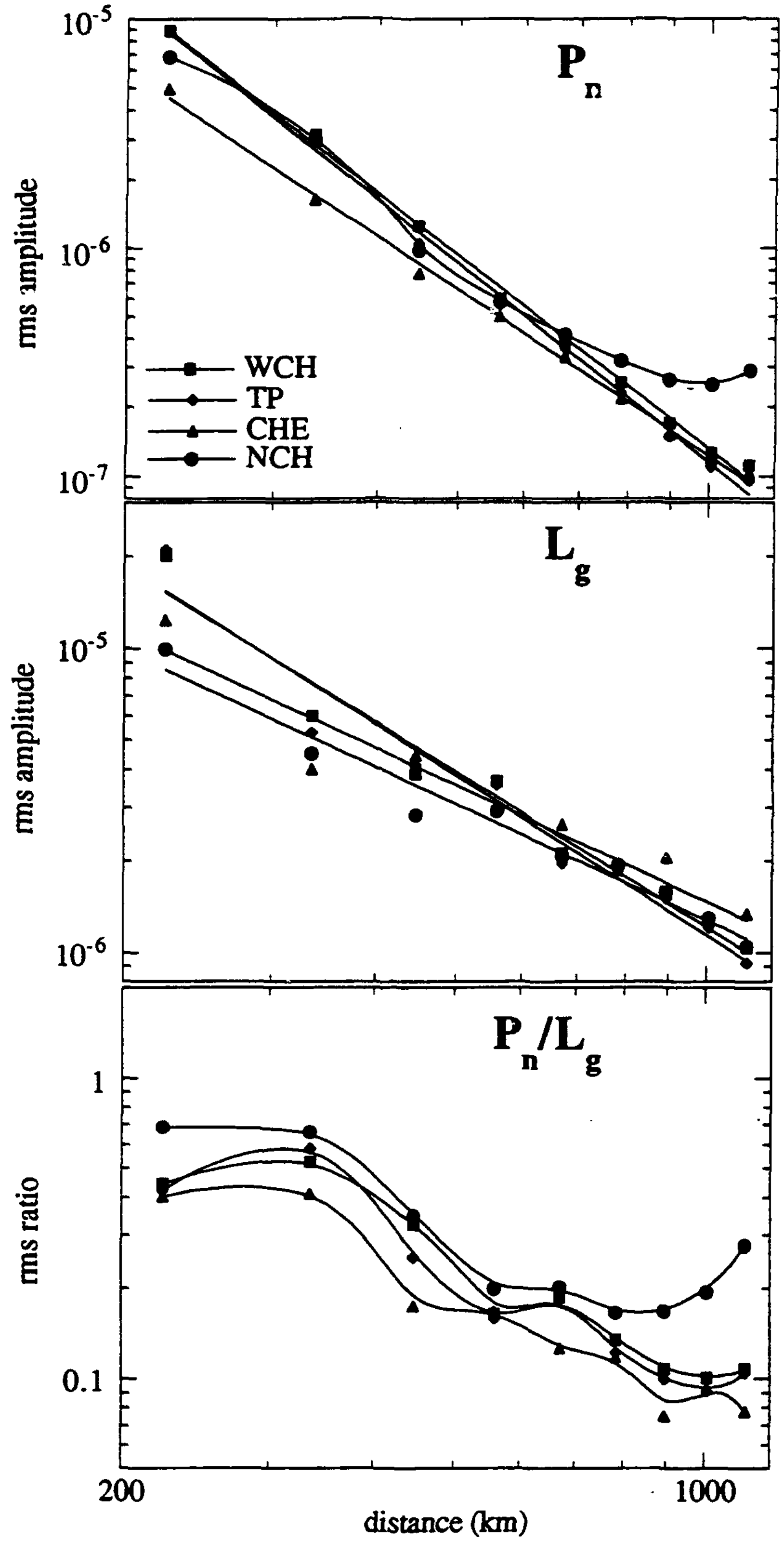

Figure 20. Same as Figure 18 but now for the earthquake source.

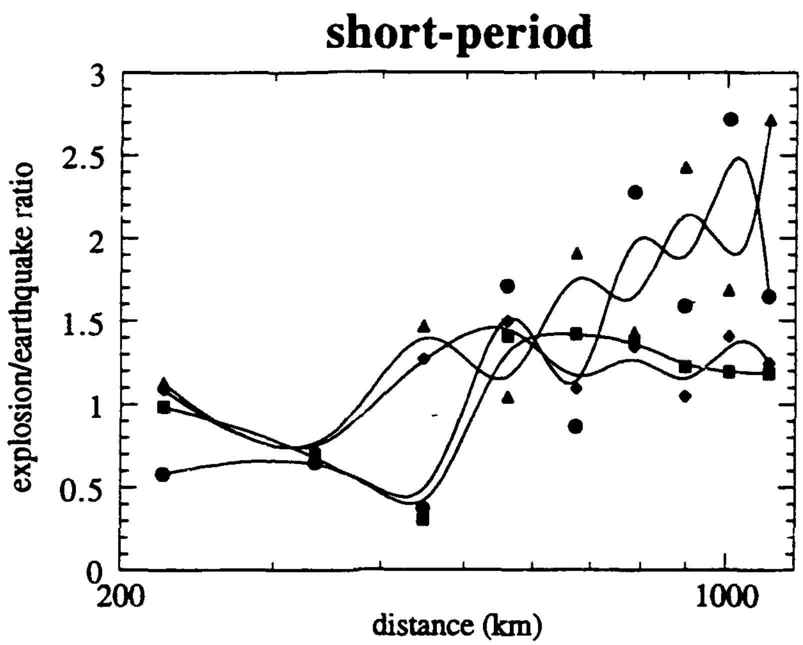

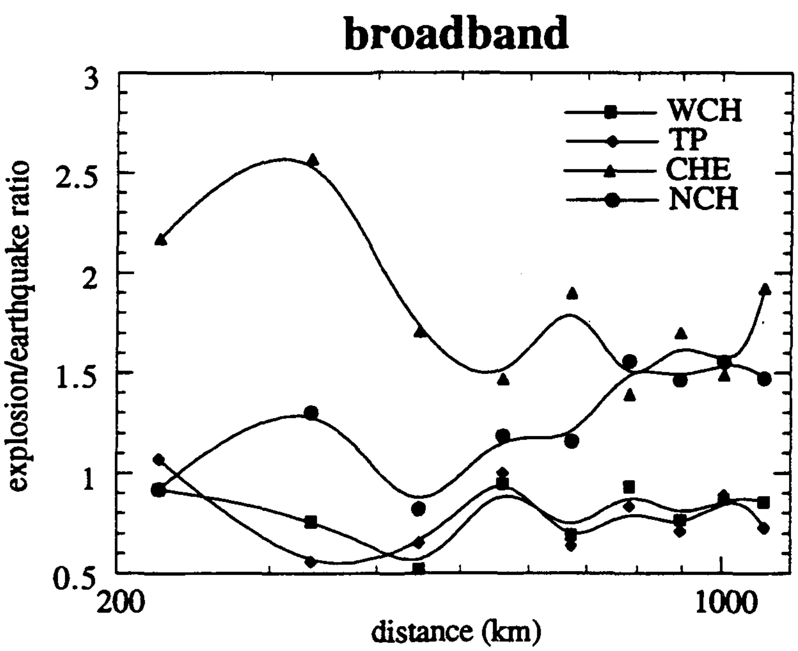

Figure 21. Quotient of explosion and earthquake P_n/L_g ratios. Though the short-period quotient is consistently higher than 1 for the regionalized Chinese velocity models it is considerably smaller than P_n/L_g variations due to propagation differences as can be inferred from Figures 17-20. Depending on the velocity structure, the broadband quotient can be both higher and lower than 1.

Appendix A

Overview of long-period modeling results. Data are shown in top trace and are underlain by synthetics for models S25, K8, WCH and T7. The synthetic for the preferred model is shown solid, other synthetics are dashed. Data and synthetic are aligned on their first motions and are normalized relative to their peak amplitude. Event numbers and stations correspond to those in Figure 2 and Table 1.

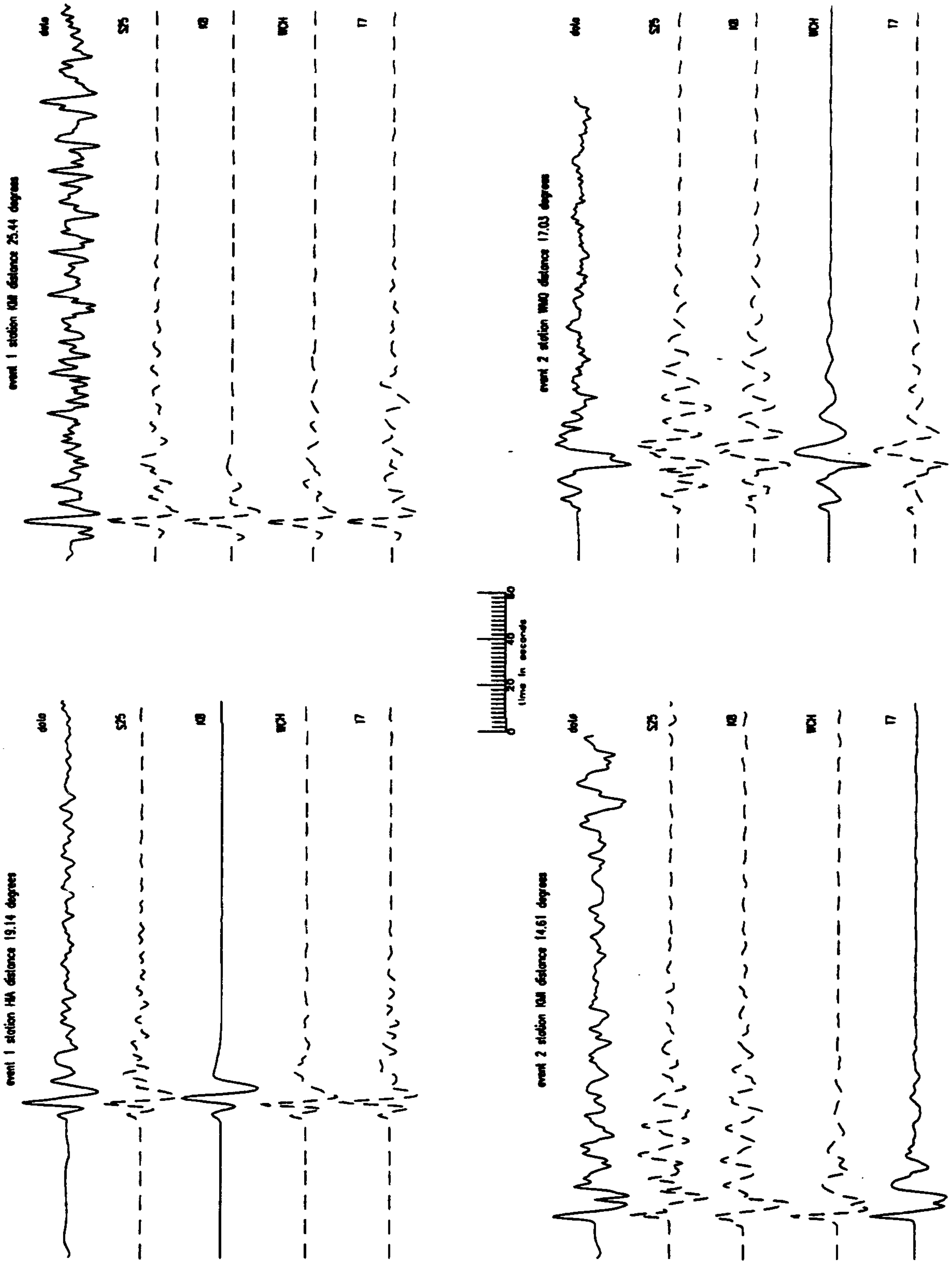
event 1 station KMI distance 25.44 degrees
event 1 station HIA distance 19.14 degrees
event 2 station WMQ distance 17.03 degrees
event 2 station KMI distance 14.61 degrees
data
S25
WCH
0
20
40
60
time in seconds

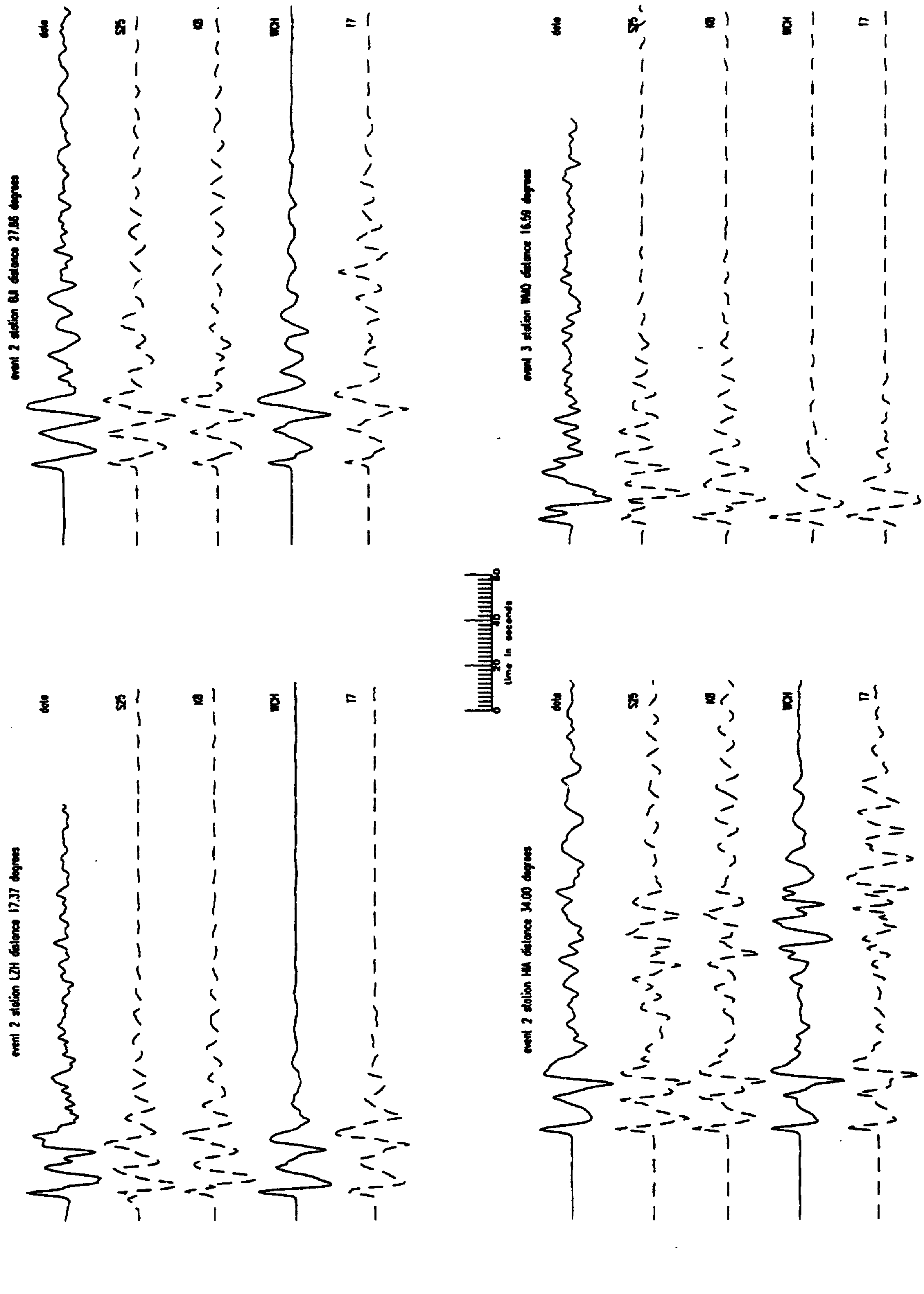
event 2 station BJI distance 27.86 degrees
data
S25
K8
WCH
T7
event 3 station WMQ distance 16.59 degrees
data
S25
K8
WCH
T7
0
20
40
60
time in seconds
event 2 station LZH distance 17.37 degrees
data
S25
K8
WCH
T7
event 2 station HIA distance 34.00 degrees
data
S25
K8
WCH
T7

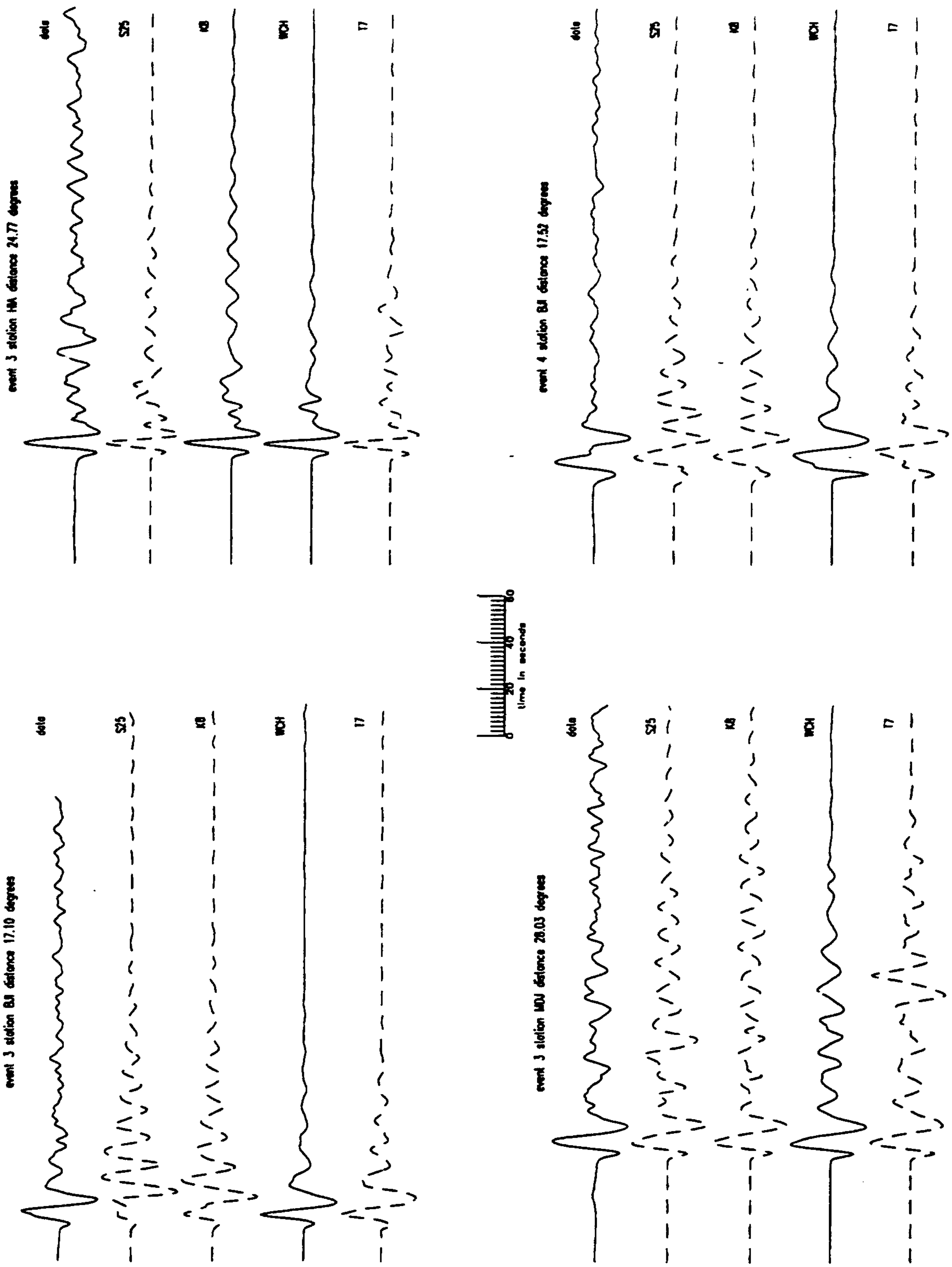

event 3 station HIA distance 24.77 degrees
data
S25
K8
WCH
T7
event 4 station BJI distance 17.52 degrees
data
S25
K8
WCH
T7
event 3 station BJI distance 17.10 degrees
data
S25
K8
WCH
T7
event 3 station MDJ distance 28.03 degrees
data
S25
K8
WCH
T7
0
20
40
60
time in seconds

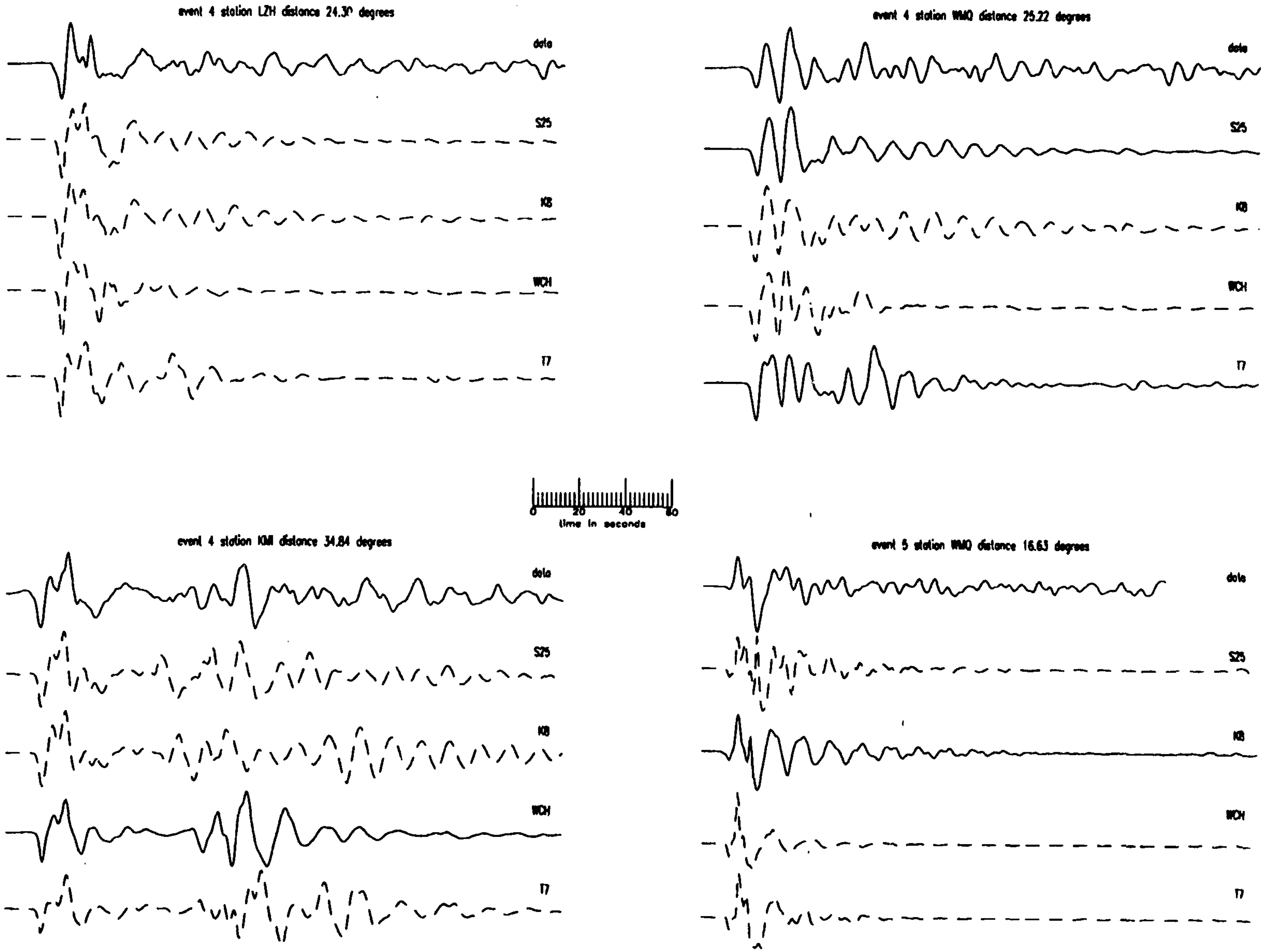
event 4 station LZH distance 24.30 degrees
data
S25
KB
WCH
T7
event 4 station WMQ distance 25.22 degrees
data
S25
KB
WCH
T7
0
20
40
60
time in seconds
event 4 station KMI distance 34.84 degrees
data
S25
KB
WCH
T7
event 5 station WMQ distance 16.63 degrees
data
S25
KB
WCH
T7

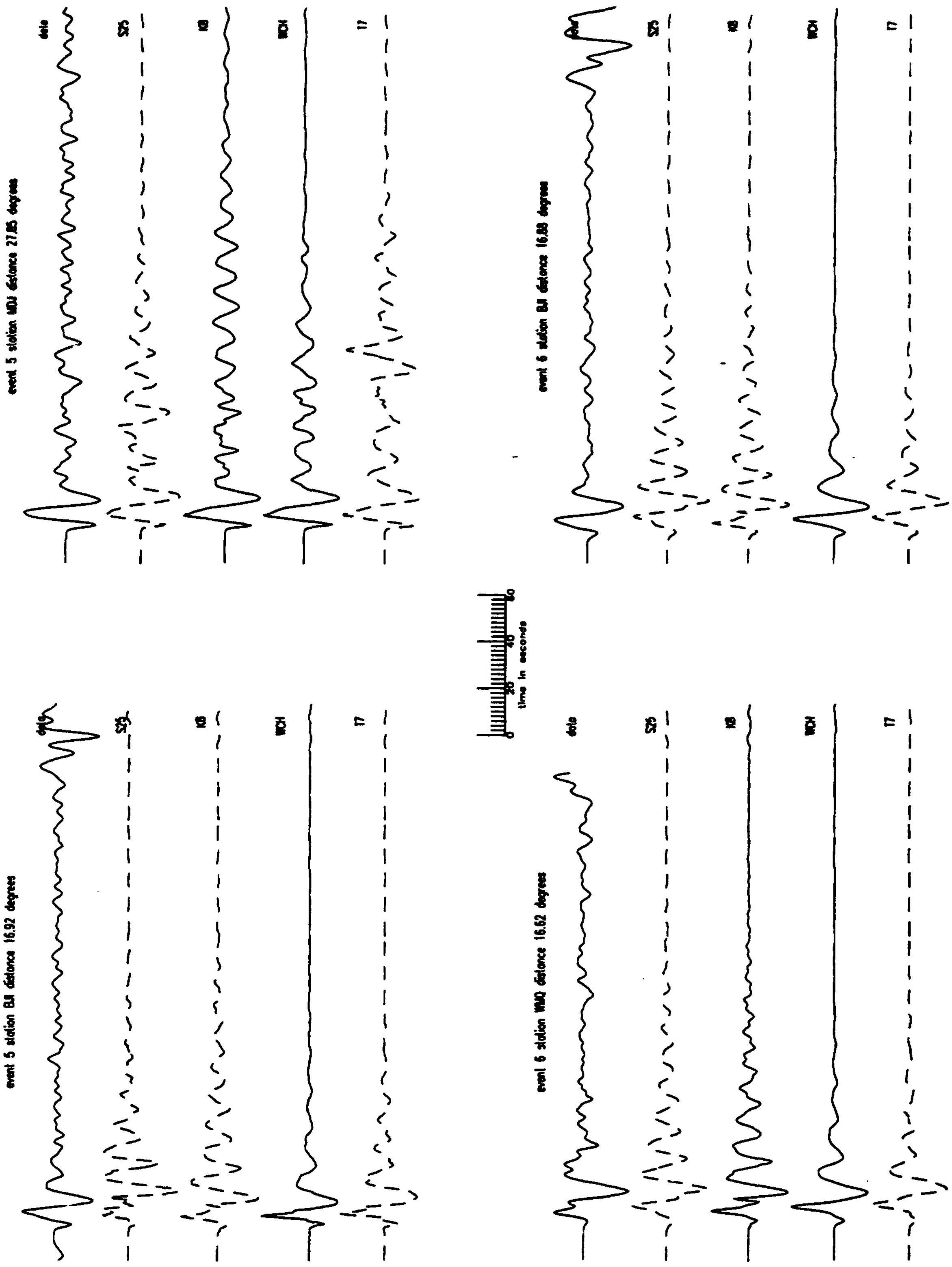
event 5 station MDJ distance 27.85 degrees
event 5 station BJI distance 16.92 degrees
event 6 station BJI distance 16.88 degrees
event 6 station WMQ distance 16.52 degrees
data
S25
K8
WCH
T7
0
20
40
60
time in seconds

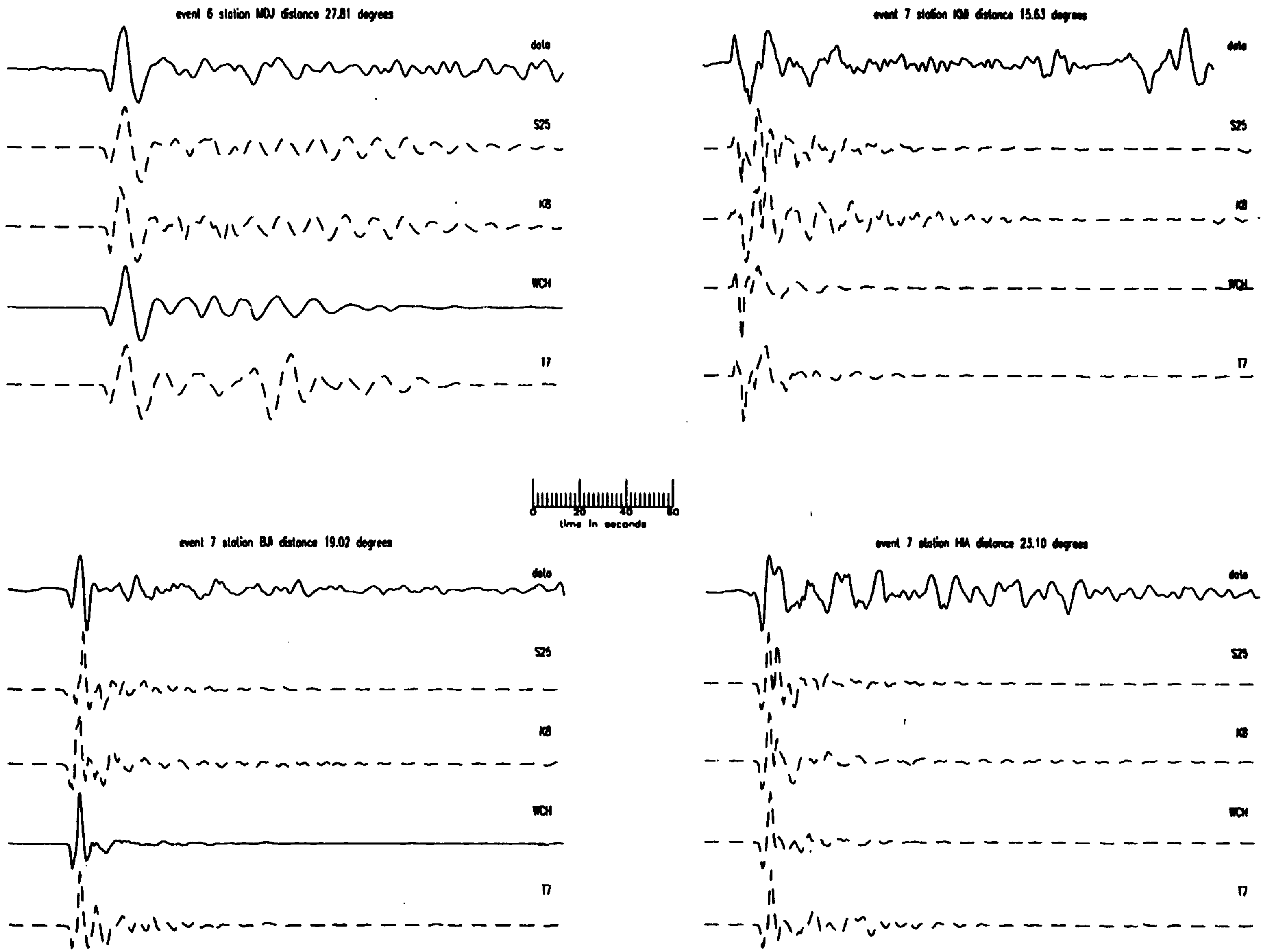
event 6 station MDJ distance 27.81 degrees
event 7 station KMI distance 15.63 degrees
event 7 station BJI distance 19.02 degrees
event 7 station HIA distance 23.10 degrees
data
S25
KB
WCH
T7
0
20
40
60
time in seconds

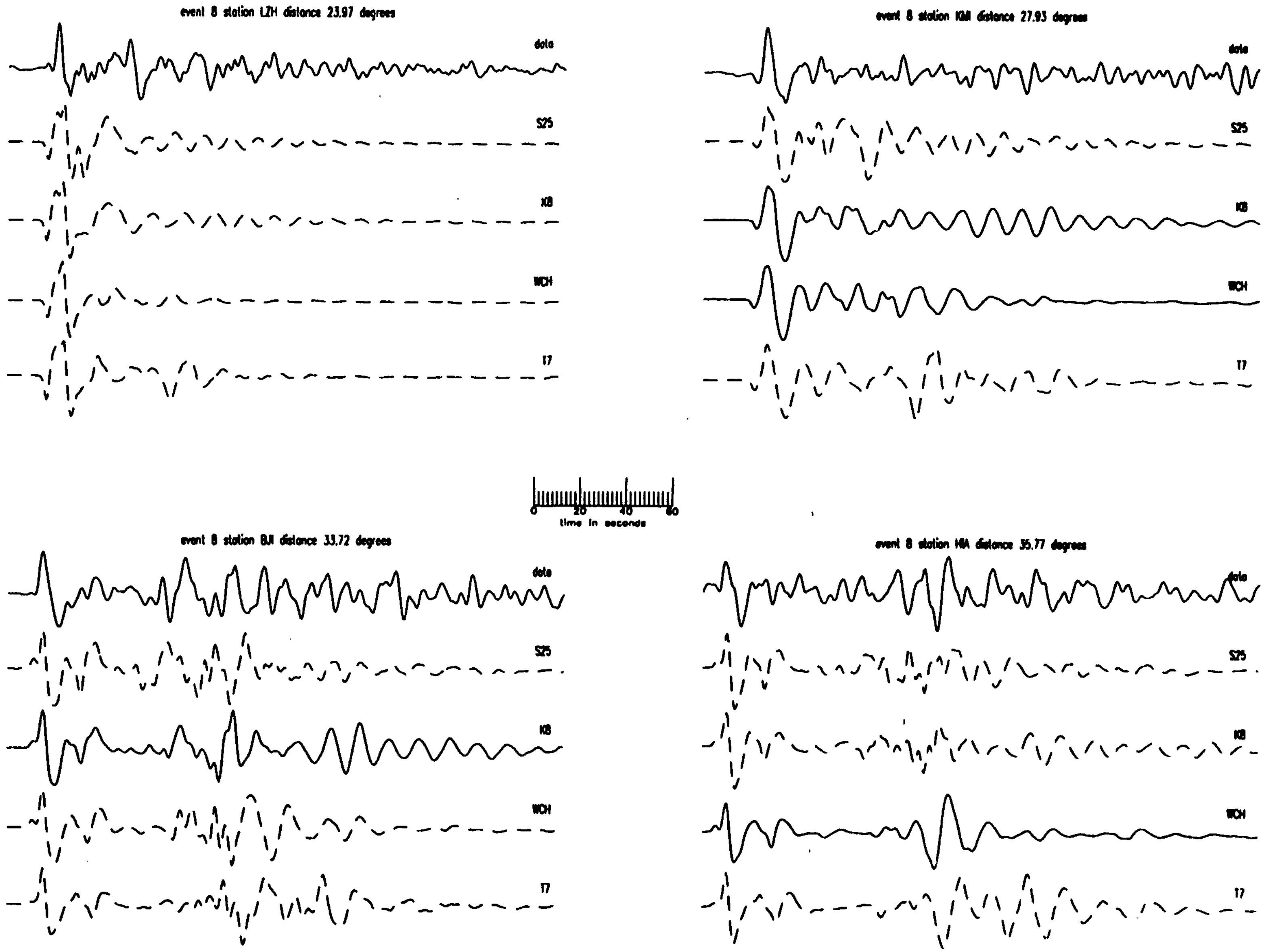
event 8 station LZH distance 23.97 degrees
data
S25
KB
WCH
T7
event 8 station KMI distance 27.93 degrees
data
S25
KB
WCH
T7
0
20
40
60
time in seconds
event 8 station BJI distance 33.72 degrees
data
S25
KB
WCH
T7
event 8 station HIA distance 35.77 degrees
data
S25
KB
WCH
T7

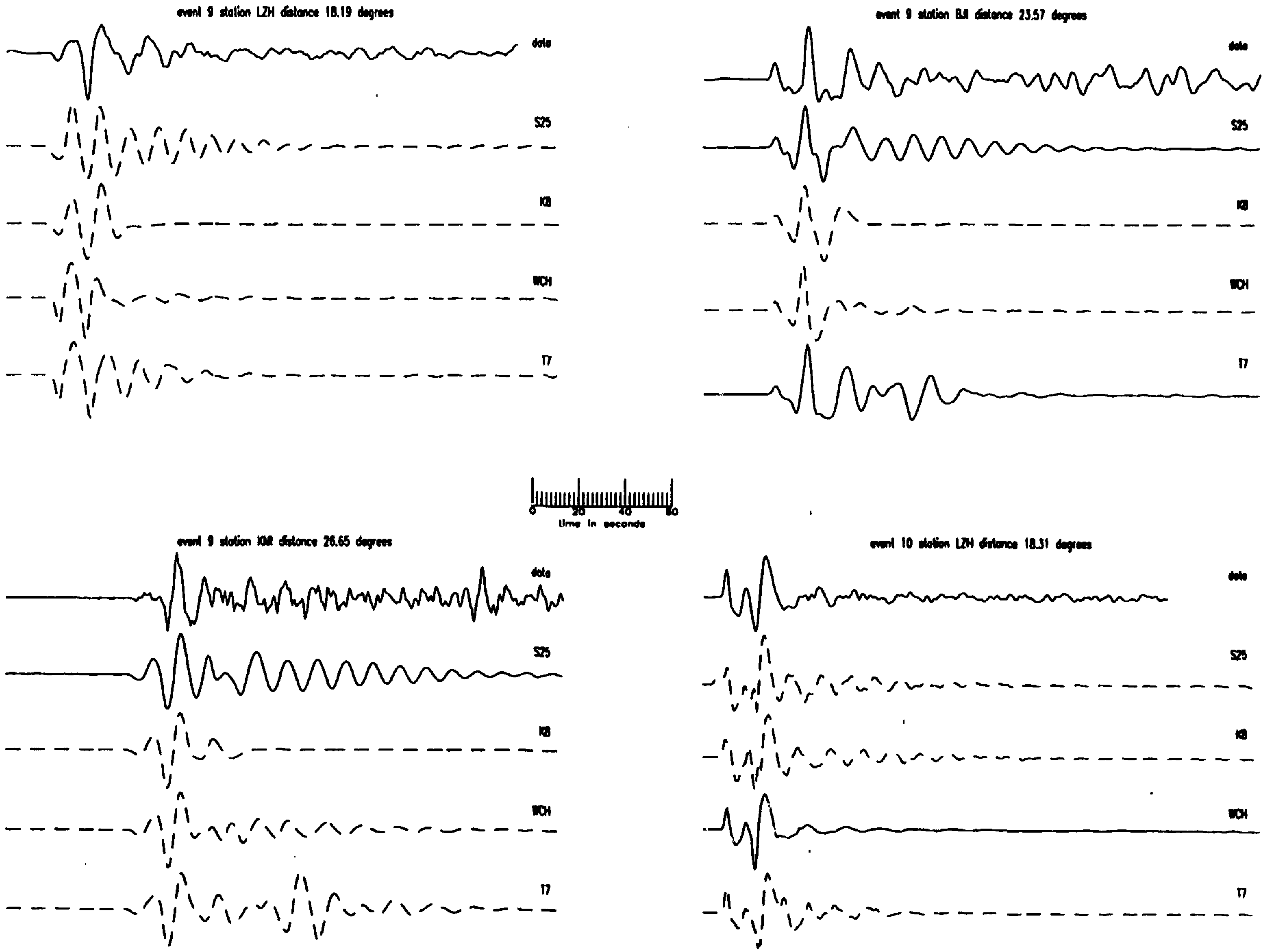

event 9 station LZH distance 18.19 degrees
data
S25
KB
WCH
T7
event 9 station BJI distance 23.57 degrees
data
S25
KB
WCH
T7
0
20
40
60
time in seconds
event 9 station KMI distance 26.65 degrees
data
S25
KB
WCH
T7
event 10 station LZH distance 18.31 degrees
data
S25
KB
WCH
T7

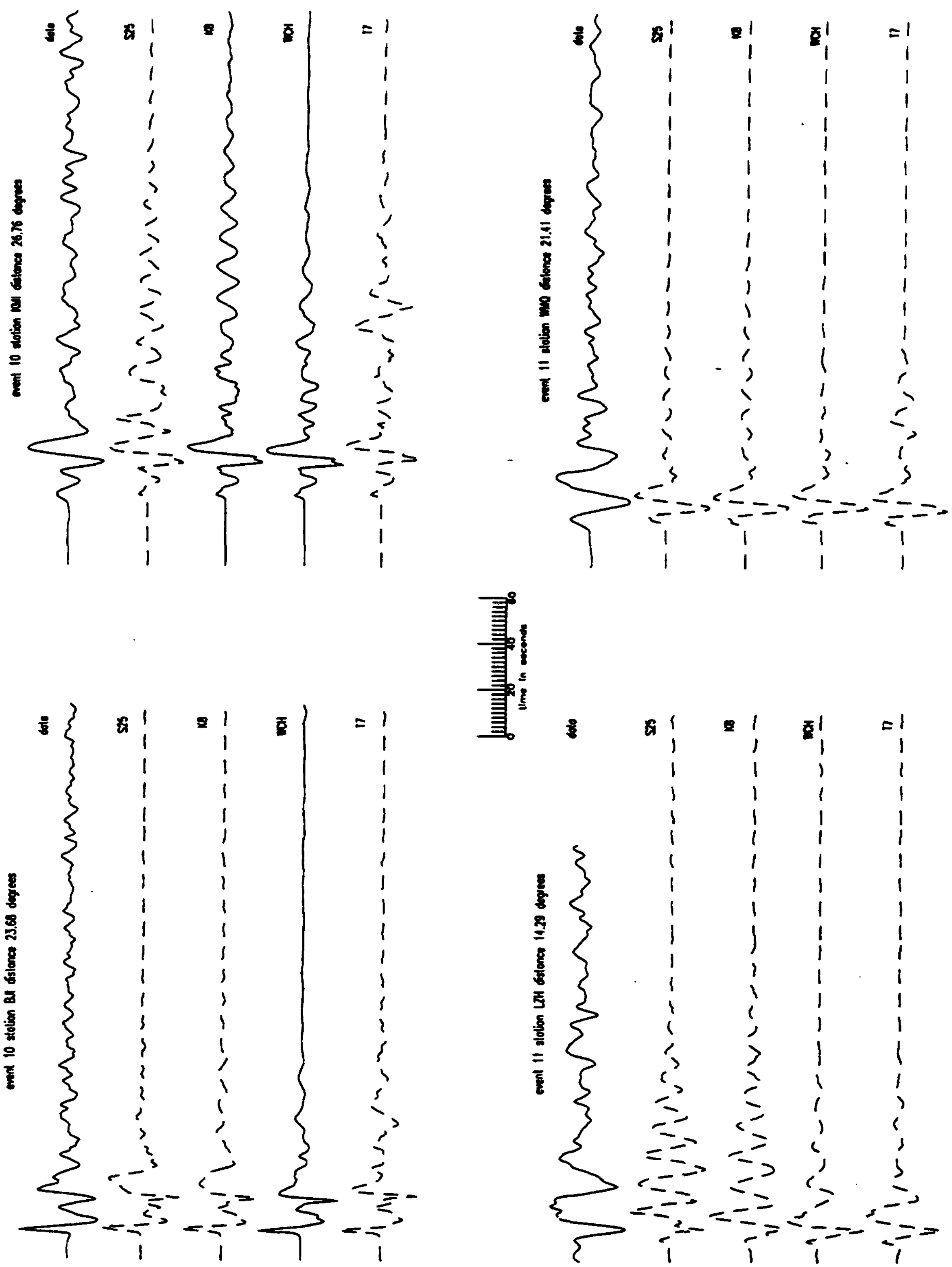

event 10 station BJI distance 23.68 degrees
event 10 station KMI distance 26.76 degrees
event 11 station LZH distance 14.29 degrees
event 11 station WMQ distance 21.41 degrees
data
S25
KB
WCH
T7
0
20
40
60
time in seconds

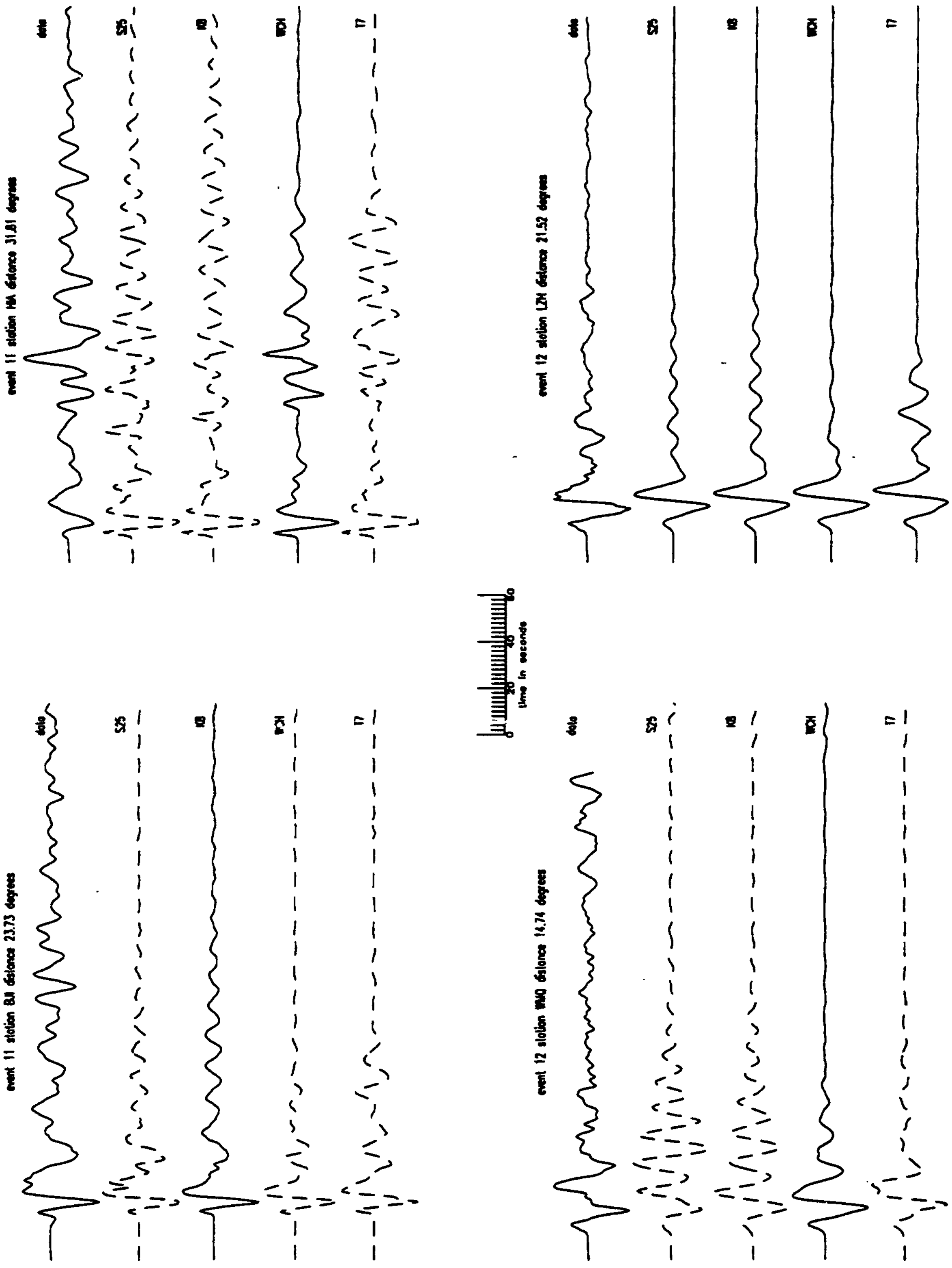
event 11 station HA distance 31.81 degrees
event 11 station BJI distance 23.73 degrees
event 12 station LZH distance 21.52 degrees
event 12 station WMQ distance 14.74 degrees
data
S25
KB
WCH
T7
0
20
40
60
time in seconds

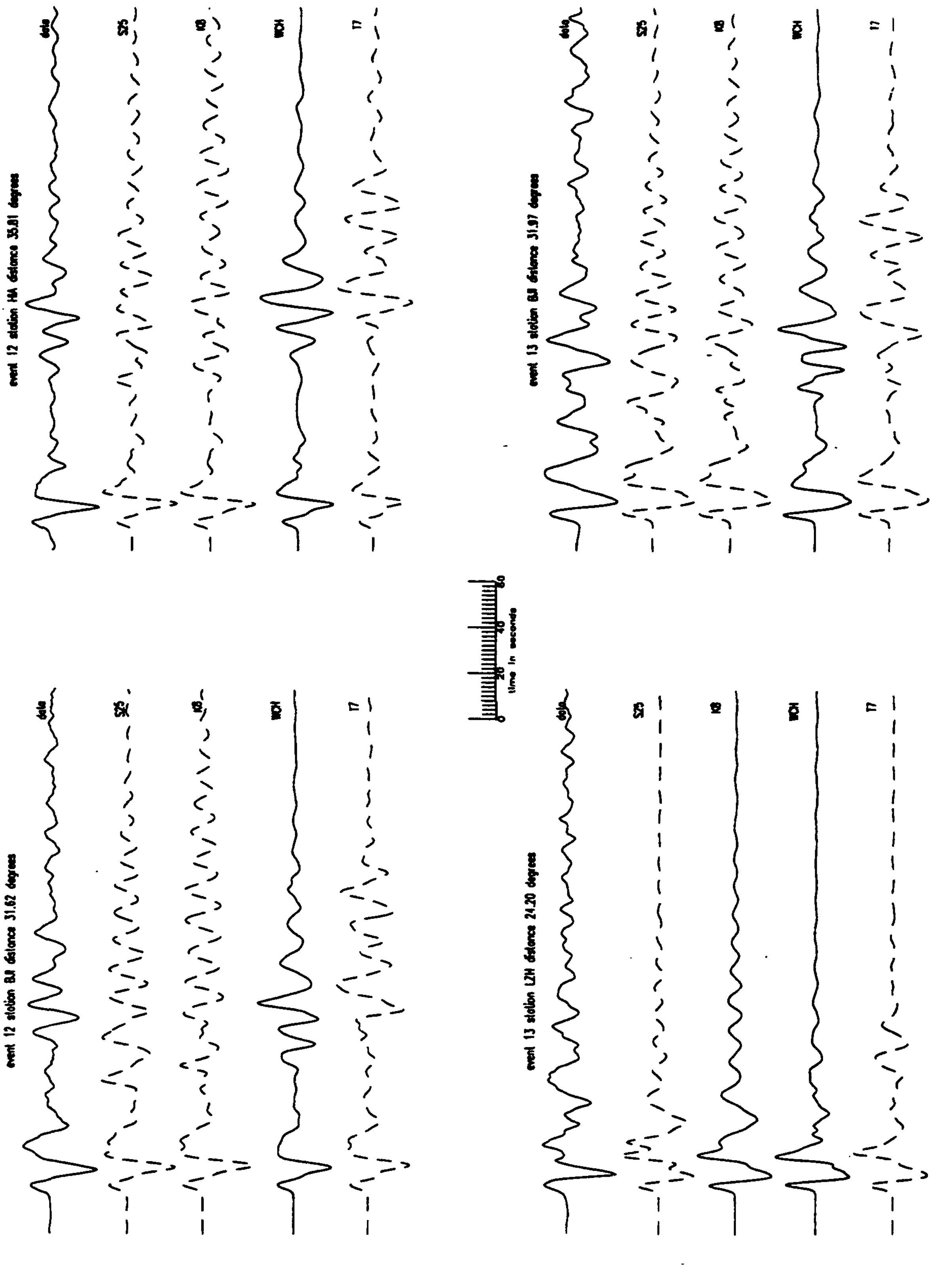

event 12 station BJI distance 31.62 degrees
event 12 station HIA distance 35.81 degrees
event 13 station LZH distance 24.20 degrees
event 13 station BJI distance 31.97 degrees
data
S25
KB
WCH
T7
0
20
40
60
time in seconds

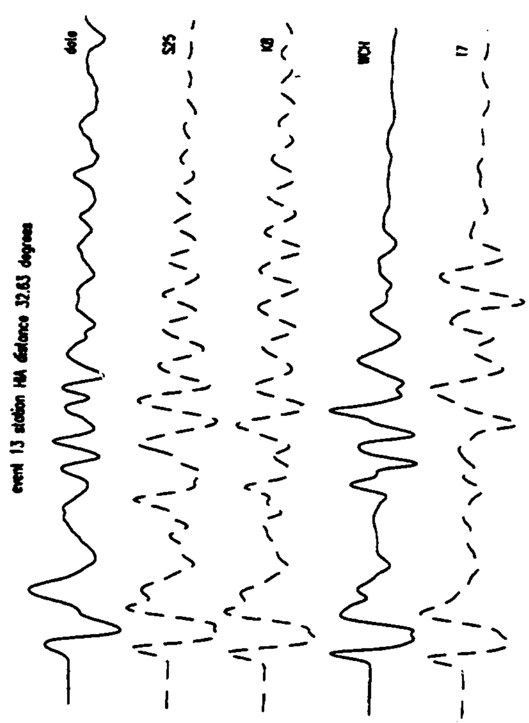
event 13 station HA distance 32.83 degrees
data
S25
KB
WCH

Appendix B

Overview of broadband modeling results. Top traces show match between the observed waveform and the synthetic generated for model WCH, the bottom trace gives the best match obtained for this waveform. The velocity profiles indicate changes made to model WCH to obtain this match. Event numbers and stations correspond to those in Figure 2 and Table 1.

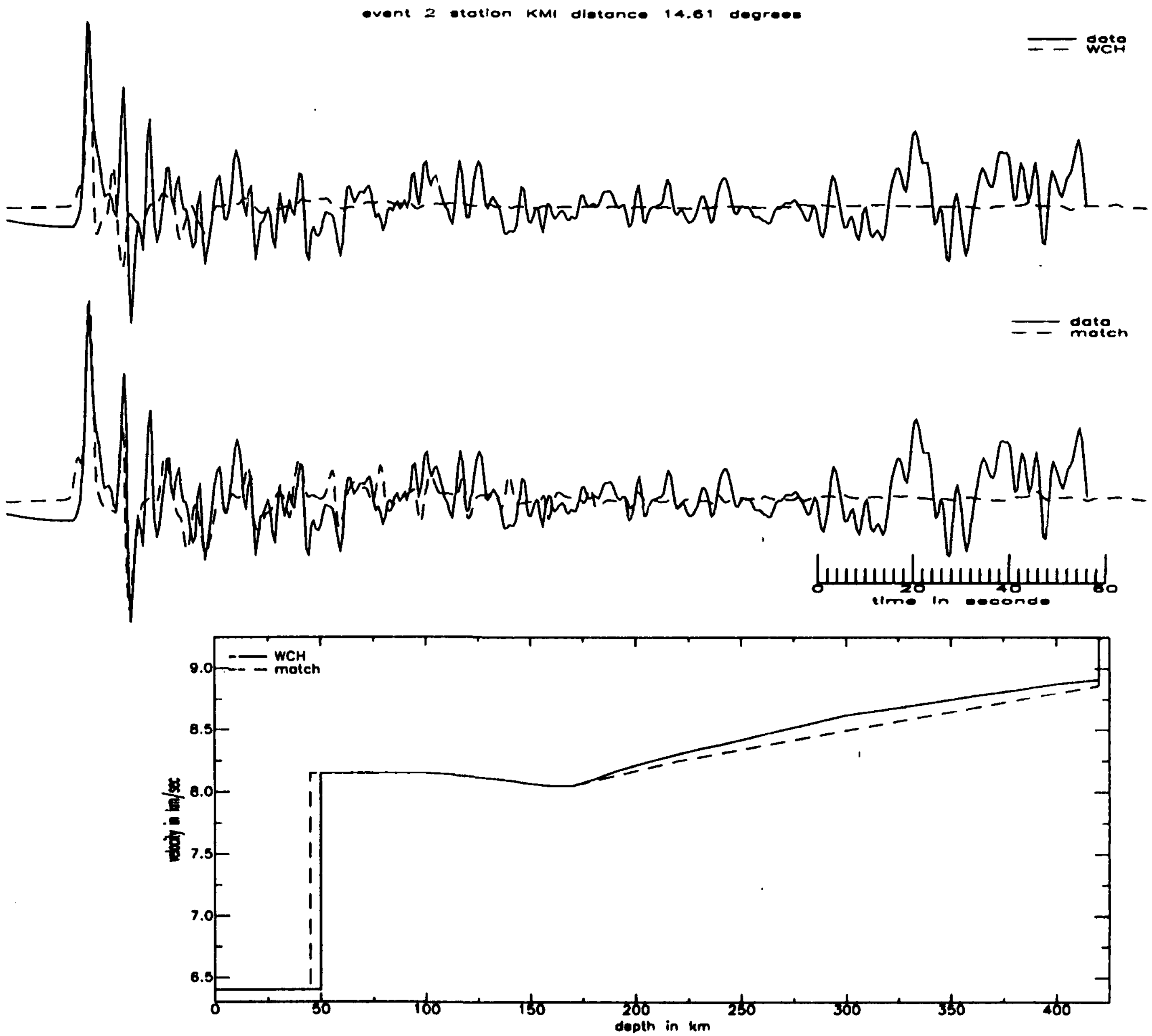

event 2 station KMI distance 14.61 degrees
data
WCH
data
match
0
20
40
60
time in seconds
WCH
match
9.0
8.5
8.0
7.5
7.0
6.5
velocity in km/sec
0
50
100
150
200
250
300
350
400
depth in km

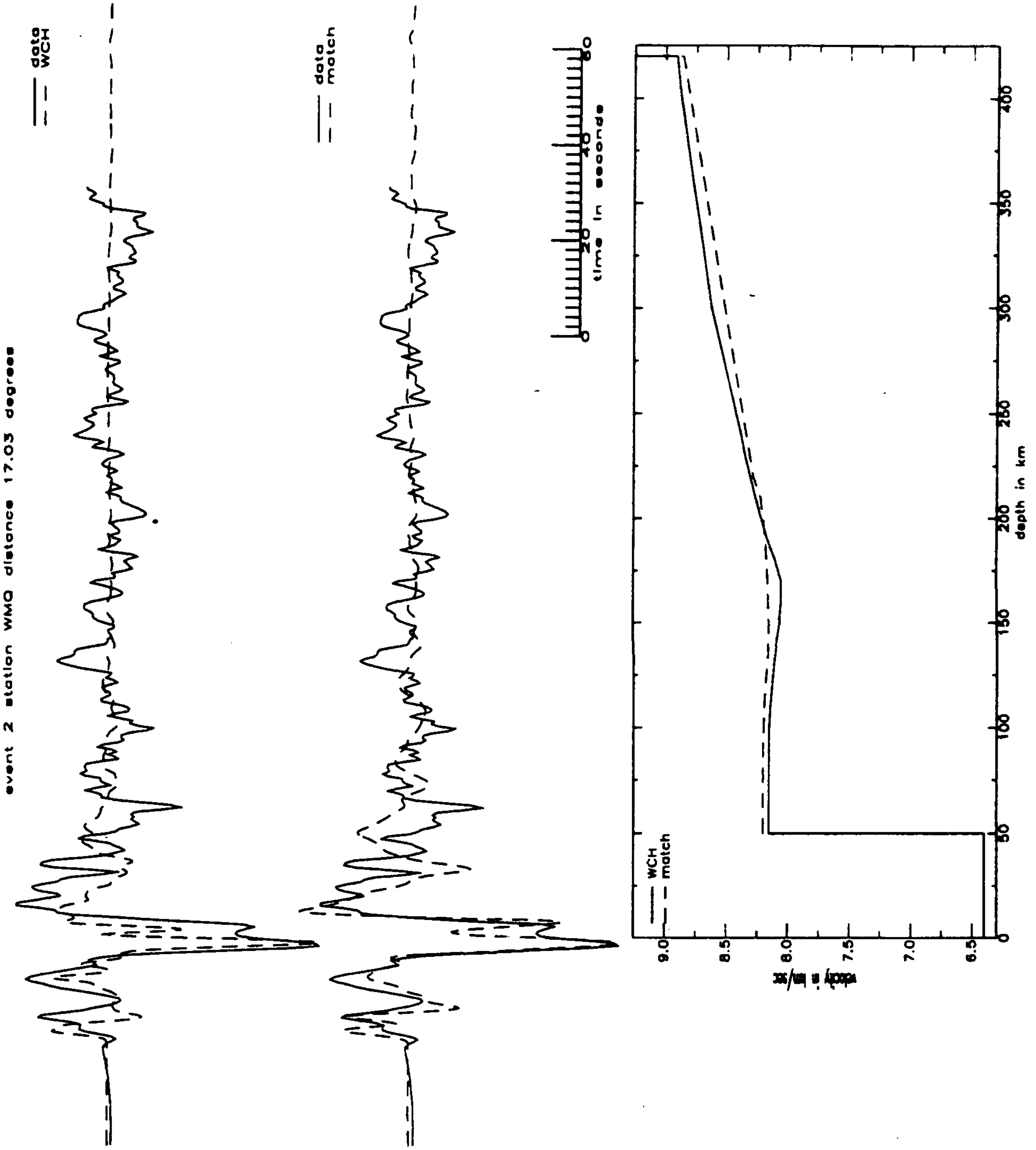

event 2 station WMQ distance 17.03 degrees
data
WCH
data
match
0
20
40
60
time in seconds
WCH
match
9.0
8.5
8.0
7.5
7.0
6.5
velocity in km/sec
0
50
100
150
200
250
300
350
400
depth in km

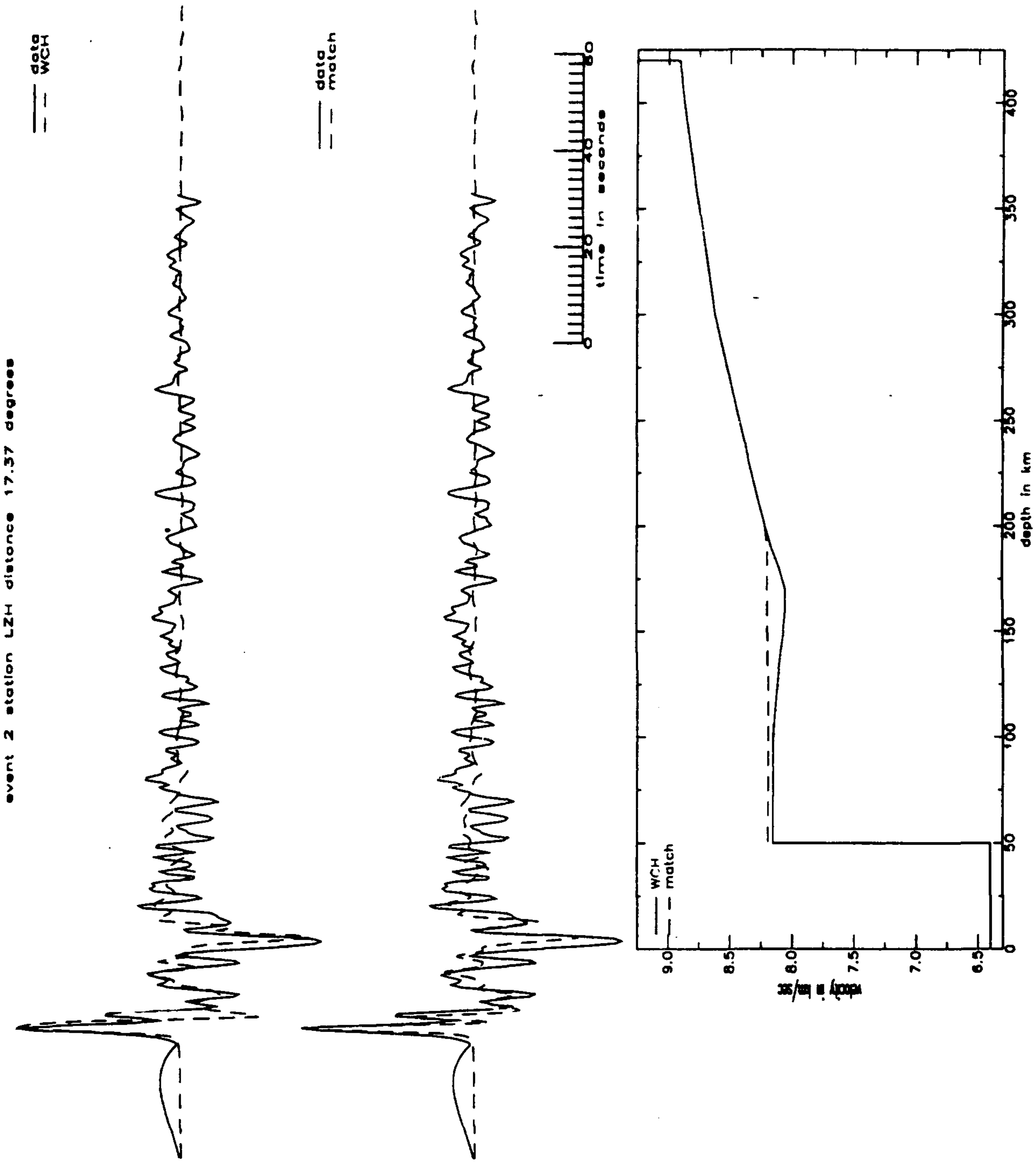

event 2 station LZH distance 17.37 degrees
data
WCH
data
match
0
20
40
60
time in seconds
WCH
match
velocity in km/sec
9.0
8.5
8.0
7.5
7.0
6.5
0
50
100
150
200
250
300
350
400
depth in km

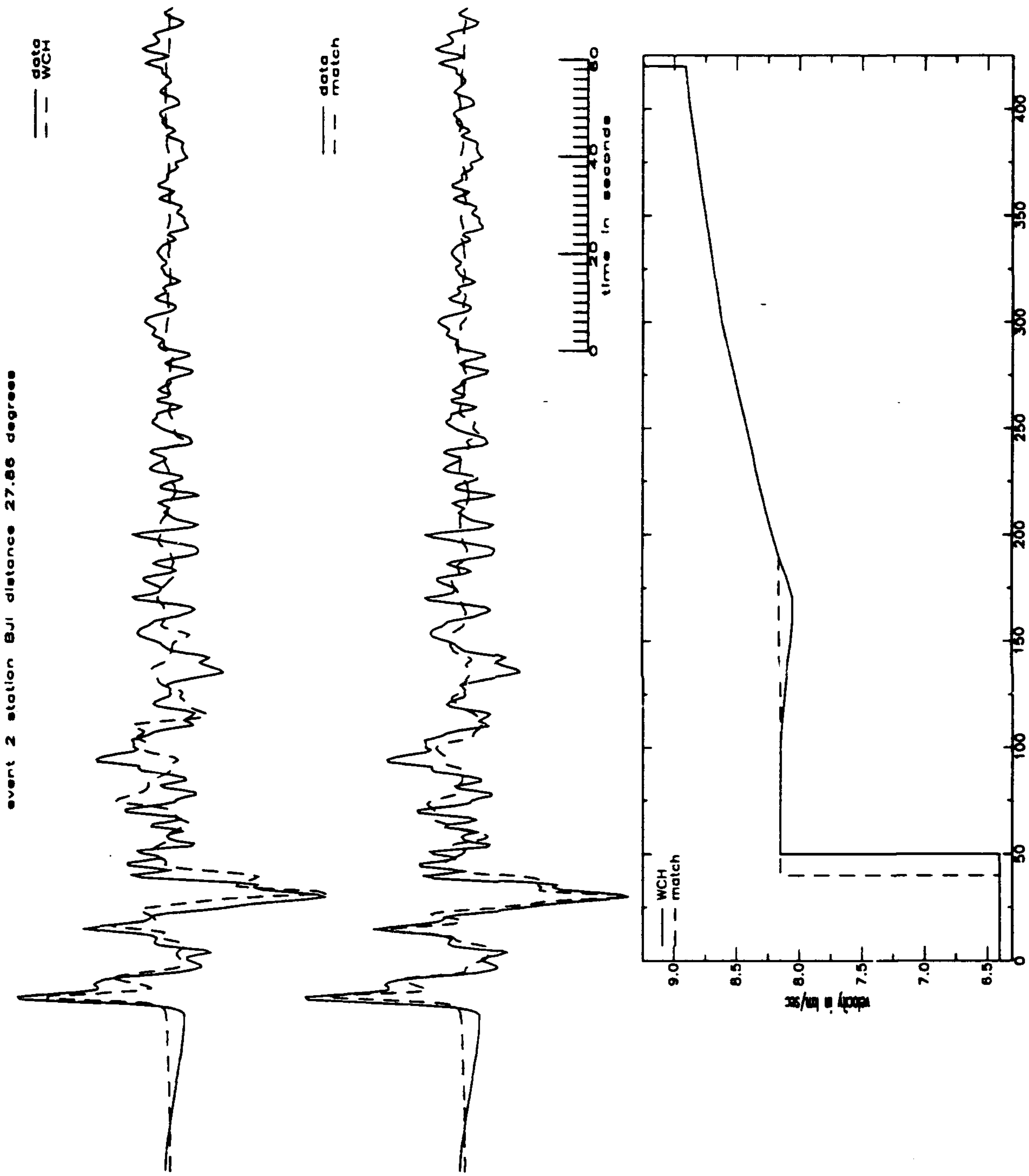

event 2 station BJI distance 27.86 degrees
data
WCH
data
match
0 20 40 60
time in seconds
WCH
match
9.0 8.5 8.0 7.5 7.0 6.5
velocity in km/sec
0 50 100 150 200 250 300 350 400
depth in km

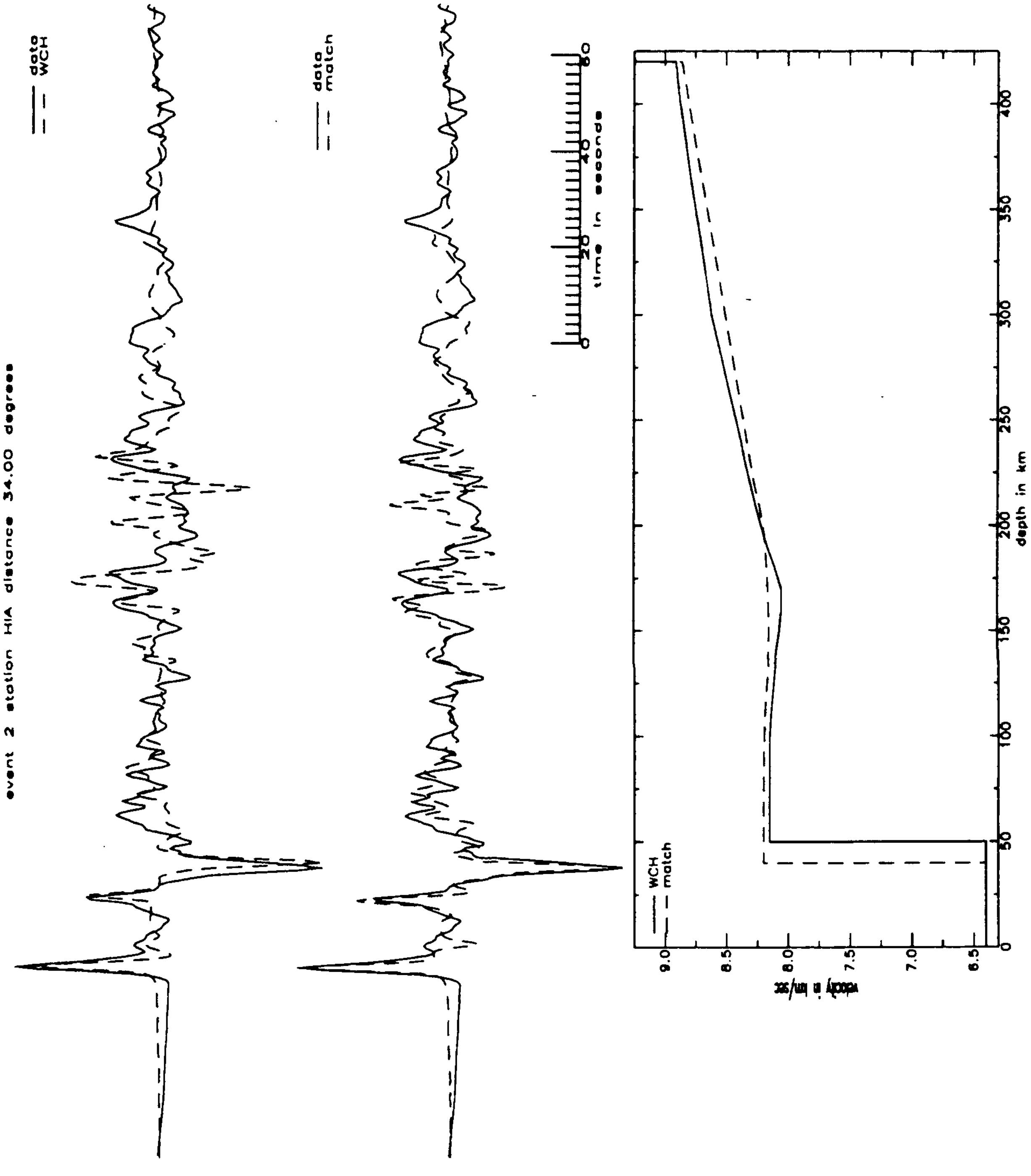
event 2 station HIA distance 34.00 degrees
data
WCH
data
match
0
20
40
60
time in seconds
WCH
match
9.0
8.5
8.0
7.5
7.0
6.5
velocity in km/sec
0
50
100
150
200
250
300
350
400
depth in km

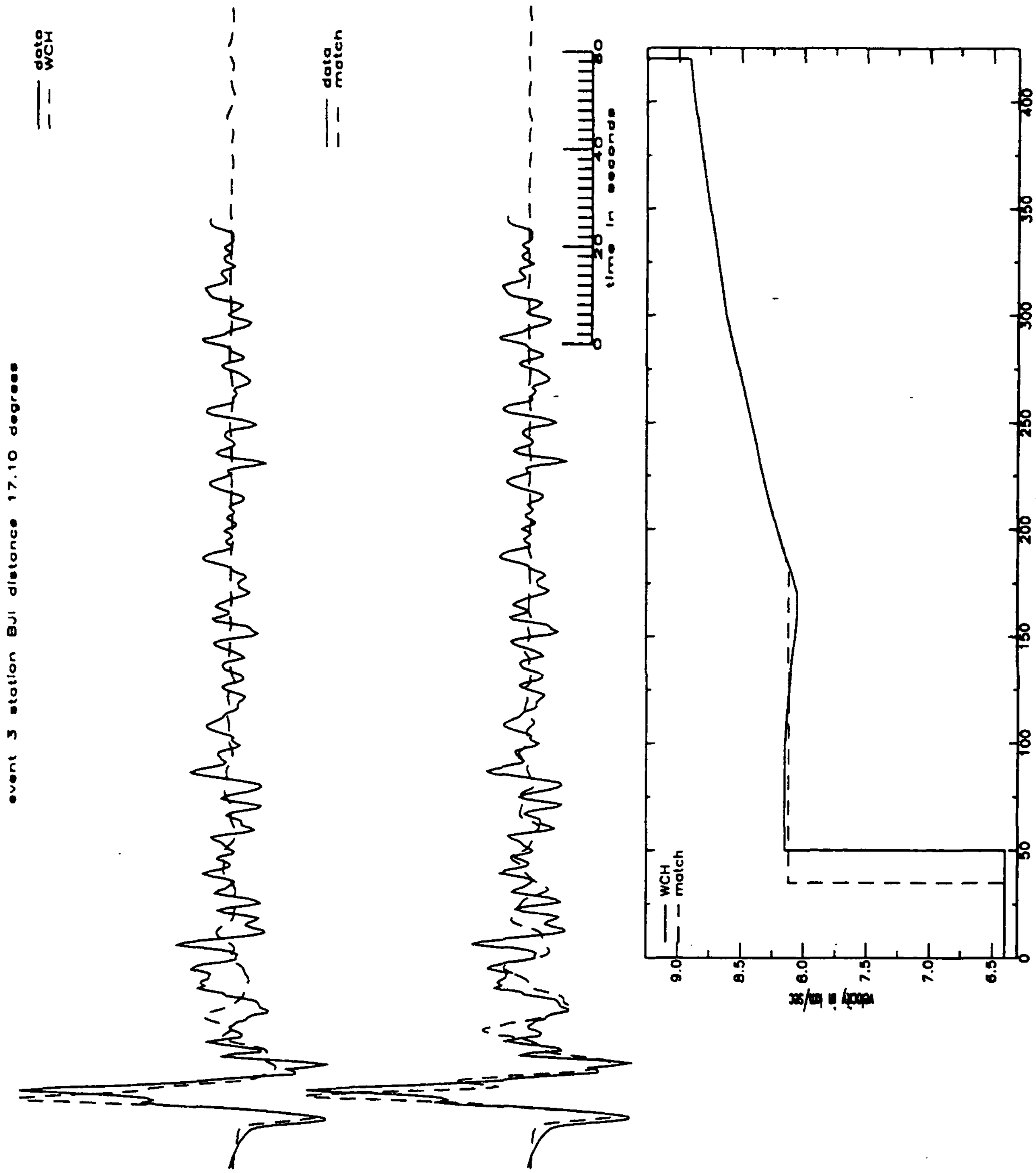
event 3 station BJI distance 17.10 degrees
data
WCH
data
match
0 20 40 60
time in seconds
WCH
match
depth in km
velocity in km/sec

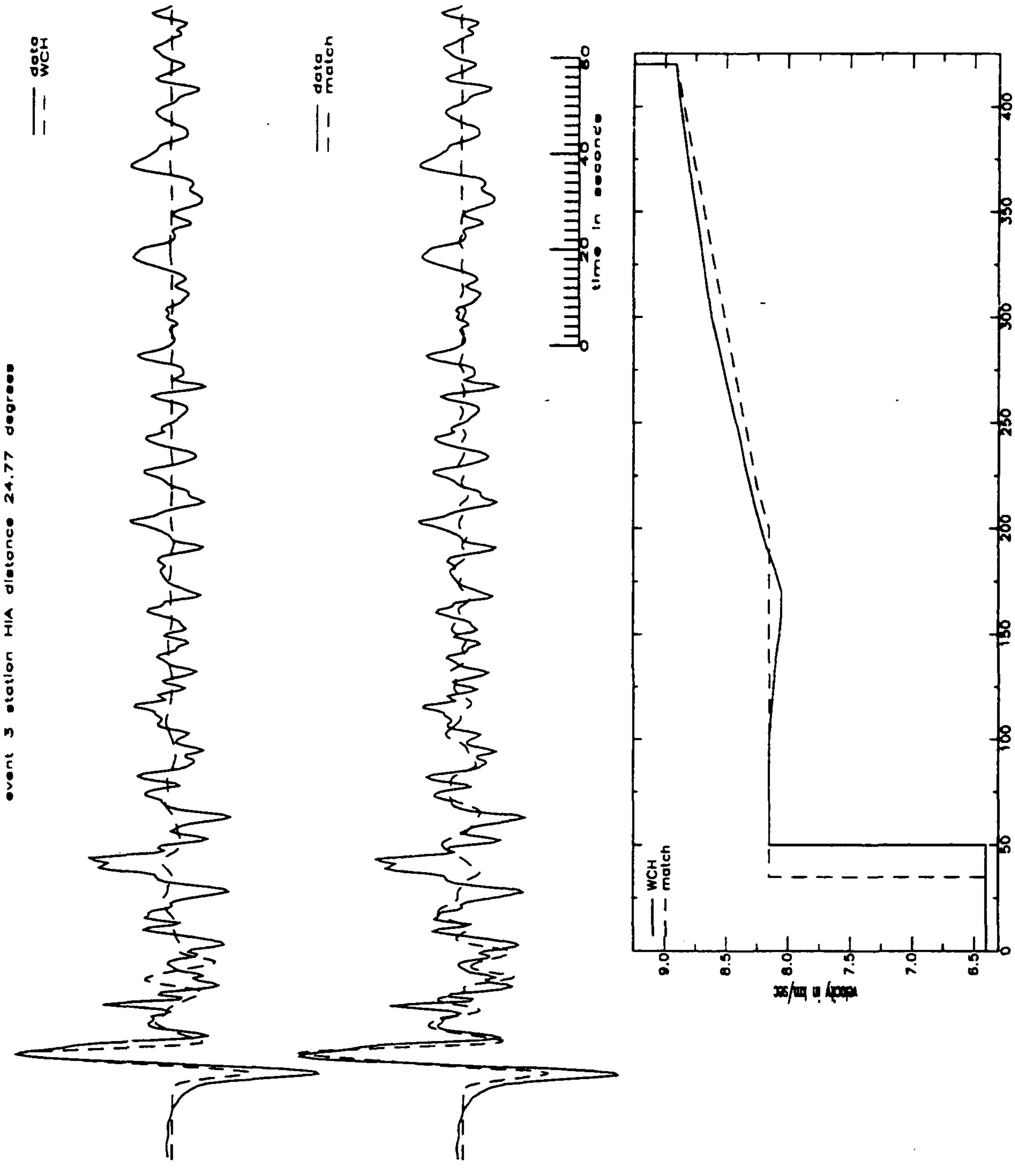
event 3 station HIA distance 24.77 degrees
data
WCH
data
match
0
20
40
60
time in seconds
WCH
match
9.0
8.5
8.0
7.5
7.0
6.5
velocity in km/sec
0
50
100
150
200
250
300
350
400
depth in km

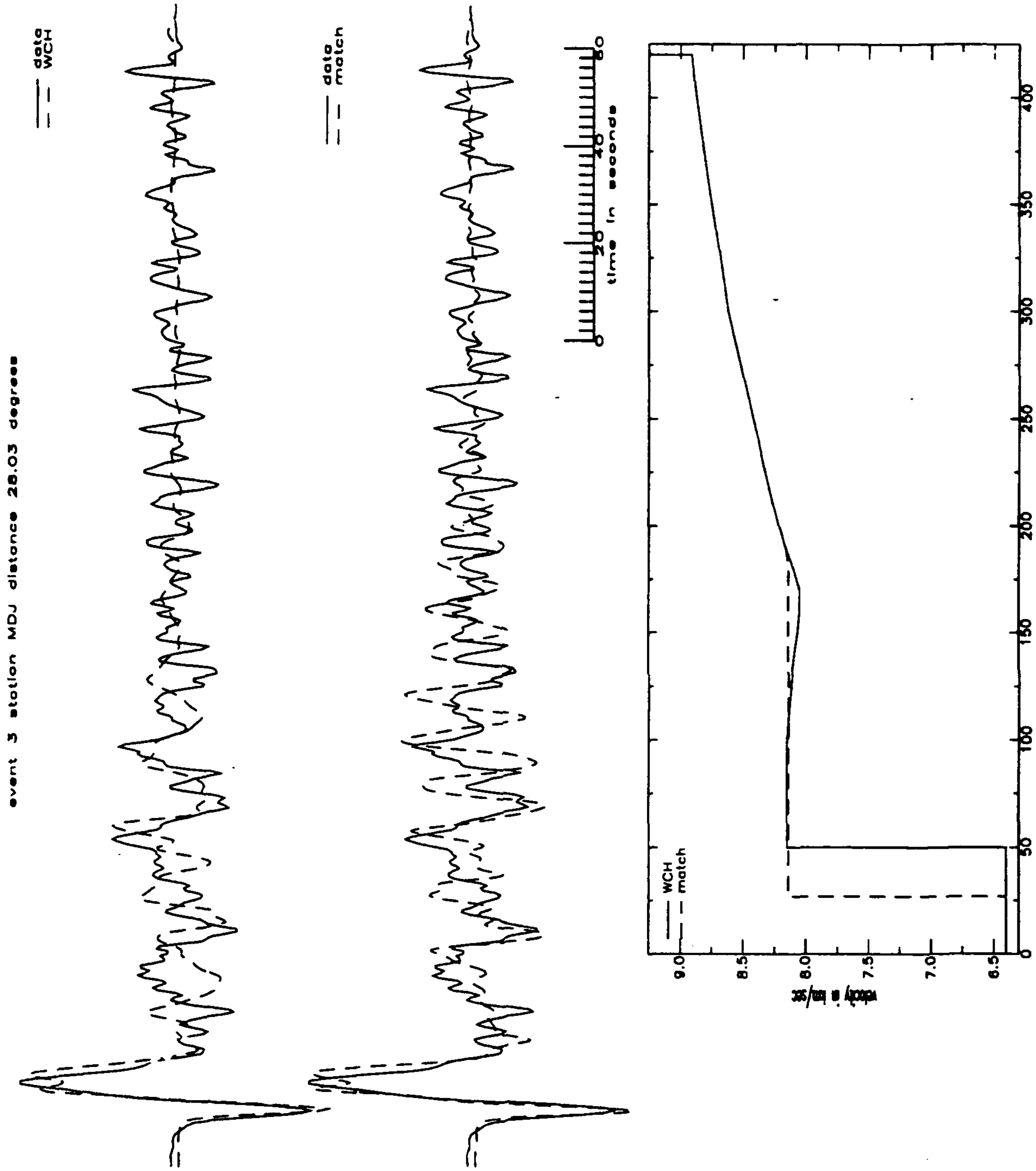
event 3 station MDJ distance 28.03 degrees
data
WCH
data
match
0
20
40
60
time in seconds
WCH
match
9.0
8.5
8.0
7.5
7.0
6.5
velocity in km/sec
0
50
100
150
200
250
300
350
400
depth in km

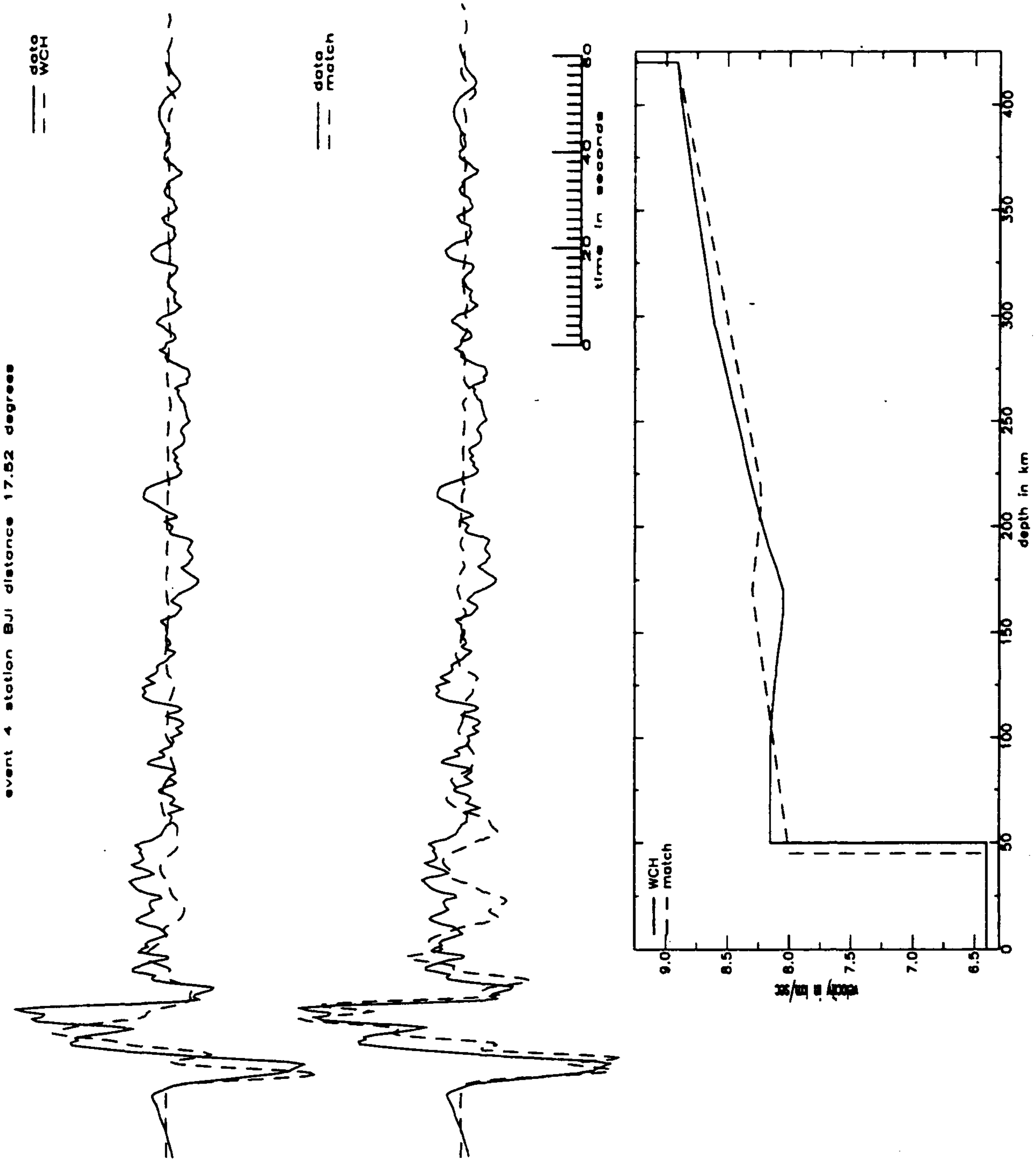

event 4 station BJI distance 17.52 degrees
data
WCH
data
match
0
20
40
60
time in seconds
WCH
match
9.0
8.5
8.0
7.5
7.0
6.5
velocity in km/sec
0
50
100
150
200
250
300
350
400
depth in km

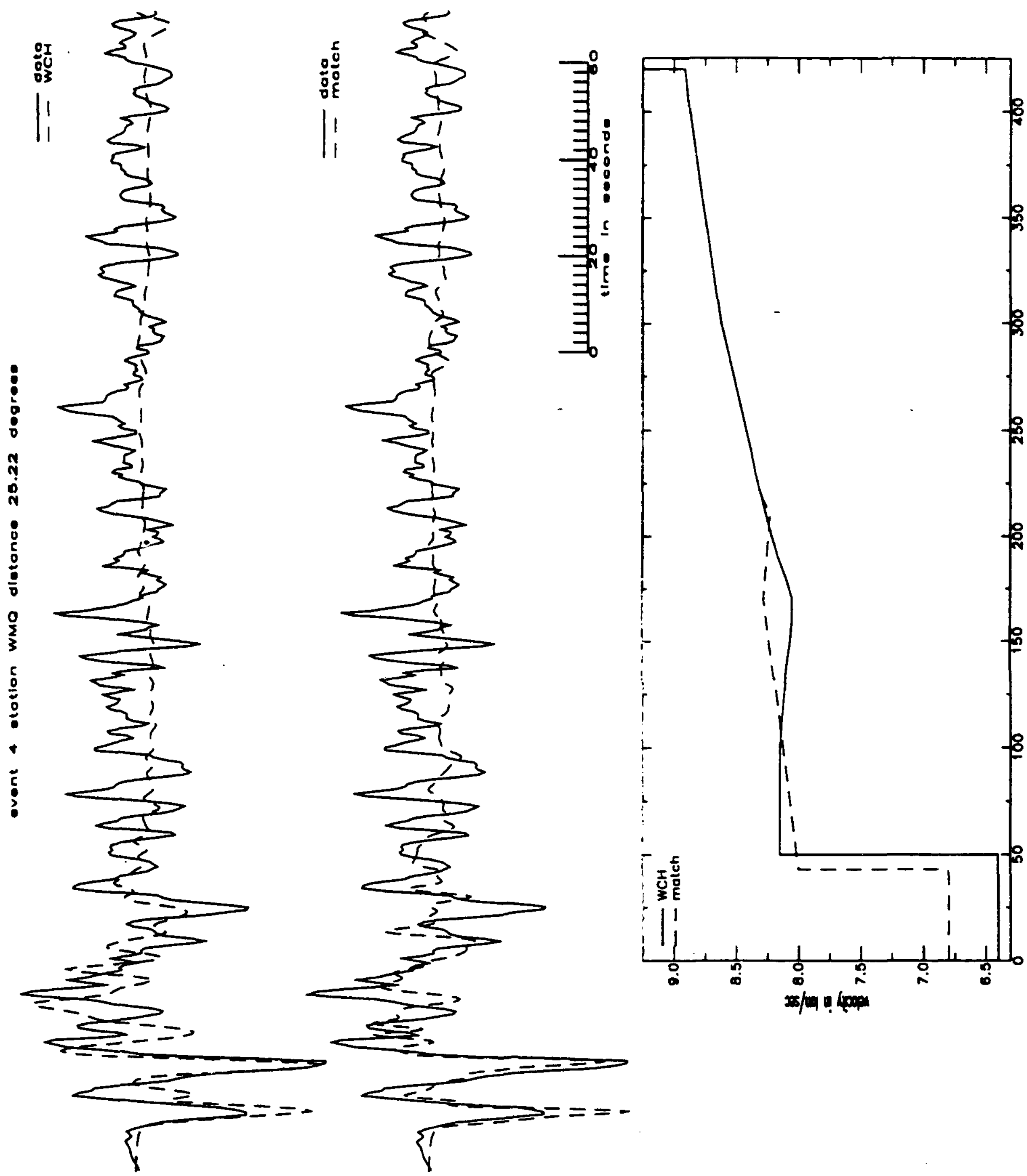
event 4 station WMQ distance 25.22 degrees
data
WCH
data
match
0
20
40
60
time in seconds
WCH
match
9.0
8.5
8.0
7.5
7.0
6.5
velocity in km/sec
0
50
100
150
200
250
300
350
400
depth in km

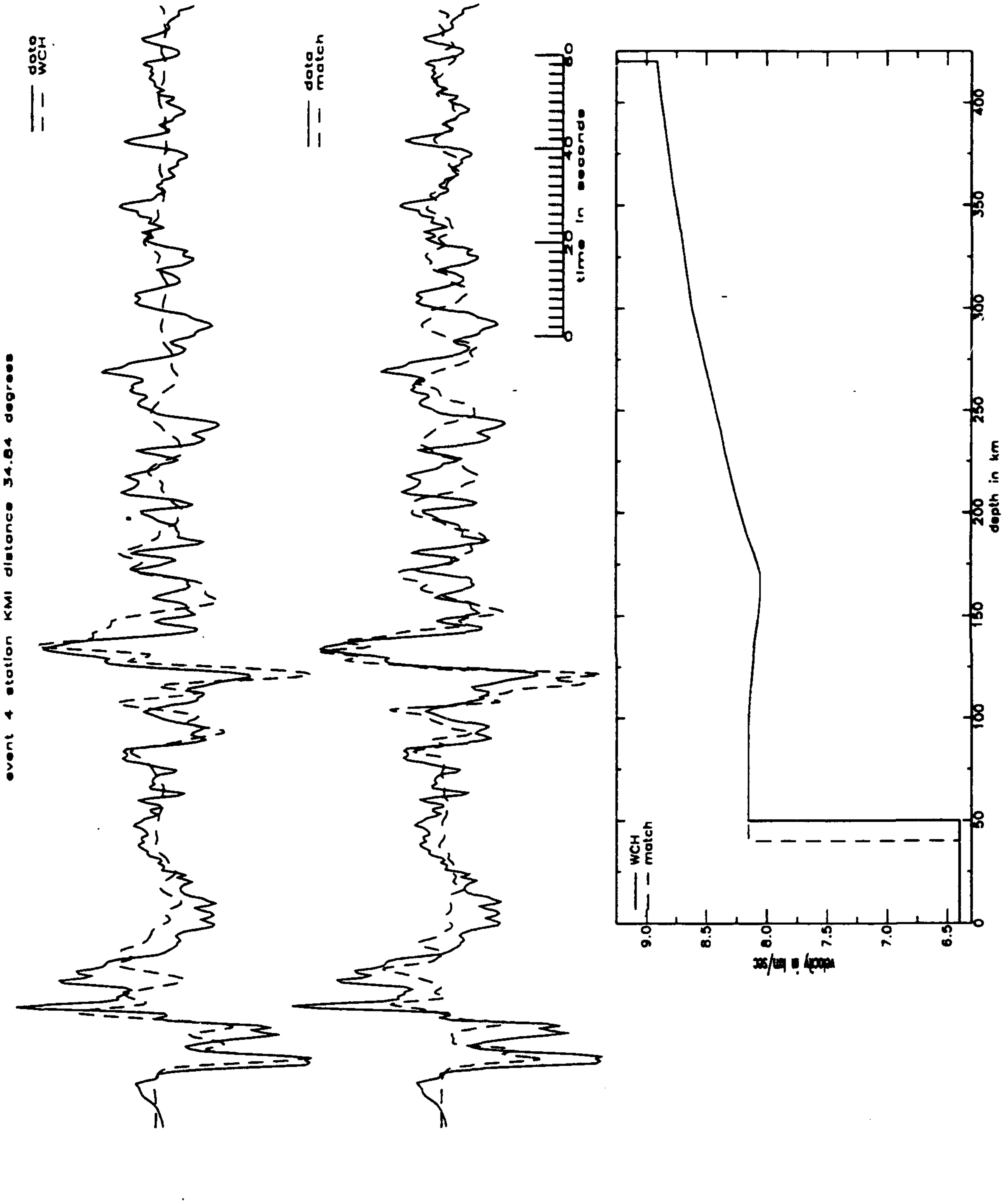
event 4 station KMI distance 34.84 degrees
data
WCH
data
match
time in seconds
0
20
40
60
WCH
match
velocity in km/sec
9.0
8.5
8.0
7.5
7.0
6.5
depth in km
0
50
100
150
200
250
300
350
400

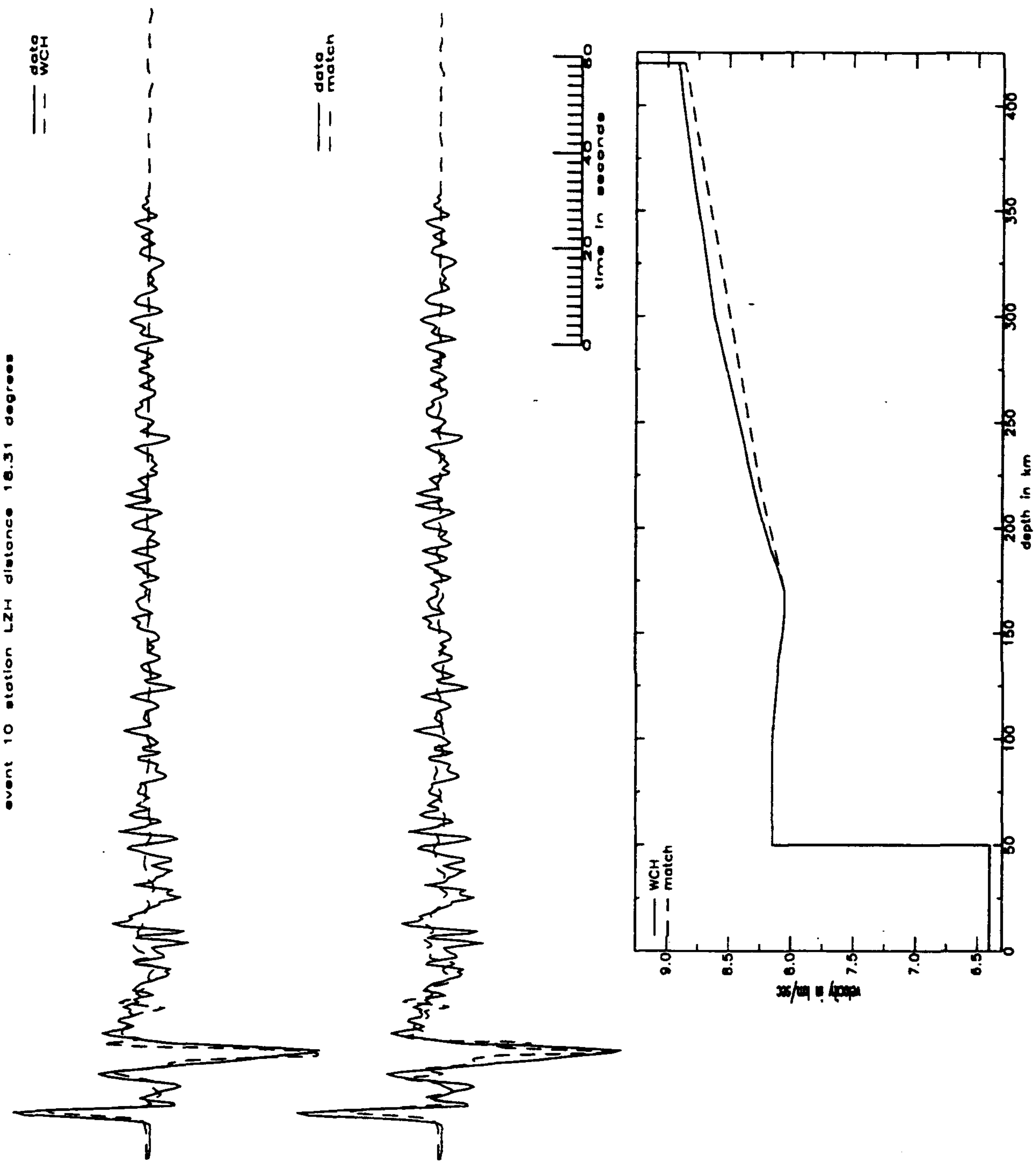
event 10 station LZH distance 18.31 degrees
data
WCH
data
match
0
20
40
60
time in seconds
WCH
match
9.0
8.5
8.0
7.5
7.0
6.5
velocity in km/sec
0
50
100
150
200
250
300
350
400
depth in km

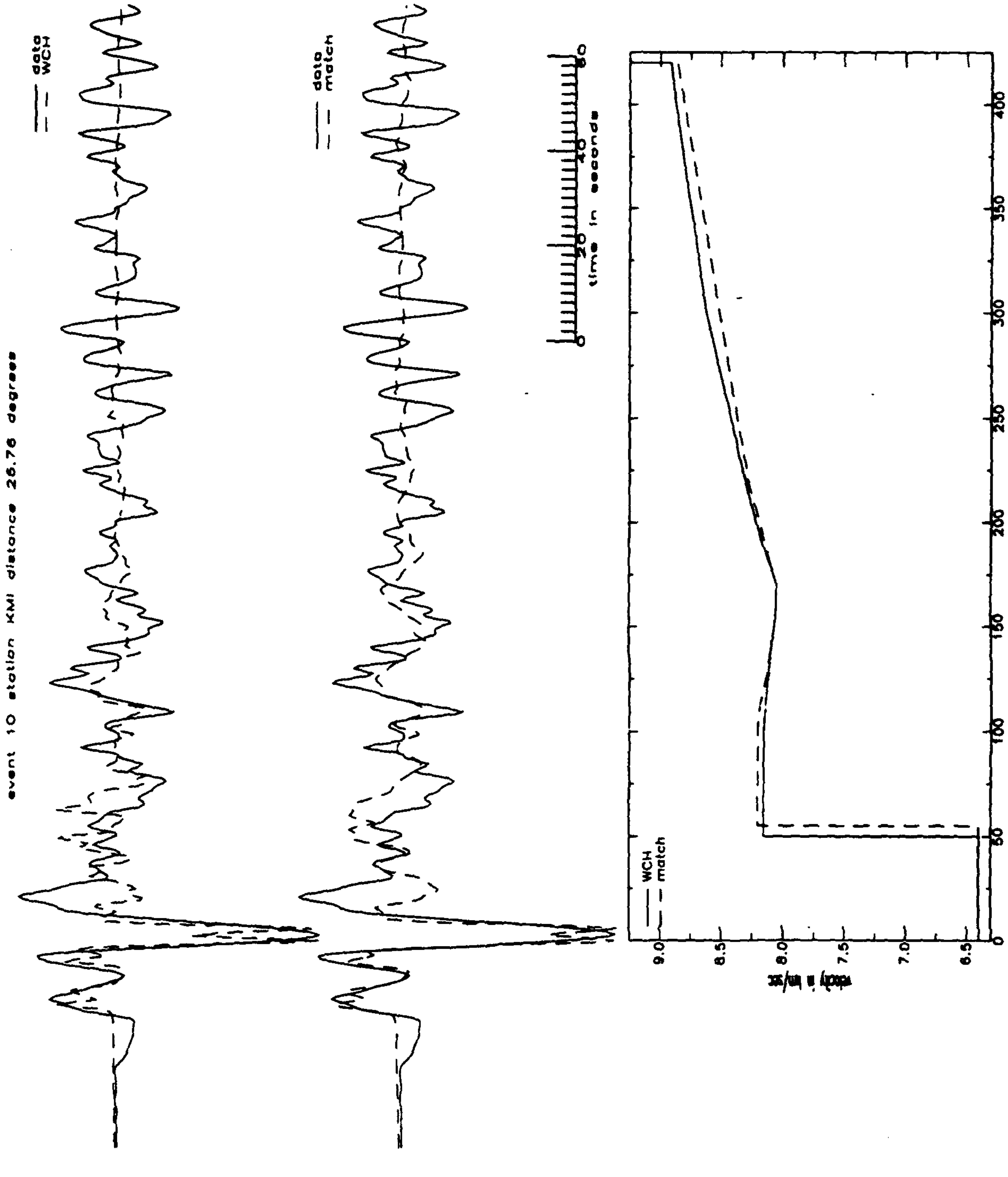
event 10 station KMI distance 26.76 degrees
data
WCH
data
match
time in seconds
0
20
40
60
WCH
match
velocity in km/sec
9.0
8.5
8.0
7.5
7.0
6.5
depth in km
0
50
100
150
200
250
300
350
400

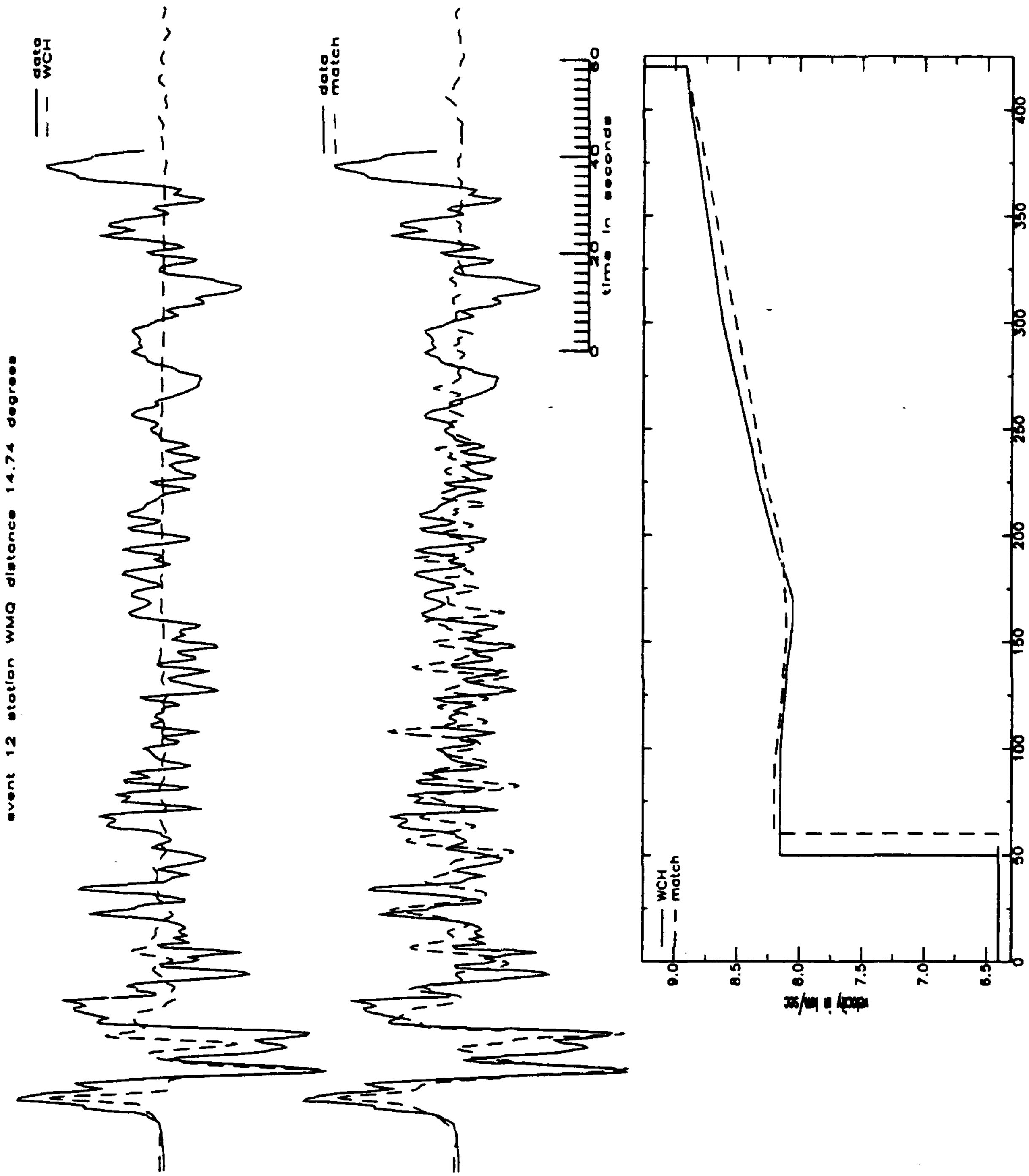

event 12 station WMQ distance 14.74 degrees
data
WCH
data
match
0
20
40
60
time in seconds
WCH
match
9.0
8.5
8.0
7.5
7.0
6.5
velocity in km/sec
0
50
100
150
200
250
300
350
400
depth in km

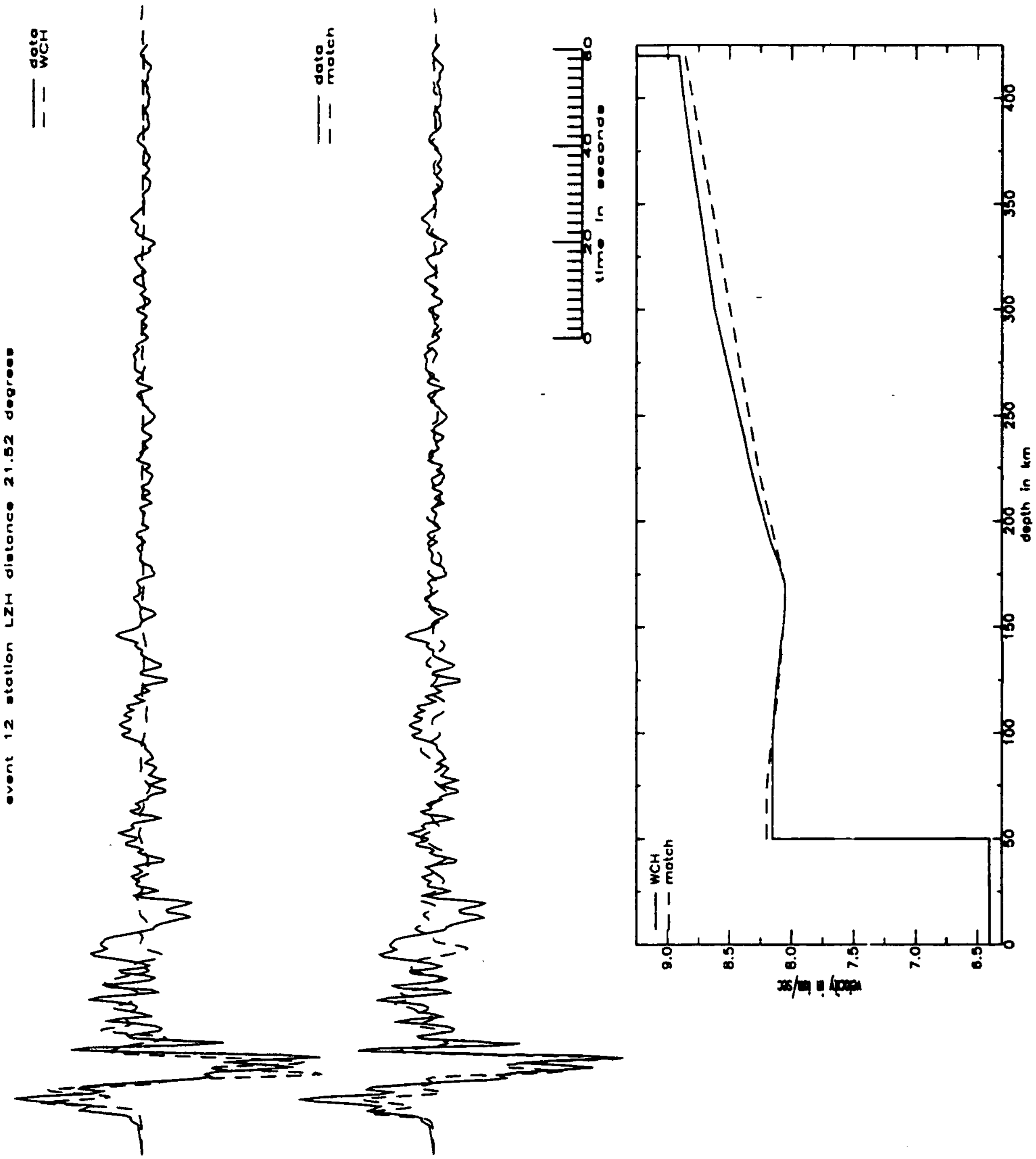

event 12 station LZH distance 21.52 degrees
data
WCH
data
match
0
20
40
60
time in seconds
WCH
match
9.0
8.5
8.0
7.5
7.0
6.5
velocity in km/sec
0
50
100
150
200
250
300
350
400
depth in km

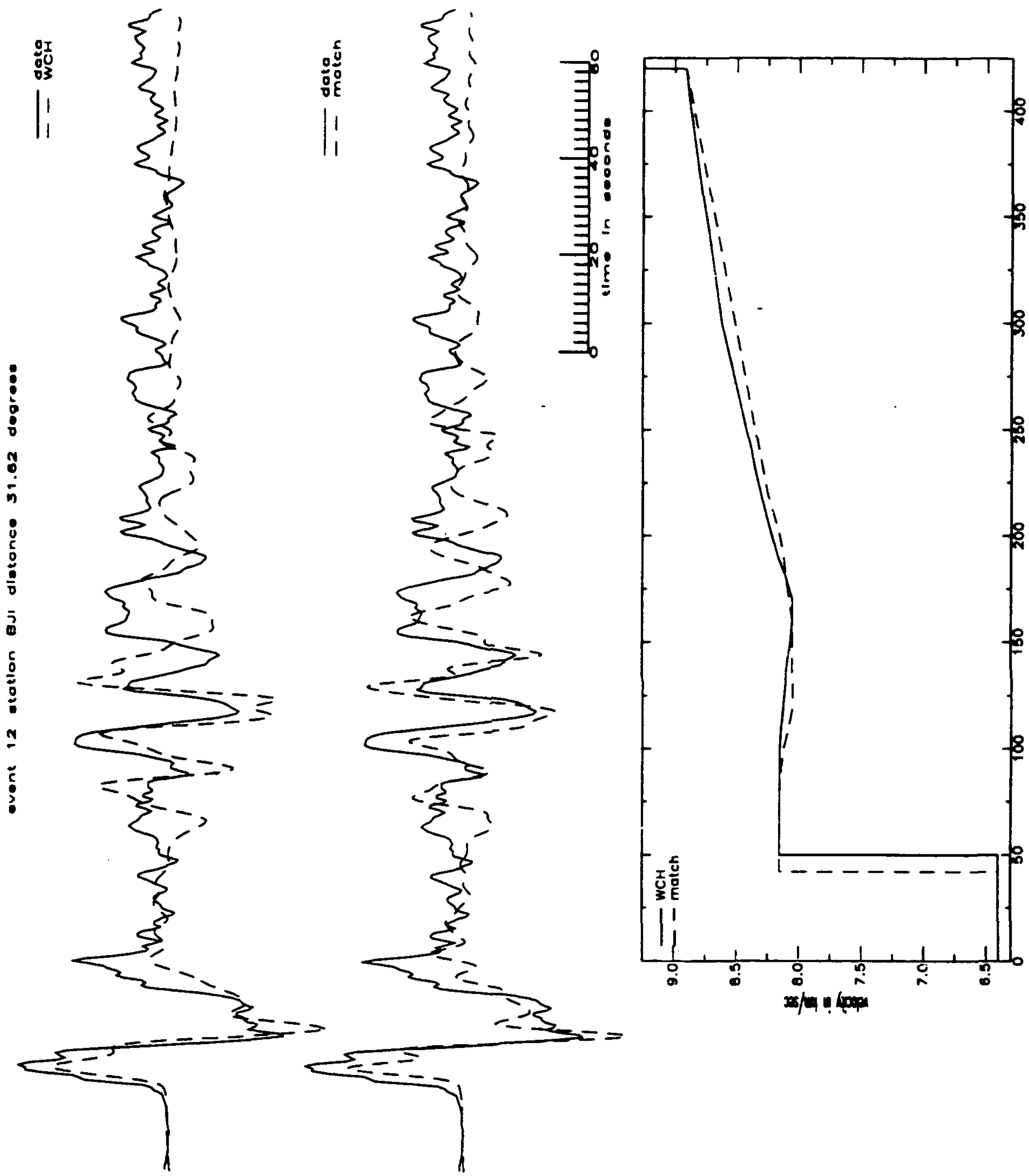
event 12 station BJI distance 31.62 degrees
data
WCH
data
match
0
20
40
60
time in seconds
WCH
match
9.0
8.5
8.0
7.5
7.0
6.5
velocity in km/sec
0
50
100
150
200
250
300
350
400
depth in km

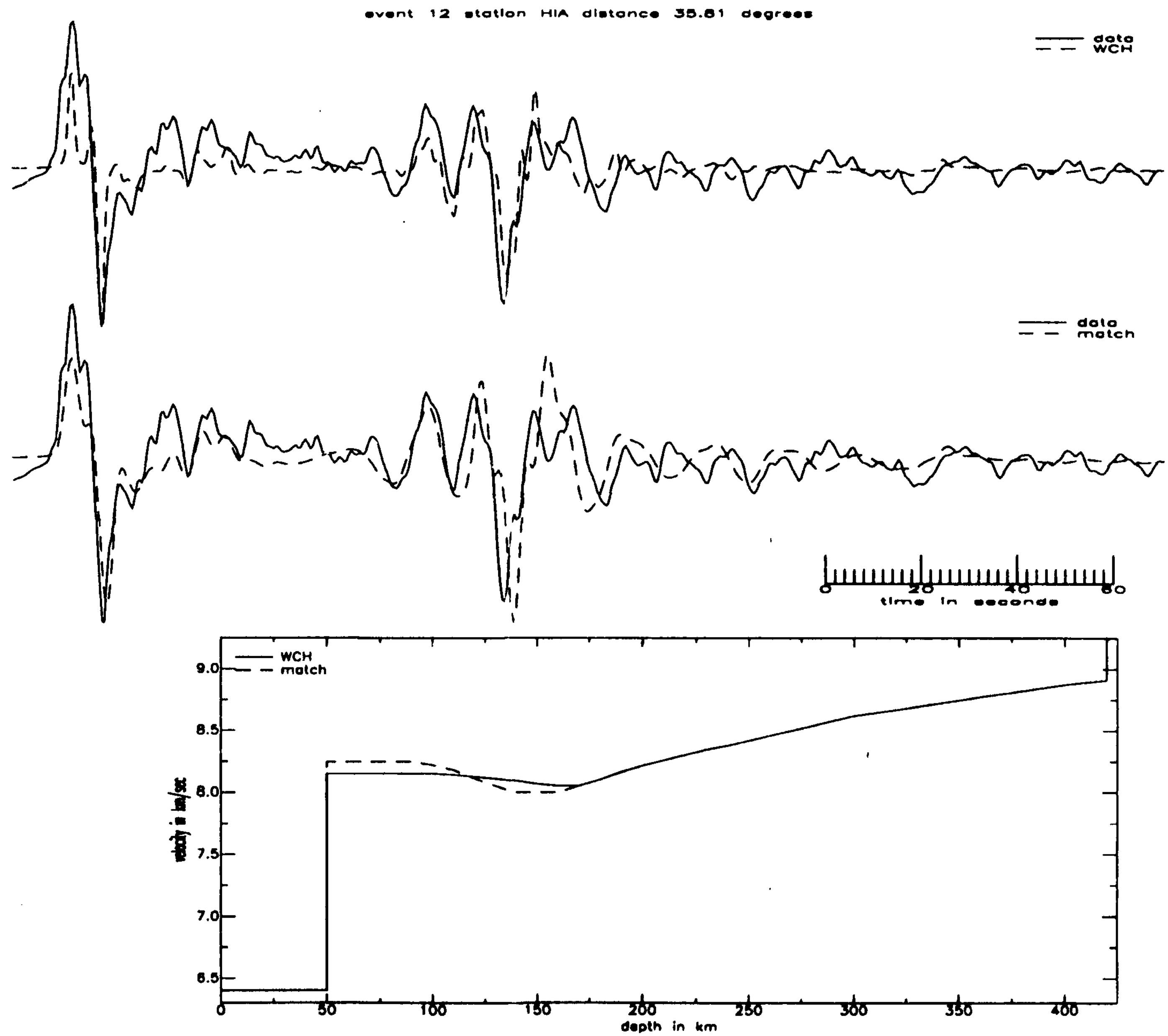

event 12 station HIA distance 35.81 degrees
data
WCH
data
match
0
20
40
60
time in seconds
WCH
match
9.0
8.5
8.0
7.5
7.0
6.5
velocity in km/sec
0
50
100
150
200
250
300
350
400
depth in km

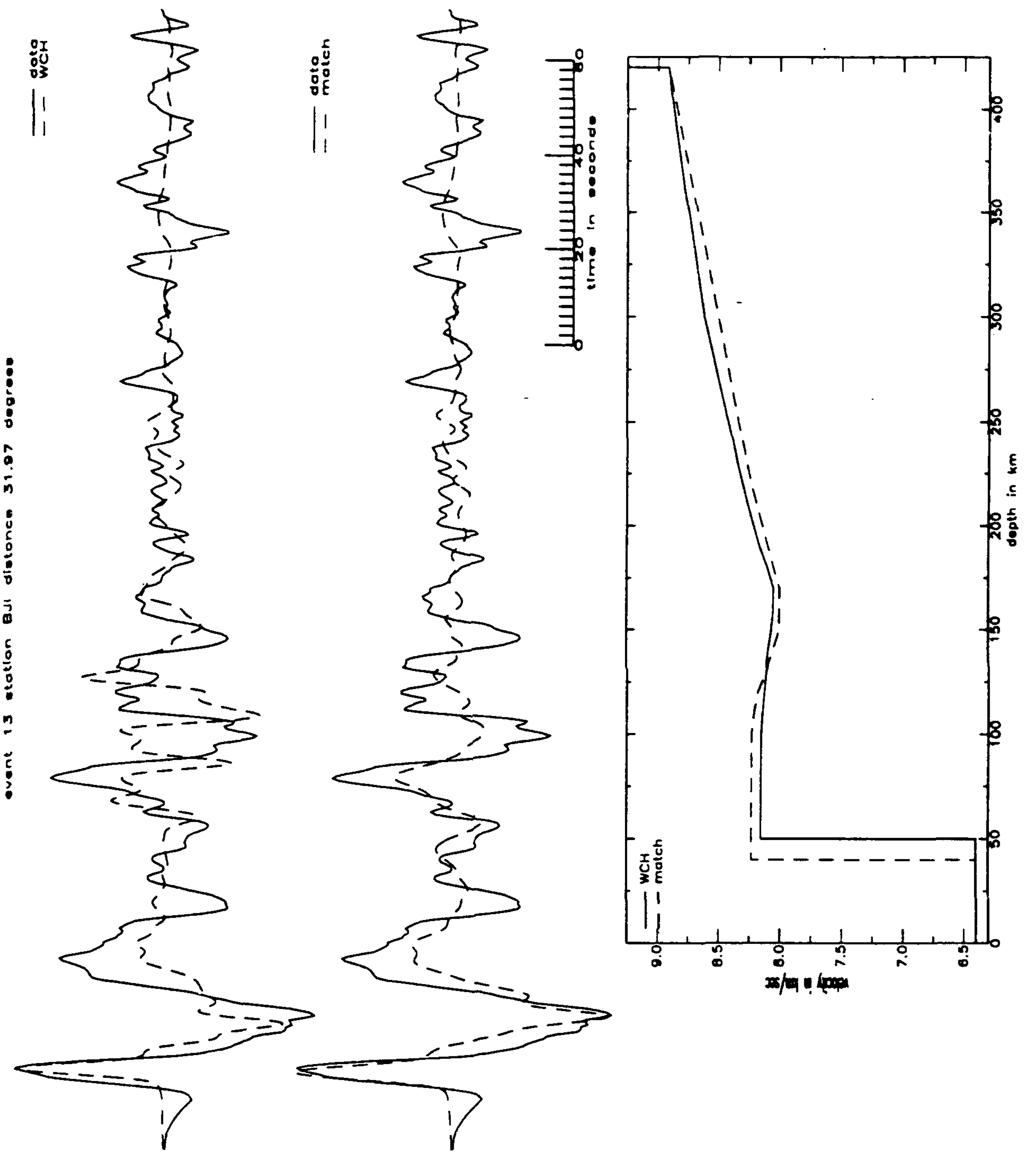

event 13 station BJI distance 31.97 degrees
data
WCH
data
match
time in seconds
0
20
40
60
WCH
match
velocity in km/sec
9.0
8.5
8.0
7.5
7.0
6.5
depth in km
0
50
100
150
200
250
300
350
400

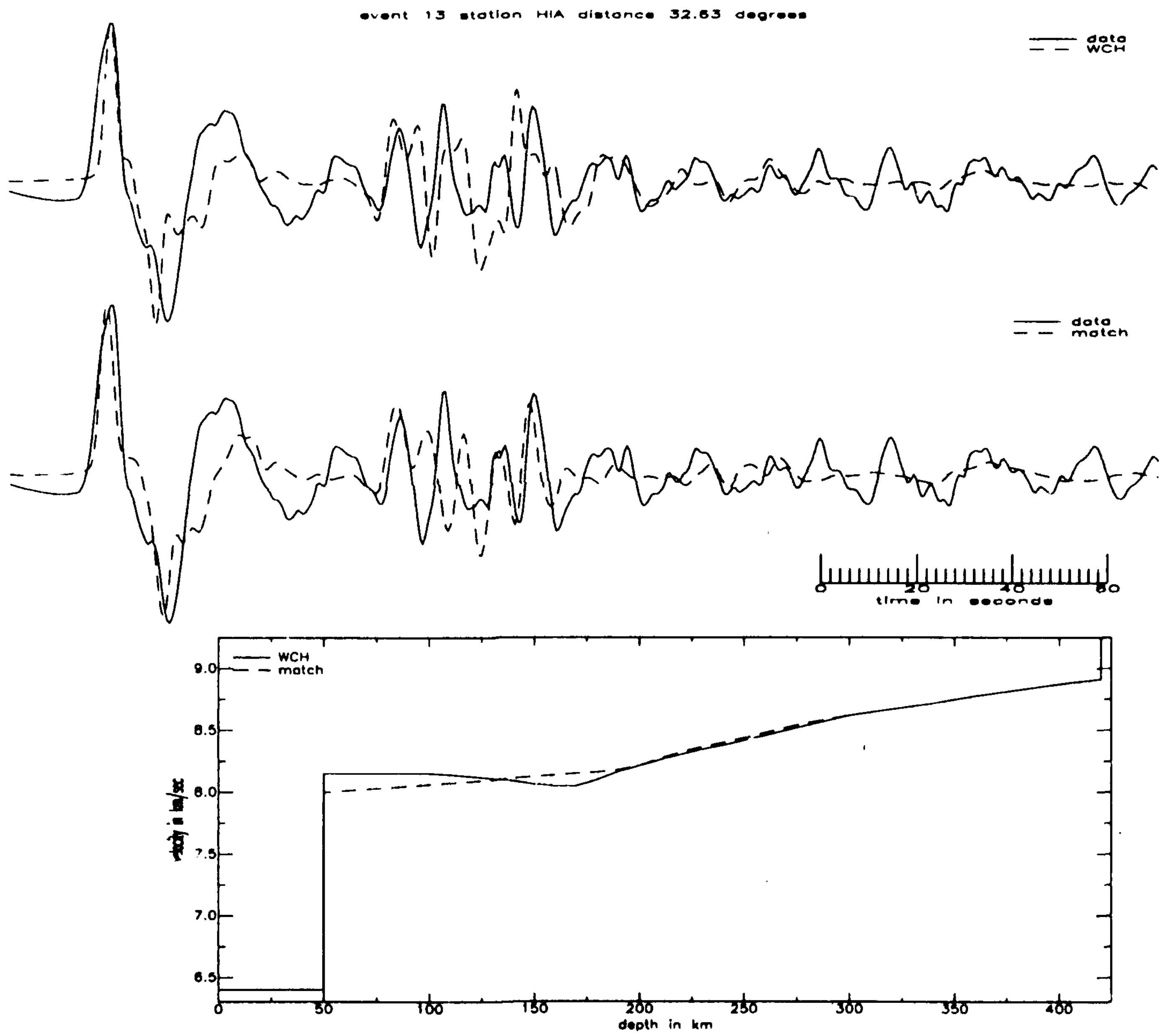

event 13 station HIA distance 32.63 degrees
data
WCH
data
match
0
20
40
60
time in seconds
WCH
match
9.0
8.5
8.0
7.5
7.0
6.5
velocity in km/sec
0
50
100
150
200
250
300
350
400
depth in km

Appendix C

Overview of synthetic regional waveforms generated to explore the effect of the regionalized Chinese velocity models (Figure 12) on the propagation of the P_n and L_g phases. Synthetics are calculated in the 1^o-10^o distance range at 1^o intervals. The waveforms are plotted with a reduction velocity of 8.2 km/s and are normalized to their peak amplitudes.

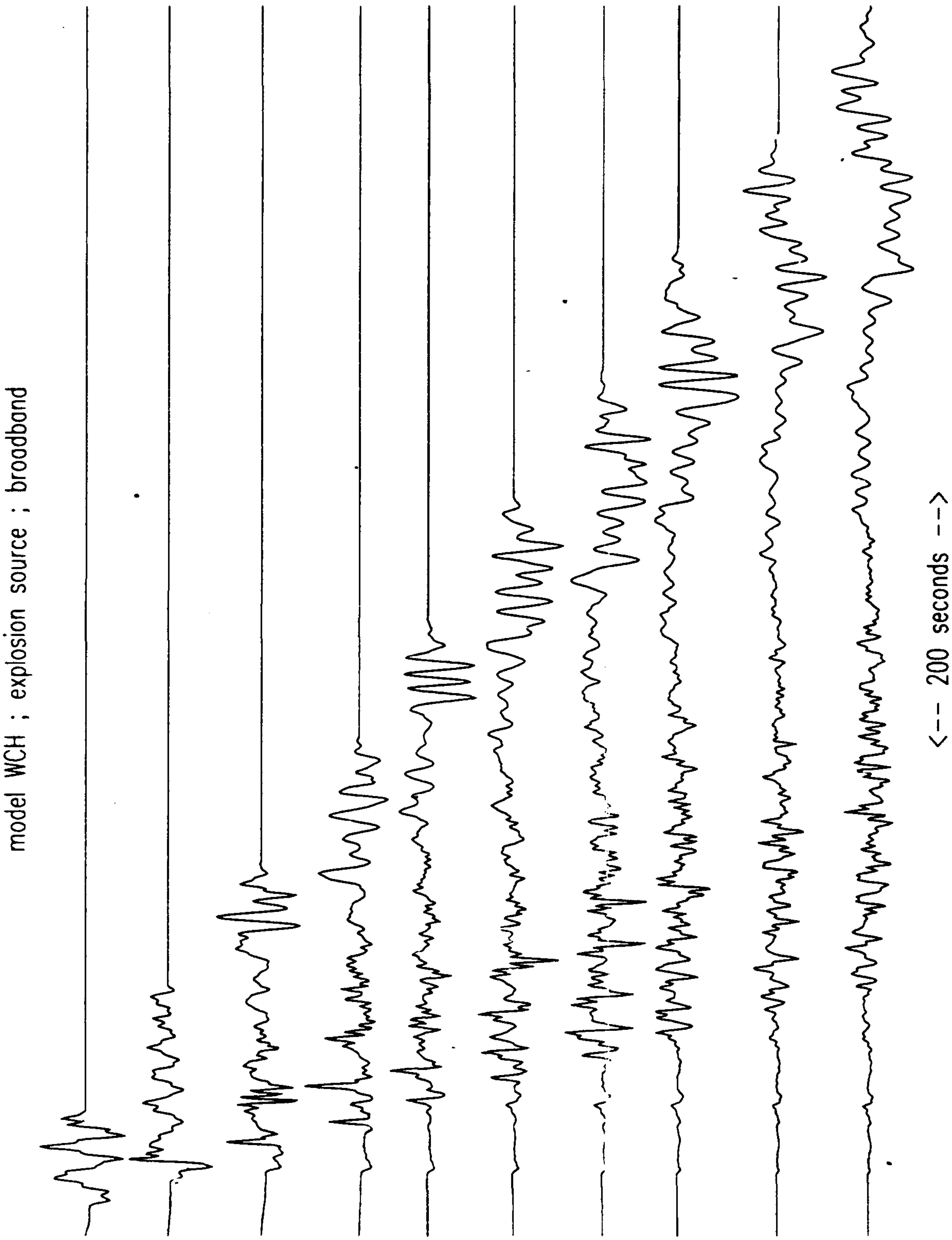
model WCH ; explosion source ; broadband
<-- 200 seconds -->

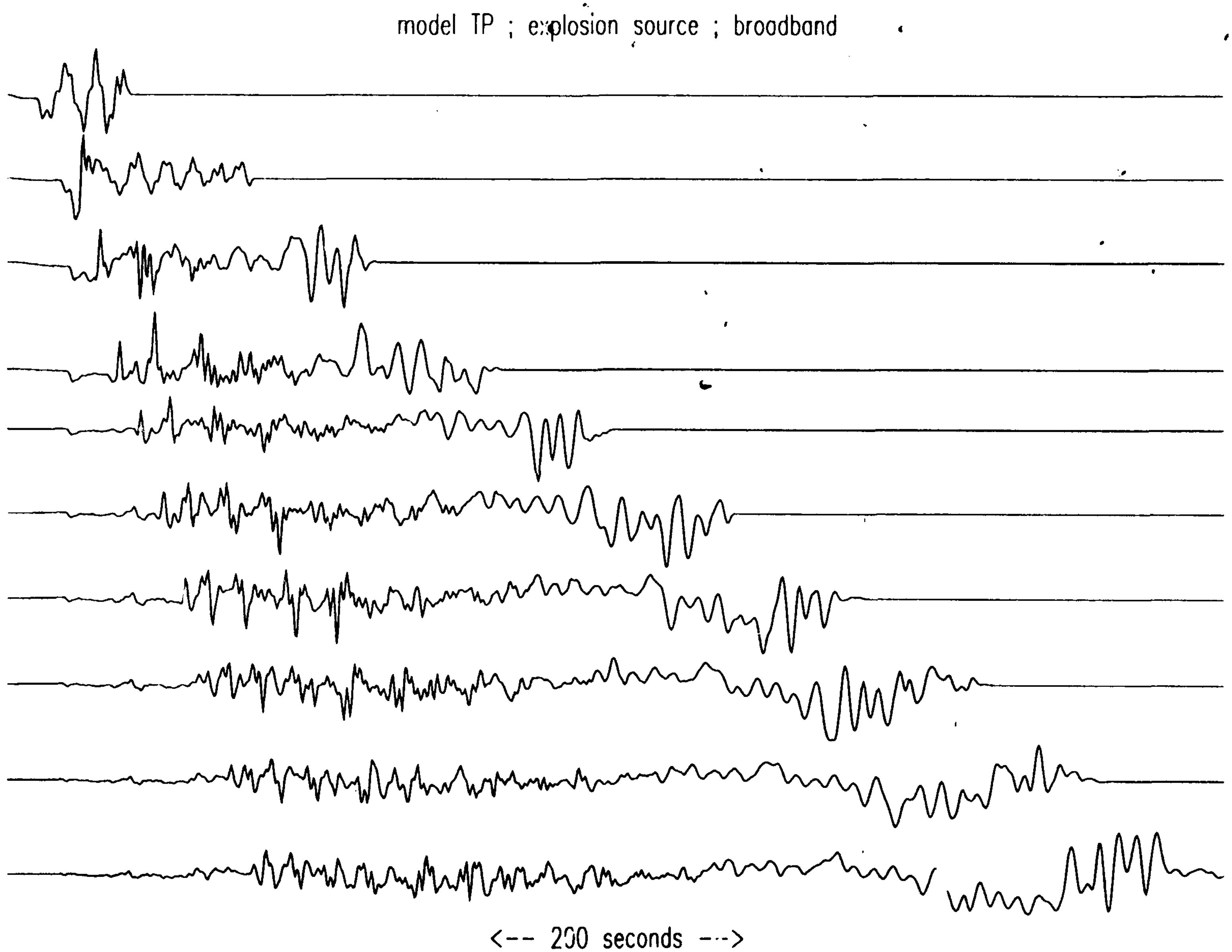
model TP ; explosion source ; broadband
<-- 200 seconds -->

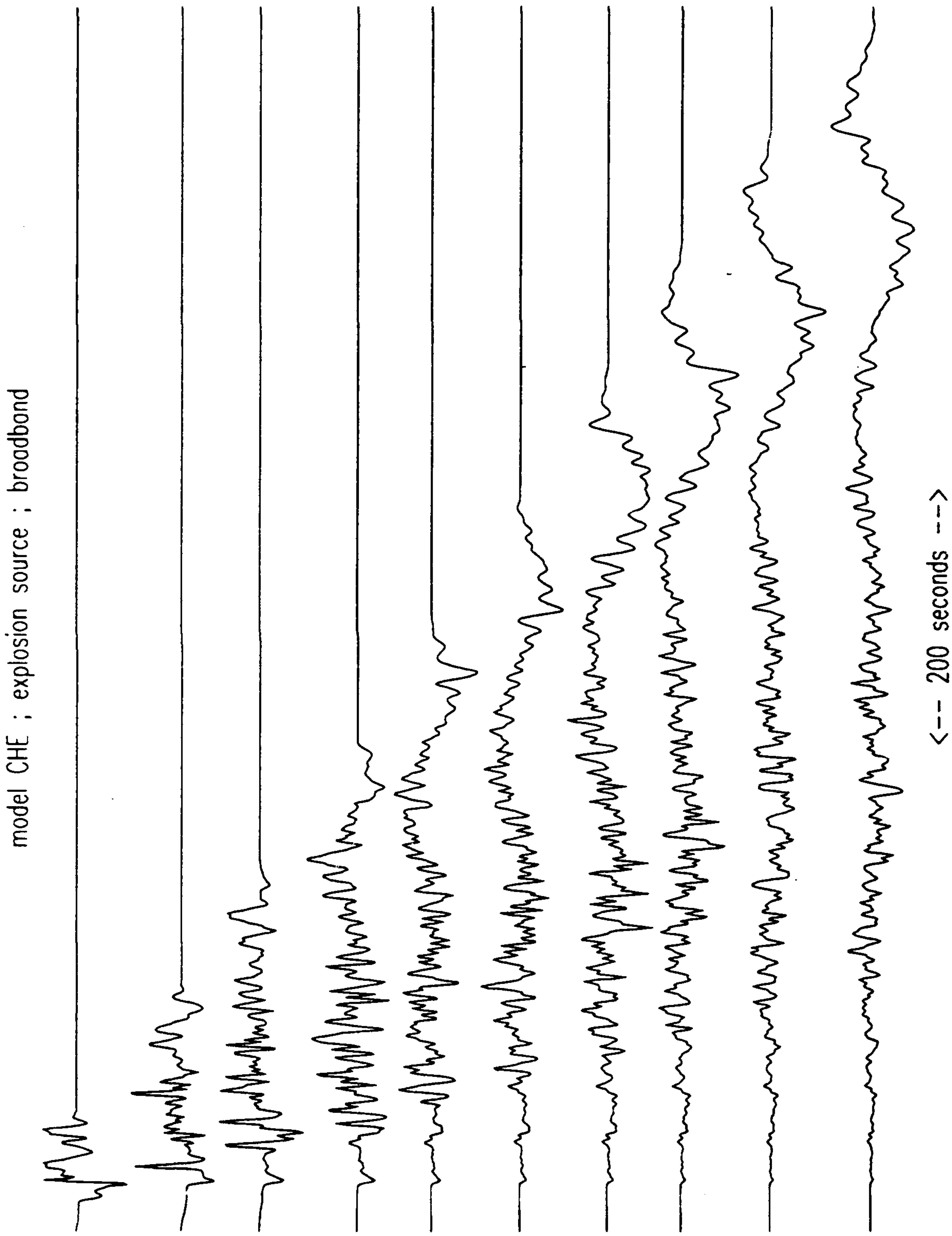
model CHE ; explosion source ; broadband
<-- 200 seconds -->

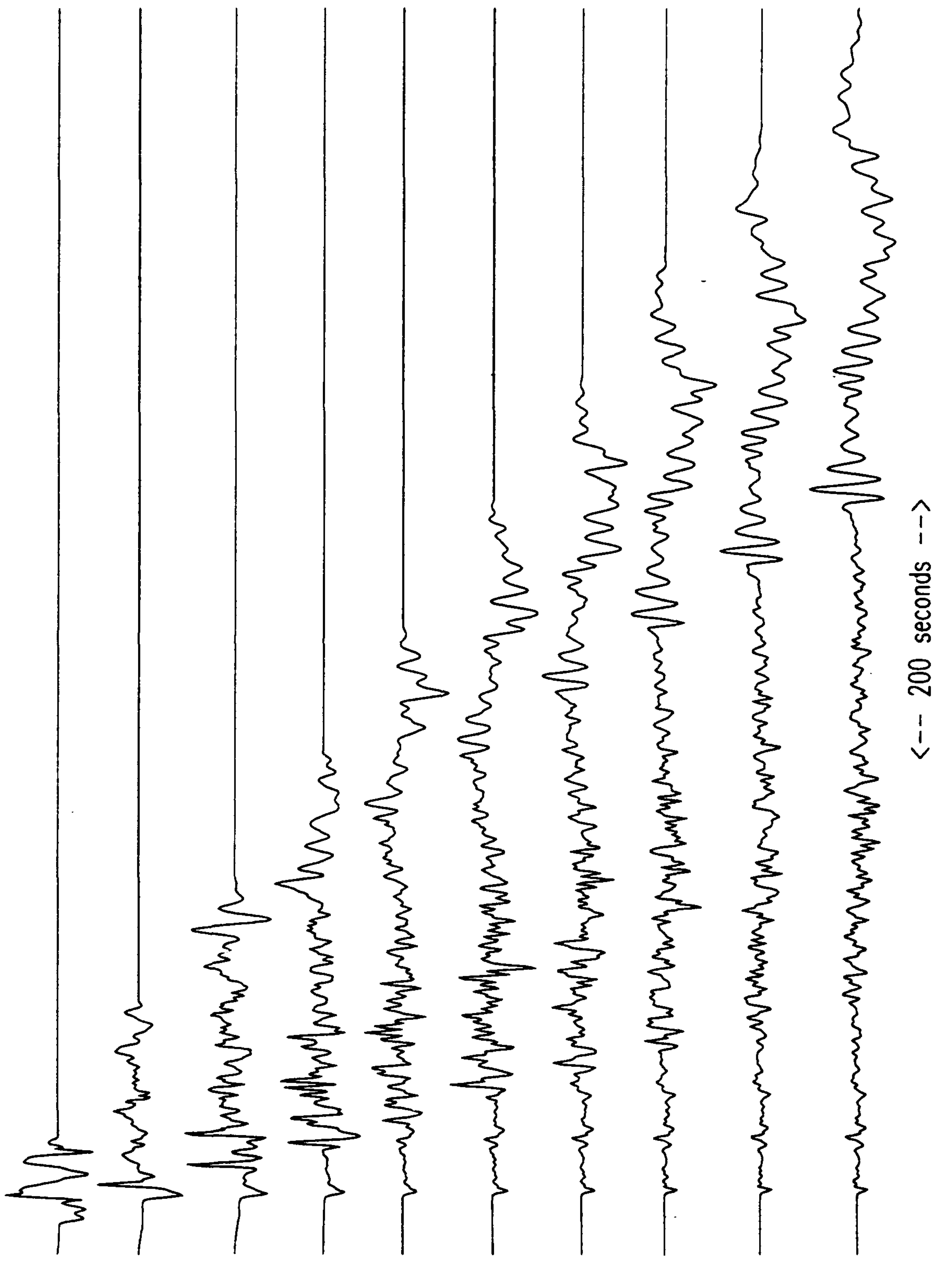
model NCH ; explosion source ; broadband
<-- 200 seconds -->

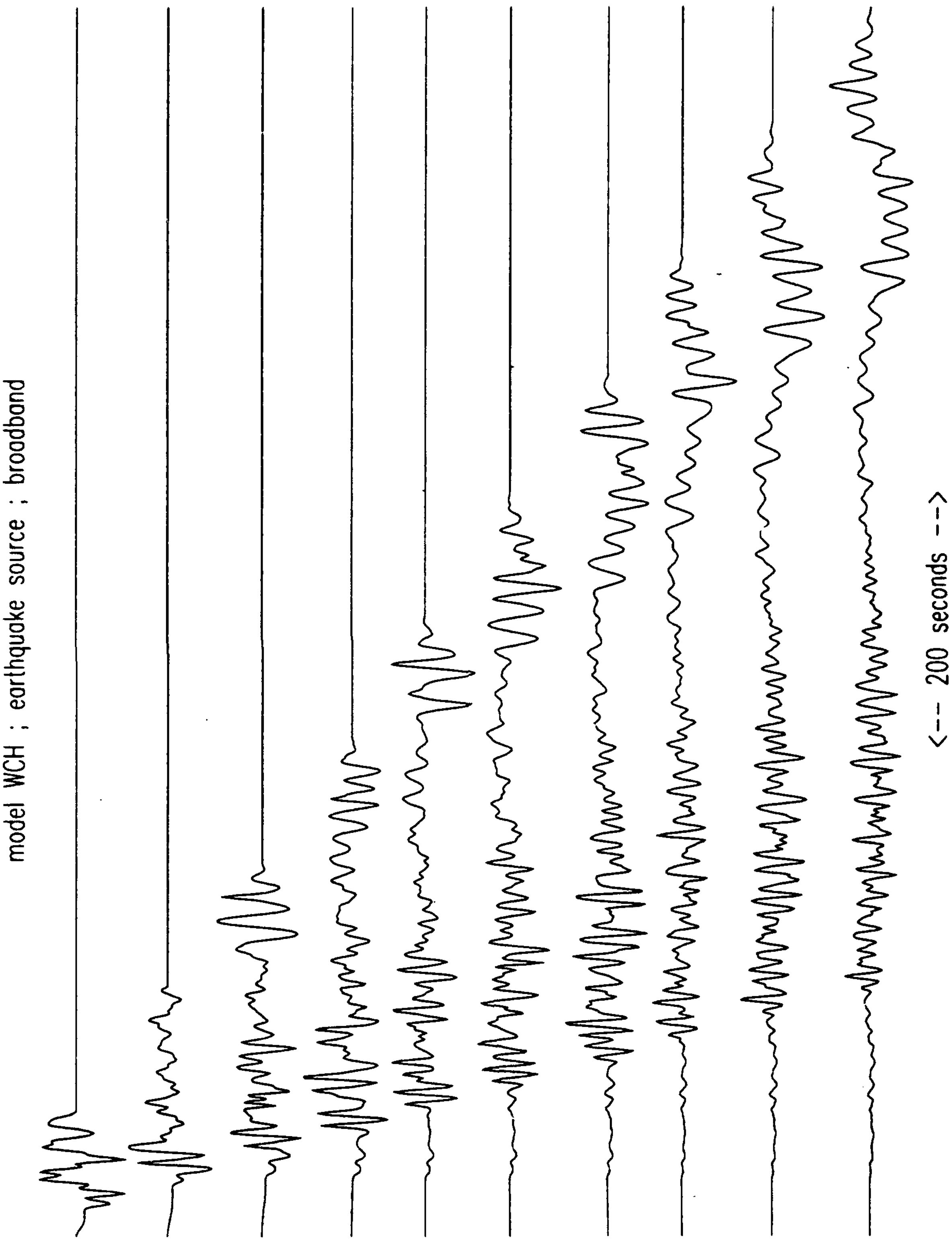
model WCH ; earthquake source ; broadband
<-- 200 seconds -->

model TP ; earthquake source ; broadband

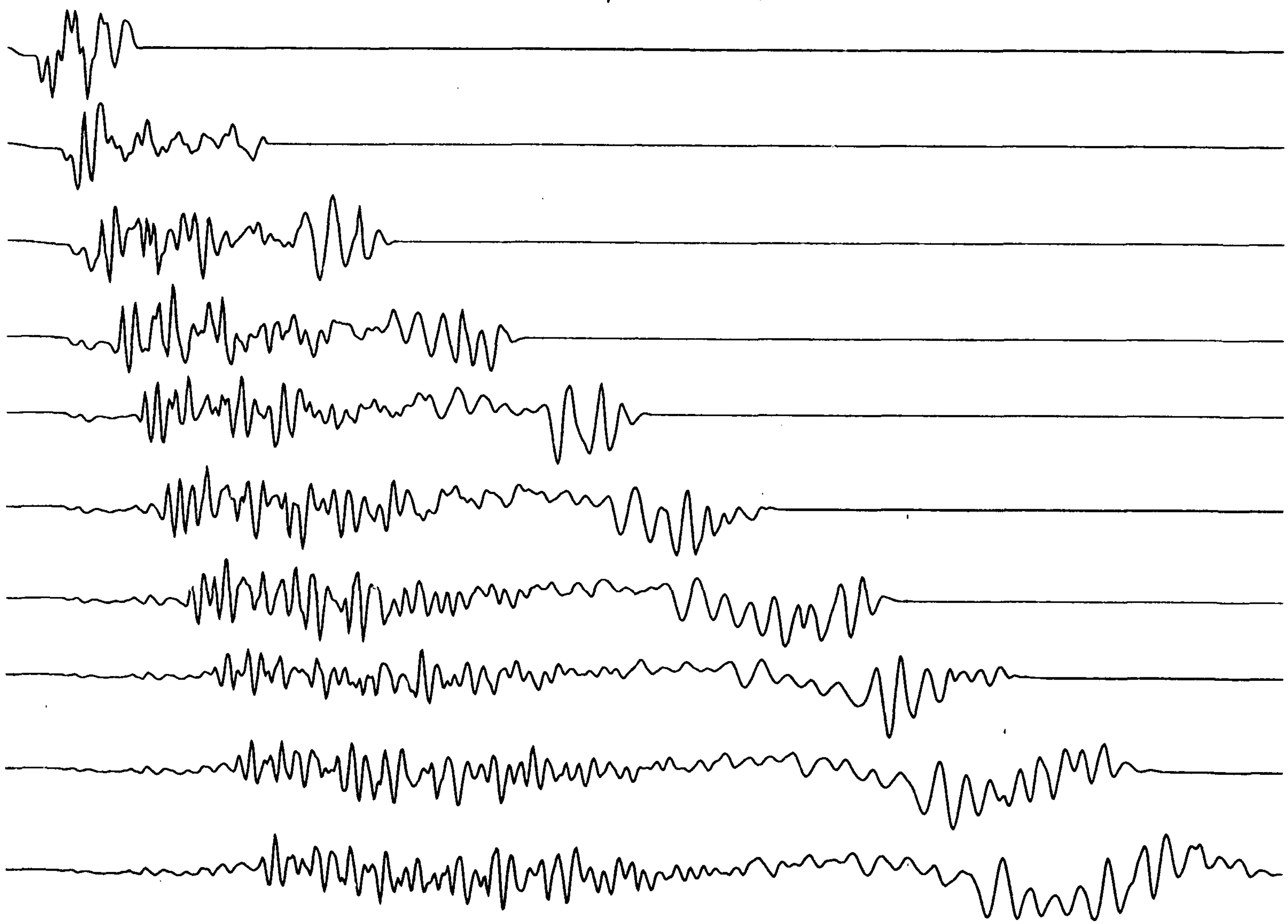

<-- 200 seconds -->

model CHE ; earthquake source ; broadband

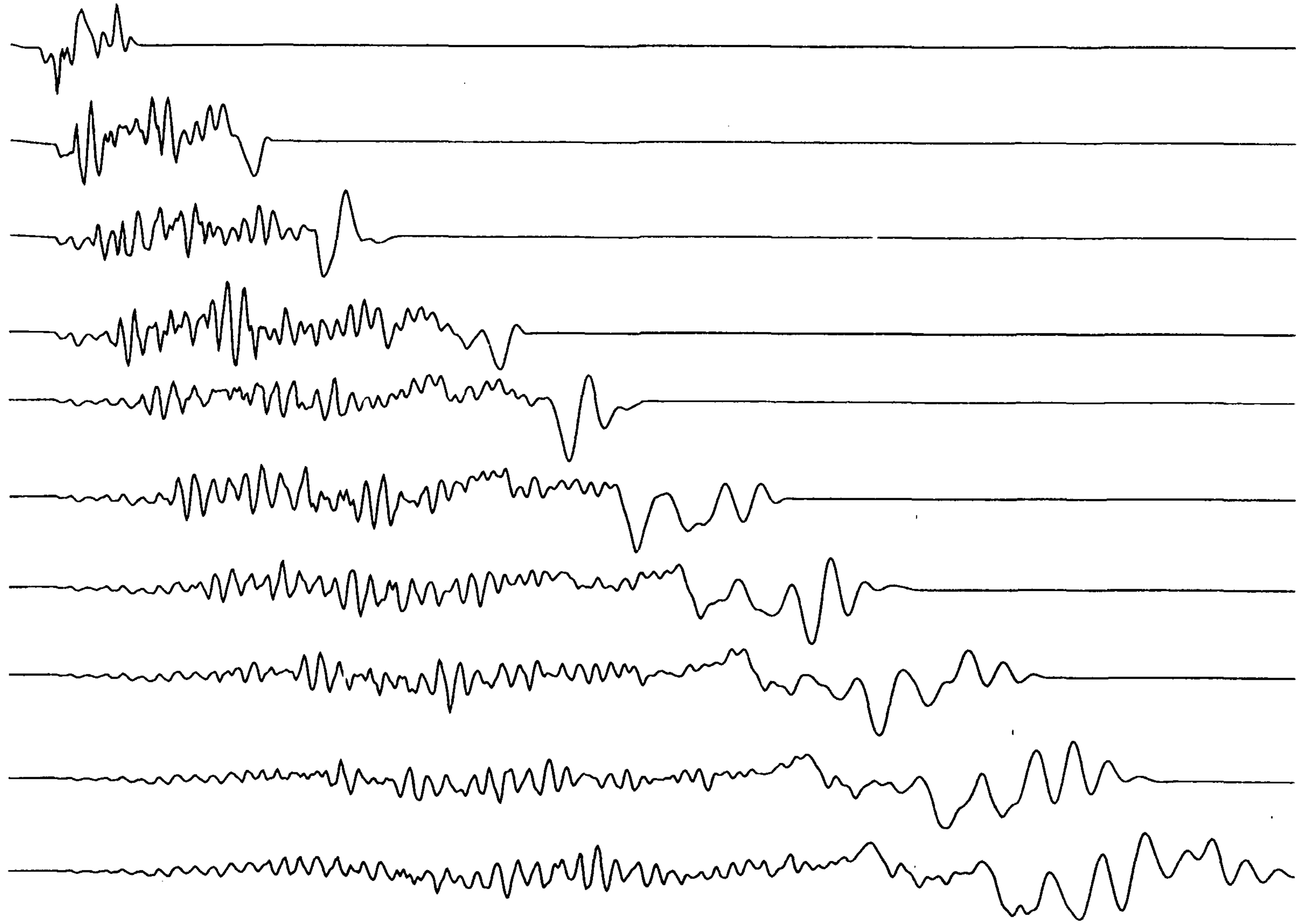

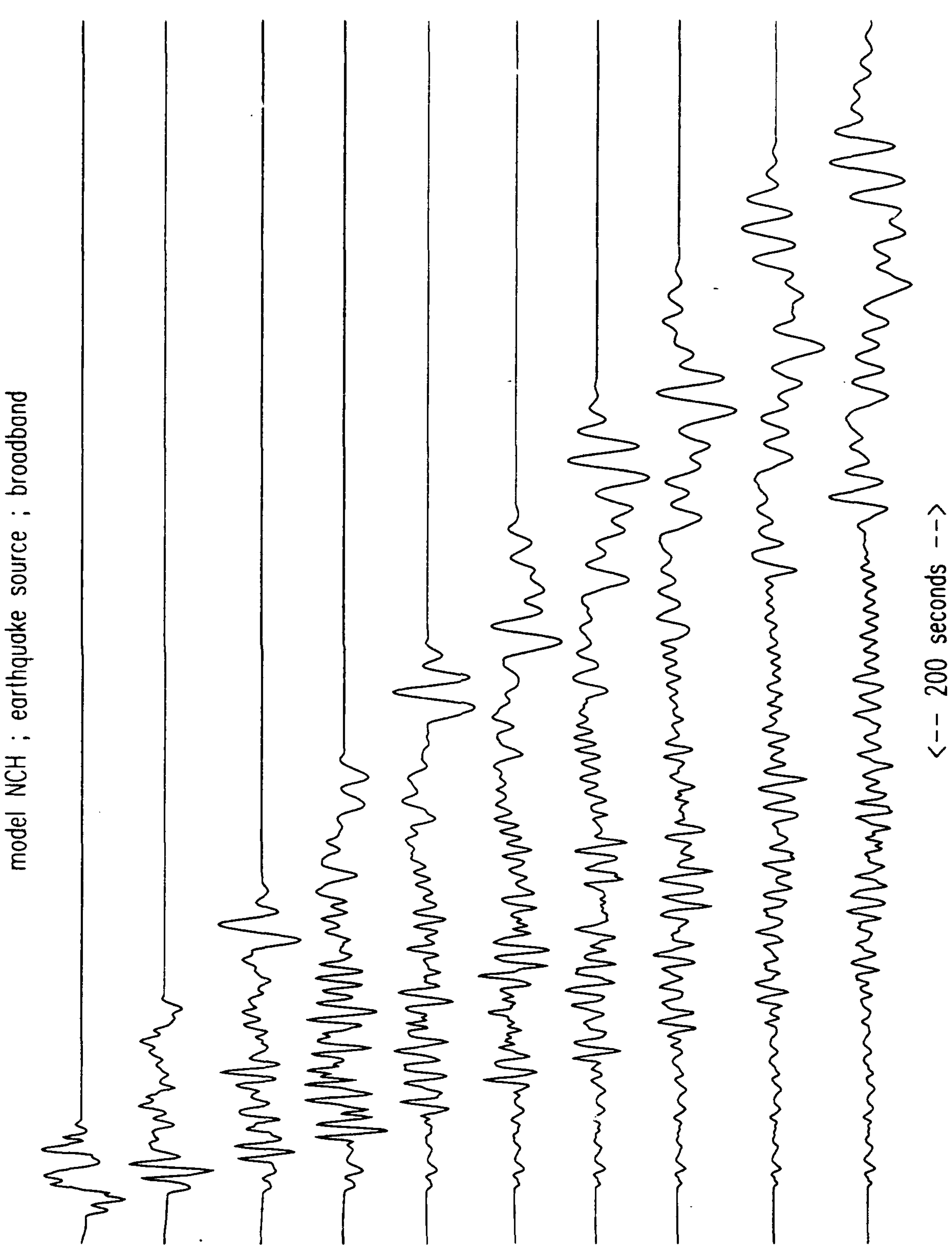
model NCH ; earthquake source ; broadband
<-- 200 seconds -->

model WCH ; explosion source ; short-period

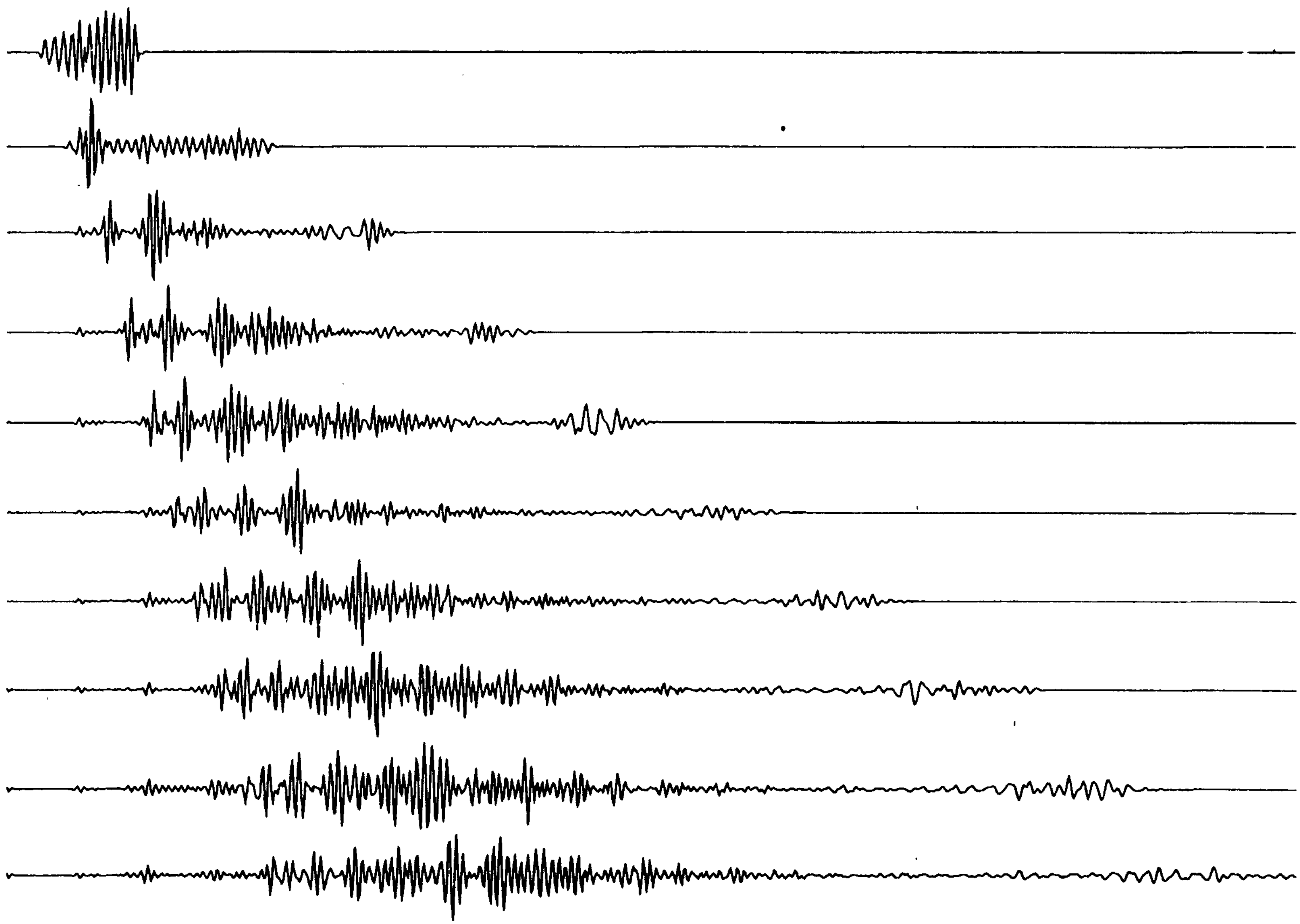

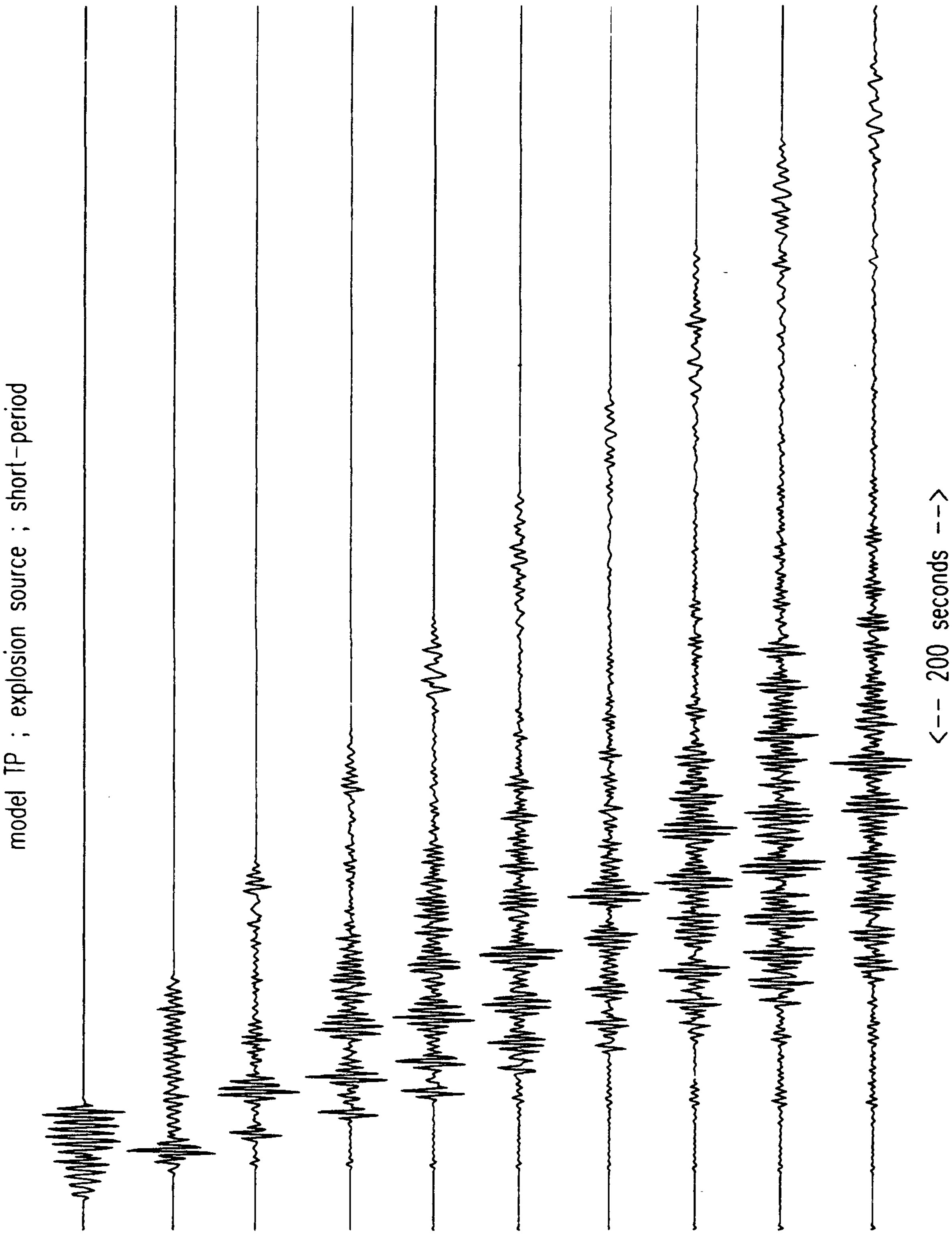
model TP ; explosion source ; short-period
<-- 200 seconds -->

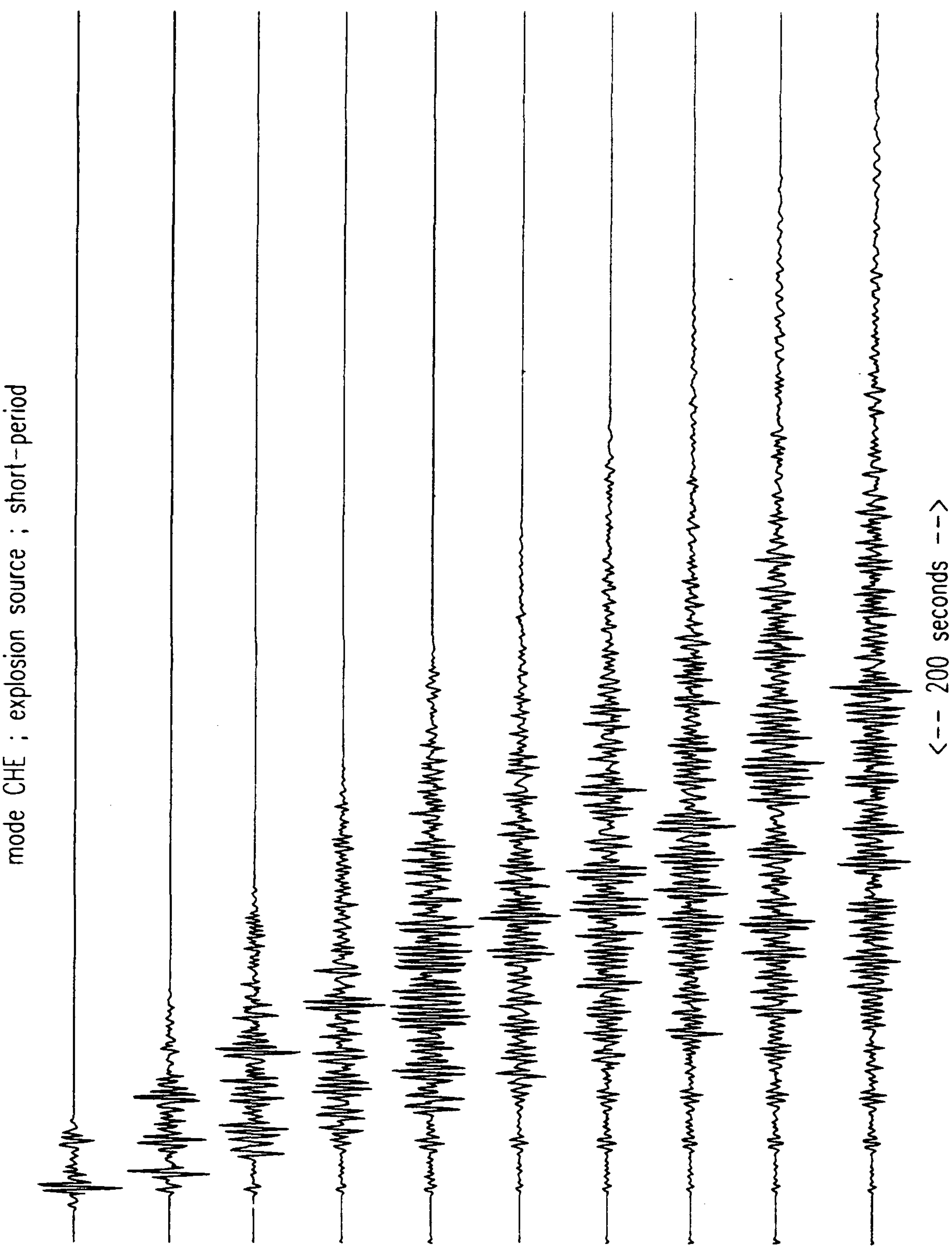
mode CHE ; explosion source ; short-period
<-- 200 seconds -->

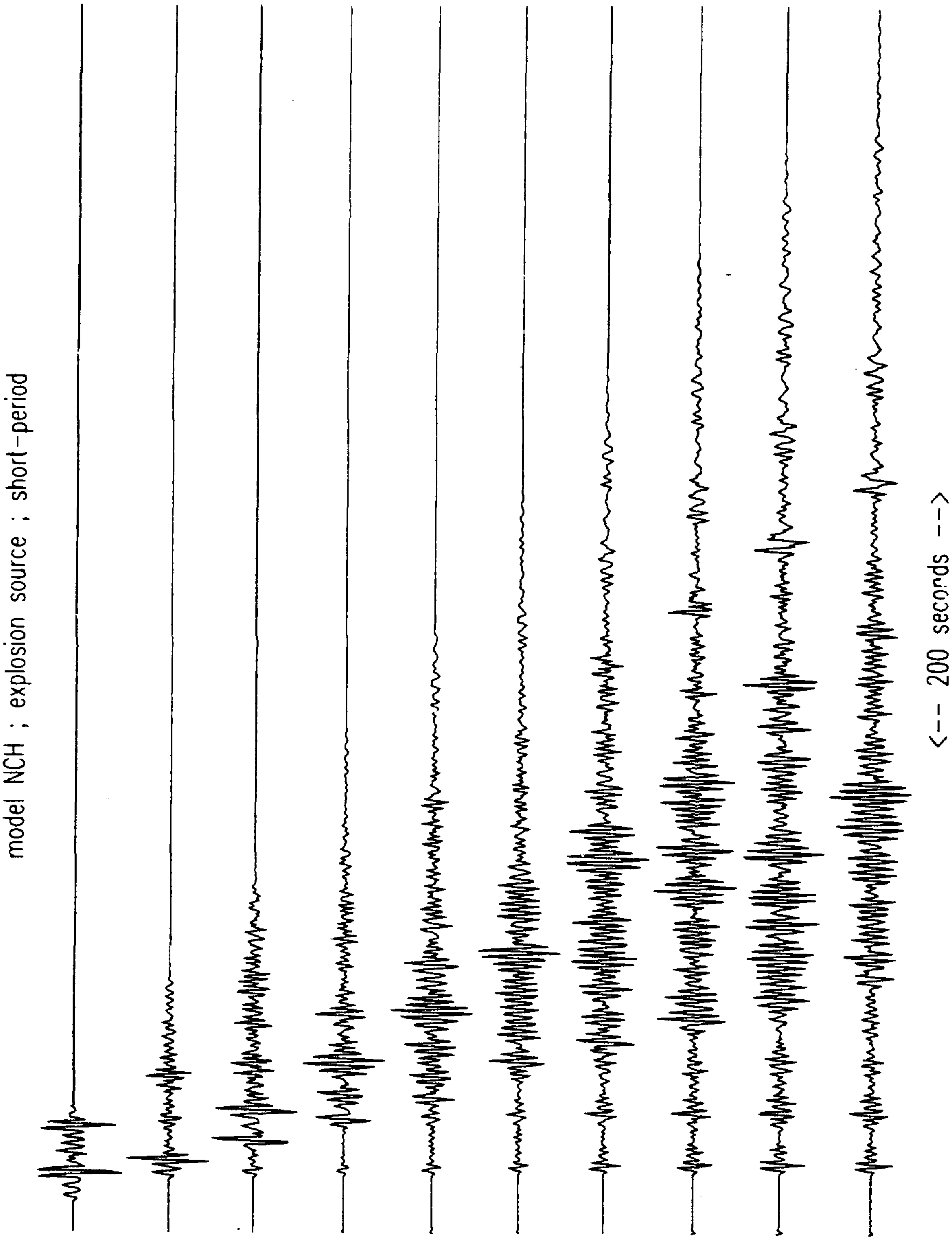
model NCH ; explosion source ; short-period
<-- 200 seconds -->

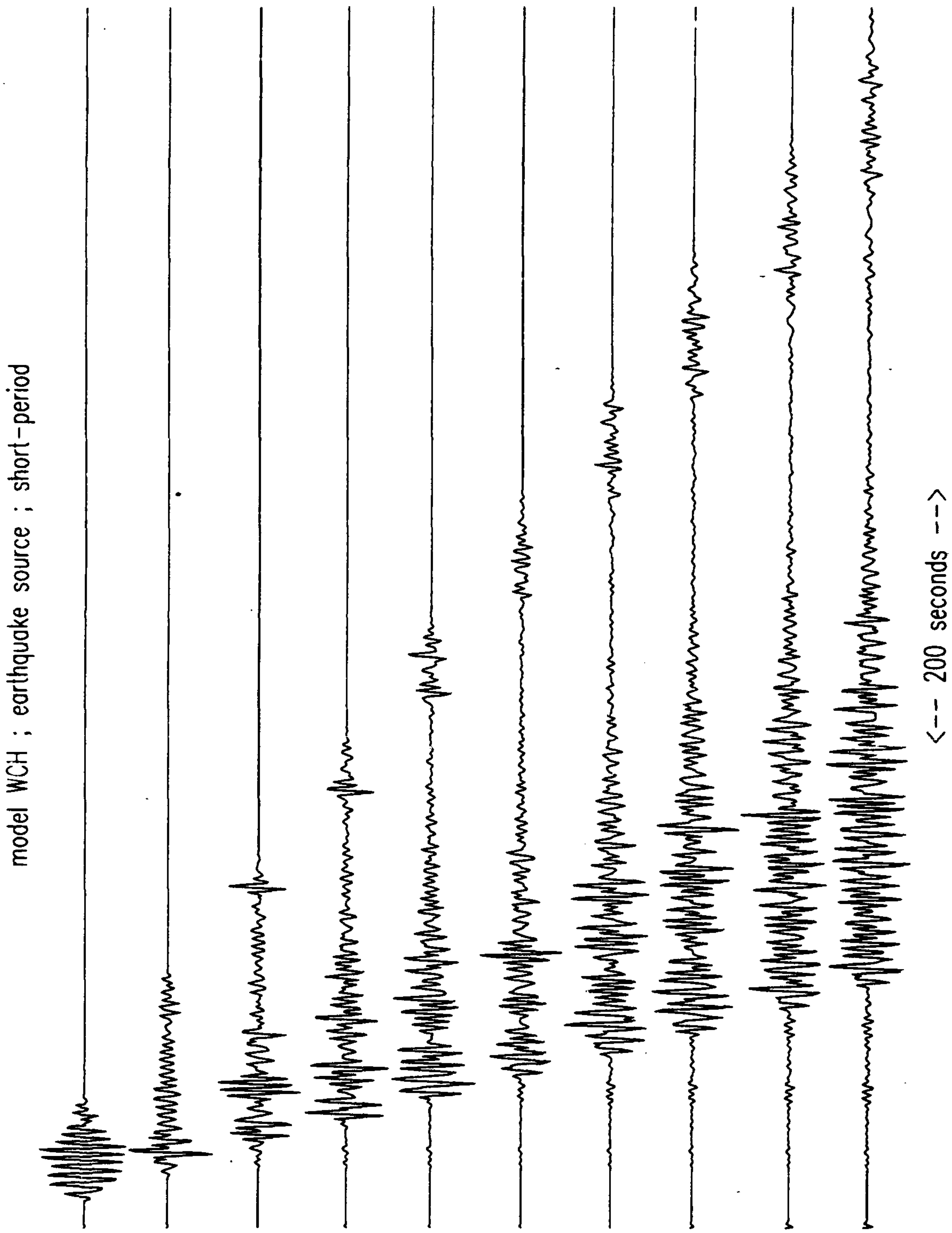
model WCH ; earthquake source ; short-period
<-- 200 seconds -->

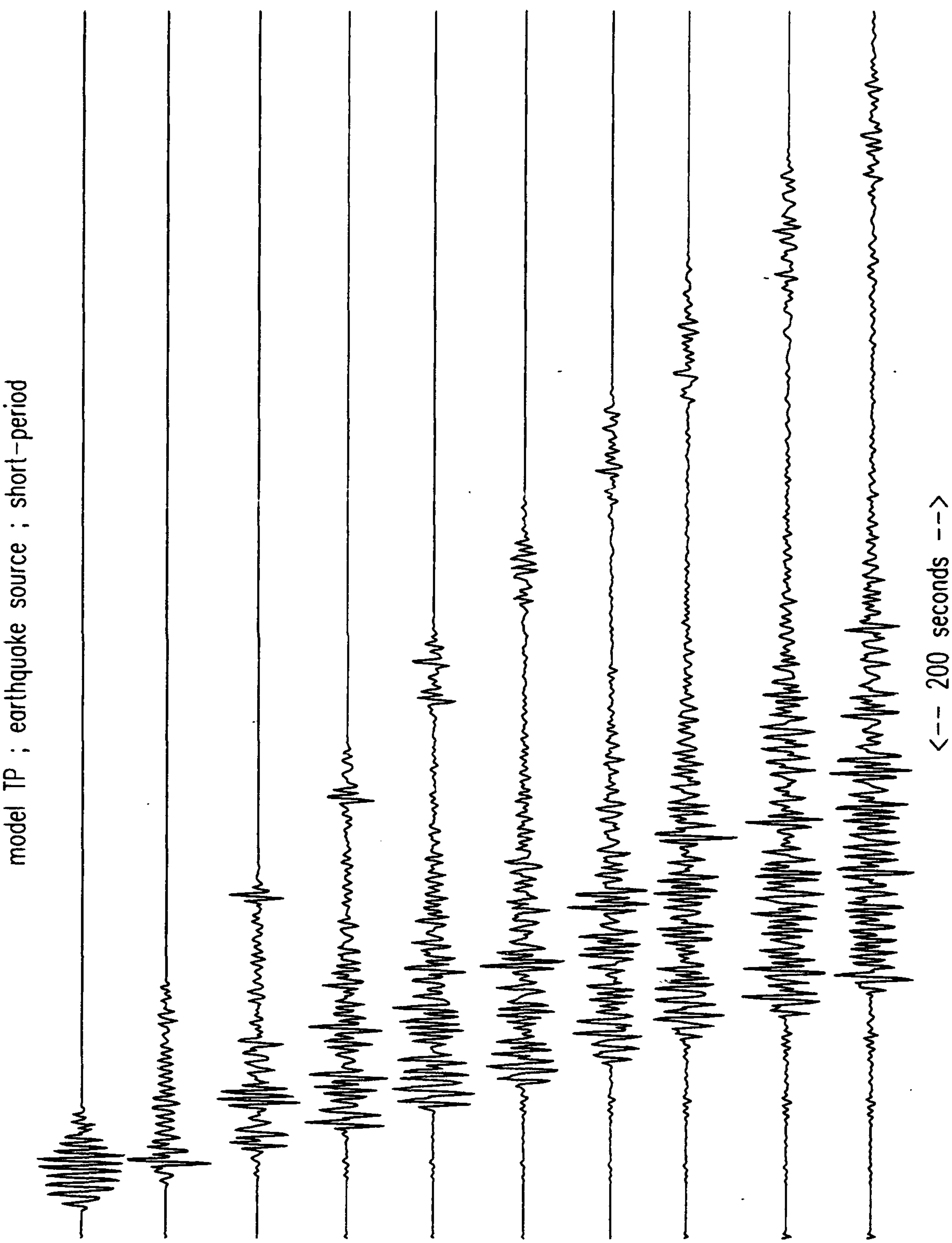
model TP ; earthquake source ; short-period
<-- 200 seconds -->

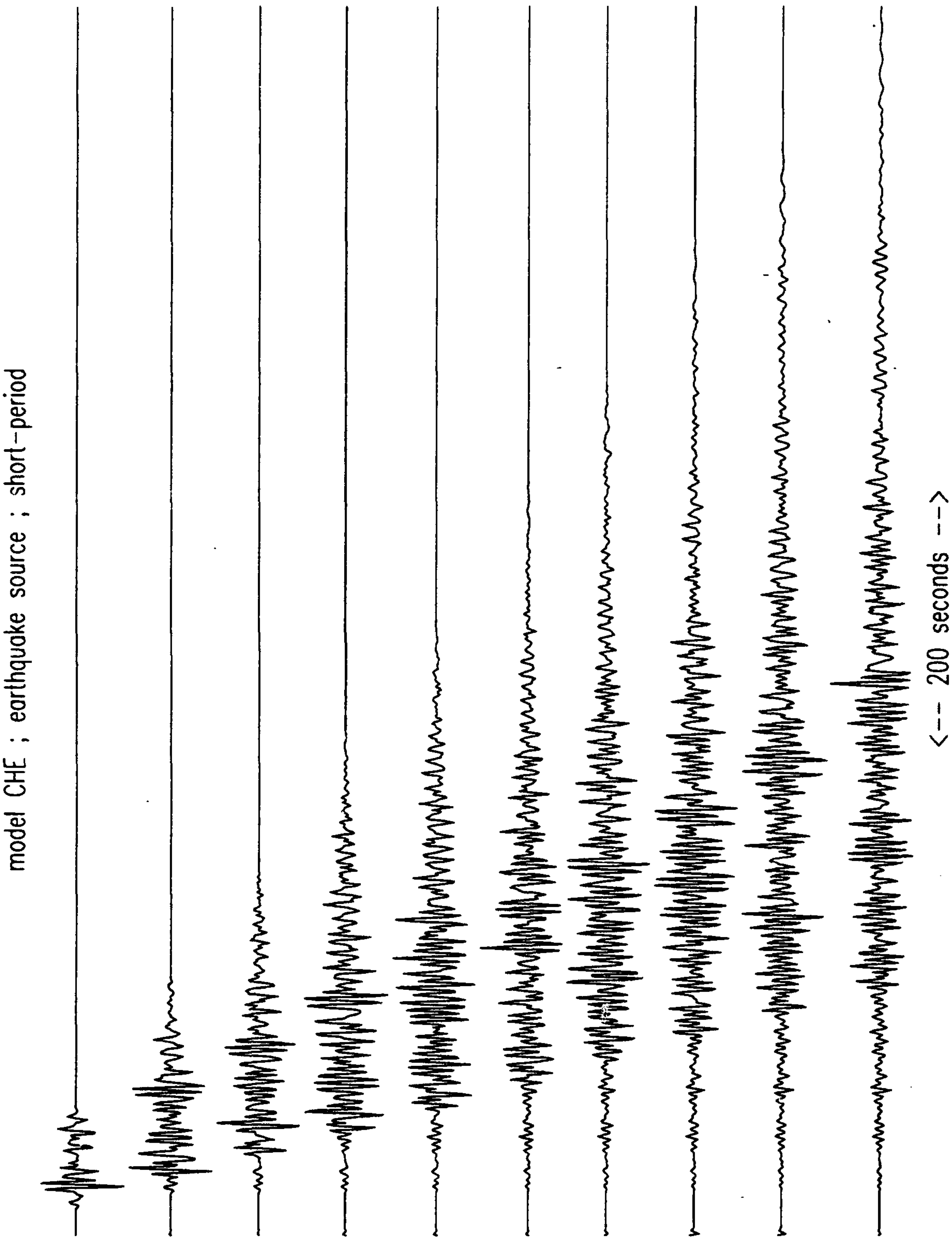
model CHE ; earthquake source ; short-period
<-- 200 seconds -->

model NCH ; earthquake source ; short-period

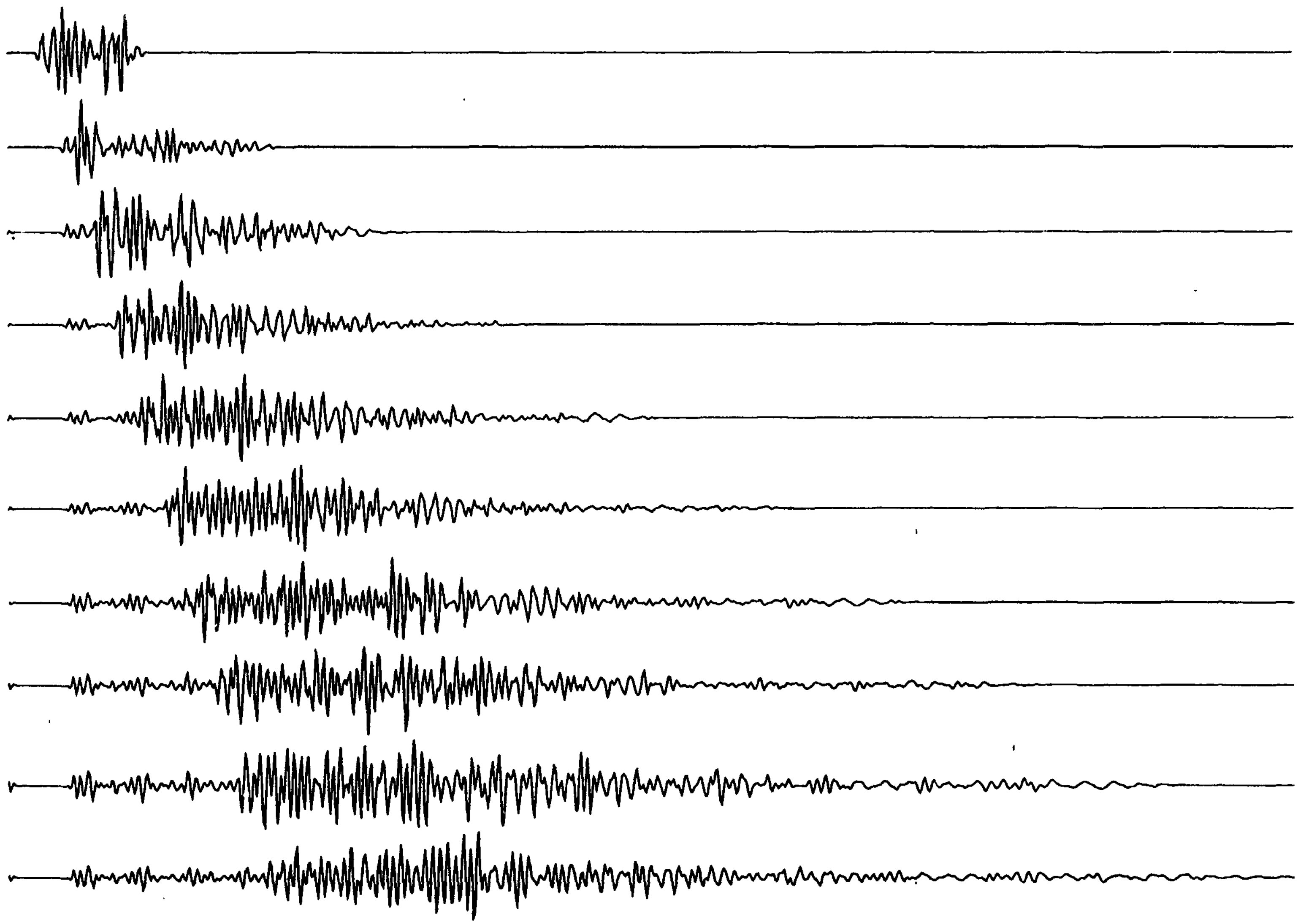

Prof. Thomas Ahrens
Seismological Lab, 252-21
Division of Geological & Planetary Sciences
California Institute of Technology
Pasadena, CA 91125

Prof. Keiiti Aki
Center for Earth Sciences
University of Southern California
University Park
Los Angeles, CA 90089-0741

Prof. Shelton Alexander
Geosciences Department
403 Deike Building
The Pennsylvania State University
University Park, PA 16802

Prof. Charles B. Archambeau
CIRES
University of Colorado
Boulder, CO 80309

Dr. Thomas C. Bache, Jr.
Science Applications Int'l Corp.
10260 Campus Point Drive
San Diego, CA 92121 (2 copies)

Prof. Muawia Barazangi
Institute for the Study of the Continent
Cornell University
Ithaca, NY 14853

Dr. Jeff Barker
Department of Geological Sciences
State University of New York
at Binghamton
Vestal, NY 13901

Dr. Douglas R. Baumgardt
ENSCO, Inc
5400 Port Royal Road
Springfield, VA 22151-2388

Dr. Susan Beck
Department of Geosciences
Building #77
University of Arizona
Tuscon, AZ 85721

Dr. T.J. Bennett
S-CUBED
A Division of Maxwell Laboratories
11800 Sunrise Valley Drive, Suite 1212
Reston, VA 22091

Dr. Robert Blandford
AFTAC/TT, Center for Seismic Studies
1300 North 17th Street
Suite 1450
Arlington, VA 22209-2308

Dr. Stephen Bratt
ARPA/NMRO
3701 North Fairfax Drive
Arlington, VA 22203-1714

Dr. Lawrence Burdick
IGPP, A-025
Scripps Institute of Oceanography
University of California, San Diego
La Jolla, CA 92093

Dr. Robert Burridge
Schlumberger-Doll Research Center
Old Quarry Road
Ridgefield, CT 06877

Dr. Jerry Carter
Center for Seismic Studies
1300 North 17th Street
Suite 1450
Arlington, VA 22209-2308

Dr. Eric Chael
Division 9241
Sandia Laboratory
Albuquerque, NM 87185

Dr. Martin Chapman
Department of Geological Sciences
Virginia Polytechnical Institute
21044 Derring Hall
Blacksburg, VA 24061

Prof. Vernon F. Cormier
Department of Geology & Geophysics
U-45, Room 207
University of Connecticut
Storrs, CT 06268

Prof. Steven Day
Department of Geological Sciences
San Diego State University
San Diego, CA 92182

Marvin Denny
U.S. Department of Energy
Office of Arms Control
Washington, DC 20585

Dr. Zoltan Der
ENSCO, Inc.
5400 Port Royal Road
Springfield, VA 22151-2388

Prof. Adam Dziewonski
Hoffman Laboratory, Harvard University
Dept. of Earth Atmos. & Planetary Sciences
20 Oxford Street
Cambridge, MA 02138

Prof. John Ebel
Department of Geology & Geophysics
Boston College
Chestnut Hill, MA 02167

Eric Fielding
SNEE Hall
INSTOC
Cornell University
Ithaca, NY 14853

Dr. Mark D. Fisk
Mission Research Corporation
735 State Street
P.O. Drawer 719
Santa Barbara, CA 93102

Prof Stanley Flatte
Applied Sciences Building
University of California, Santa Cruz
Santa Cruz, CA 95064

Dr. John Foley
NER-Geo Sciences
1100 Crown Colony Drive
Quincy, MA 02169

Prof. Donald Forsyth
Department of Geological Sciences
Brown University
Providence, RI 02912

Dr. Art Frankel
U.S. Geological Survey
922 National Center
Reston, VA 22092

Dr. Cliff Frolich
Institute of Geophysics
8701 North Mopac
Austin, TX 78759

Dr. Holly Given
IGPP, A-025
Scripps Institute of Oceanography
University of California, San Diego
La Jolla, CA 92093

Dr. Jeffrey W. Given
SAIC
10260 Campus Point Drive
San Diego, CA 92121

Dr. Dale Glover
Defense Intelligence Agency
ATTN: ODT-1B
Washington, DC 20301

Dan N. Hagedon
Pacific Northwest Laboratories
Battelle Boulevard
Richland, WA 99352

Dr. James Hannon
Lawrence Livermore National Laboratory
P.O. Box 808
L-205
Livermore, CA 94550

Prof. David G. Harkrider
Seismological Laboratory
Division of Geological & Planetary Sciences
California Institute of Technology
Pasadena, CA 91125

Prof. Danny Harvey
CIRES
University of Colorado
Boulder, CO 80309

Prof. Donald V. Helmberger
Seismological Laboratory
Division of Geological & Planetary Sciences
California Institute of Technology
Pasadena, CA 91125

Prof. Eugene Herrin
Institute for the Study of Earth and Man
Geophysical Laboratory
Southern Methodist University
Dallas, TX 75275

Prof. Robert B. Herrmann
Department of Earth & Atmospheric Sciences
St. Louis University
St. Louis, MO 63156

Prof. Lane R. Johnson
Seismographic Station
University of California
Berkeley, CA 94720

Prof. Thomas H. Jordan
Department of Earth, Atmospheric &
Planetary Sciences
Massachusetts Institute of Technology
Cambridge, MA 02139

Prof. Alan Kafka
Department of Geology & Geophysics
Boston College
Chestnut Hill, MA 02167

Robert C. Kemerait
ENSCO, Inc.
445 Pineda Court
Melbourne, FL 32940

Dr. Karl Koch
Institute for the Study of Earth and Man
Geophysical Laboratory
Southern Methodist University
Dallas, Tx 75275

Dr. Max Koontz
U.S. Dept. of Energy/DP 5
Forrestal Building
1000 Independence Avenue
Washington, DC 20585

Dr. Richard LaCoss
MIT Lincoln Laboratory, M-200B
P.O. Box 73
Lexington, MA 02173-0073

Dr. Fred K. Lamb
University of Illinois at Urbana-Champaign
Department of Physics
1110 West Green Street
Urbana, IL 61801

Prof. Charles A. Langston
Geosciences Department
403 Deike Building
The Pennsylvania State University
University Park, PA 16802

Jim Lawson, Chief Geophysicist
Oklahoma Geological Survey
Oklahoma Geophysical Observatory
P.O. Box 8
Leonard, OK 74043-0008

Prof. Thorne Lay
Institute of Tectonics
Earth Science Board
University of California, Santa Cruz
Santa Cruz, CA 95064

Dr. William Leith
U.S. Geological Survey
Mail Stop 928
Reston, VA 22092

Mr. James F. Lewkowicz
Phillips Laboratory/GPEH
29 Randolph Road
Hanscom AFB, MA 01731-3010(2 copies)

Mr. Alfred Lieberman
ACDA/VI-OA State Department Building
Room 5726
320-21st Street, NW
Washington, DC 20451

Prof. L. Timothy Long
School of Geophysical Sciences
Georgia Institute of Technology
Atlanta, GA 30332

Dr. Randolph Martin, III
New England Research, Inc.
76 Olcott Drive
White River Junction, VT 05001

Dr. Robert Masse
Denver Federal Building
Box 25046, Mail Stop 967
Denver, CO 80225

Dr. Gary McCartor
Department of Physics
Southern Methodist University
Dallas, TX 75275

Prof. Thomas V. McEvilly
Seismographic Station
University of California
Berkeley, CA 94720

Dr. Art McGarr
U.S. Geological Survey
Mail Stop 977
U.S. Geological Survey
Menlo Park, CA 94025

Dr. Keith L. McLaughlin
S-CUBED
A Division of Maxwell Laboratory
P.O. Box 1620
La Jolla, CA 92038-1620

Stephen Miller & Dr. Alexander Florence
SRI International
333 Ravenswood Avenue
Box AF 116
Menlo Park, CA 94025-3493

Prof. Bernard Minster
IGPP, A-025
Scripps Institute of Oceanography
University of California, San Diego
La Jolla, CA 92093

Prof. Brian J. Mitchell
Department of Earth & Atmospheric Sciences
St. Louis University
St. Louis, MO 63156

Mr. Jack Murphy
S-CUBED
A Division of Maxwell Laboratory
11800 Sunrise Valley Drive, Suite 1212
Reston, VA 22091 (2 Copies)

Dr. Keith K. Nakanishi
Lawrence Livermore National Laboratory
L-025
P.O. Box 808
Livermore, CA 94550

Prof. John A. Orcutt
IGPP, A-025
Scripps Institute of Oceanography
University of California, San Diego
La Jolla, CA 92093

Prof. Jeffrey Park
Kline Geology Laboratory
P.O. Box 6666
New Haven, CT 06511-8130

Dr. Howard Patton
Lawrence Livermore National Laboratory
L-025
P.O. Box 808
Livermore, CA 94550

Dr. Frank Pilotte
HQ AFTAC/TT
130 South Highway A1A
Patrick AFB, FL 32925-3002

Dr. Jay J. Pulli
Radix Systems, Inc.
201 Perry Parkway
Gaithersburg, MD 20877

Dr. Robert Reinke
ATTN: FCTVTD
Field Command
Defense Nuclear Agency
Kirtland AFB, NM 87115

Prof. Paul G. Richards
Lamont-Doherty Geological Observatory
of Columbia University
Palisades, NY 10964

Mr. Wilmer Rivers
Teledyne Geotech
314 Montgomery Street
Alexandria, VA 22314

Dr. Alan S. Ryall, Jr.
ARPA/NMRO
3701 North Fairfax Drive
Arlington, VA 22209-1714

Dr. Richard Sailor
TASC, Inc.
55 Walkers Brook Drive
Reading, MA 01867

Prof. Charles G. Sammis
Center for Earth Sciences
University of Southern California
University Park
Los Angeles, CA 90089-0741

Prof. Christopher H. Scholz
Lamont-Doherty Geological Observatory
of Columbia University
Palisades, NY 10964

Dr. Susan Schwartz
Institute of Tectonics
1156 High Street
Santa Cruz, CA 95064

Secretary of the Air Force
(SAFRD)
Washington, DC 20330

Office of the Secretary of Defense
DDR&E
Washington, DC 20330

Thomas J. Sereno, Jr.
Science Application Int'l Corp.
10260 Campus Point Drive
San Diego, CA 92121

Dr. Michael Shore
Defense Nuclear Agency/SPSS
6801 Telegraph Road
Alexandria, VA 22310

Dr. Robert Shumway
University of California Davis
Division of Statistics
Davis, CA 95616

Dr. Matthew Sibol
Virginia Tech
Seismological Observatory
4044 Derring Hall
Blacksburg, VA 24061-0420

Prof. David G. Simpson
IRIS, Inc.
1616 North Fort Myer Drive
Suite 1050
Arlington, VA 22209

Donald L. Springer
Lawrence Livermore National Laboratory
L-025
P.O. Box 808
Livermore, CA 94550

Dr. Jeffrey Stevens
S-CUBED
A Division of Maxwell Laboratory
P.O. Box 1620
La Jolla, CA 92038-1620

Lt. Col. Jim Stobie
ATTN: AFOSR/NL
110 Duncan Avenue
Bolling AFB
Washington, DC 20332-0001

Prof. Brian Stump
Institute for the Study of Earth & Man
Geophysical Laboratory
Southern Methodist University
Dallas, TX 75275

Prof. Jeremiah Sullivan
University of Illinois at Urbana-Champaign
Department of Physics
1110 West Green Street
Urbana, IL 61801

Prof. L. Sykes
Lamont-Doherty Geological Observatory
of Columbia University
Palisades, NY 10964

Dr. David Taylor
ENSCO, Inc.
445 Pineda Court
Melbourne, FL 32940

Dr. Steven R. Taylor
Los Alamos National Laboratory
P.O. Box 1663
Mail Stop C335
Los Alamos, NM 87545

Prof. Clifford Thurber
University of Wisconsin-Madison
Department of Geology & Geophysics
1215 West Dayton Street
Madison, WS 53706

Prof. M. Nafi Toksoz
Earth Resources Lab
Massachusetts Institute of Technology
42 Carleton Street
Cambridge, MA 02142

Dr. Larry Turnbull
CIA-OSWR/NED
Washington, DC 20505

Dr. Gregory van der Vink
IRIS, Inc.
1616 North Fort Myer Drive
Suite 1050
Arlington, VA 22209

Dr. Karl Veith
EG&G
5211 Auth Road
Suite 240
Suitland, MD 20746

Prof. Terry C. Wallace
Department of Geosciences
Building #77
University of Arizona
Tuscon, AZ 85721

Dr. Thomas Weaver
Los Alamos National Laboratory
P.O. Box 1663
Mail Stop C335
Los Alamos, NM 87545

Dr. William Wortman
Mission Research Corporation
8560 Cinderbed Road
Suite 700
Newington, VA 22122

Prof. Francis T. Wu
Department of Geological Sciences
State University of New York
at Binghamton
Vestal, NY 13901

ARPA, OASB/Library
3701 North Fairfax Drive
Arlington, VA 22203-1714

HQ DNA
ATTN: Technical Library
Washington, DC 20305

Defense Intelligence Agency
Directorate for Scientific & Technical Intelligence
ATTN: DTIB
Washington, DC 20340-6158

Defense Technical Information Center
Cameron Station
Alexandria, VA 22314 (2 Copies)

TACTEC
Battelle Memorial Institute
505 King Avenue
Columbus, OH 43201 (Final Report)

Phillips Laboratory
ATTN: XPG
29 Randolph Road
Hanscom AFB, MA 01731-3010

Phillips Laboratory
ATTN: GPE
29 Randolph Road
Hanscom AFB, MA 01731-3010

Phillips Laboratory
ATTN: TSML
5 Wright Street
Hanscom AFB, MA 01731-3004

Phillips Laboratory
ATTN: PL/SUL
3550 Aberdeen Ave SE
Kirtland, NM 87117-5776 (2 copies)

Dr. Michel Bouchon
I.R.I.G.M.-B.P. 68
38402 St. Martin D'Heres
Cedex, FRANCE

Dr. Michel Campillo
Observatoire de Grenoble
I.R.I.G.M.-B.P. 53
38041 Grenoble, FRANCE

Dr. Kin Yip Chun
Geophysics Division
Physics Department
University of Toronto
Ontario, CANADA

Prof. Hans-Peter Harjes
Institute for Geophysic
Ruhr University/Bochum
P.O. Box 102148
4630 Bochum 1, GERMANY

Prof. Eystein Husebye
NTNF/NORSAR
P.O. Box 51
N-2007 Kjeller, NORWAY

David Jepsen
Acting Head, Nuclear Monitoring Section
Bureau of Mineral Resources
Geology and Geophysics
G.P.O. Box 378, Canberra, AUSTRALIA

Ms. Eva Johannisson
Senior Research Officer
FOA
S-172 90 Sundbyberg, SWEDEN

Dr. Peter Marshall
Procurement Executive
Ministry of Defense
Blacknest, Brimpton
Reading FG7-FRS, UNITED KINGDOM

Dr. Bernard Massinon, Dr. Pierre Mechler
Societe Radiomana
27 rue Claude Bernard
75005 Paris, FRANCE (2 Copies)

Dr. Svein Mykkeltveit
NTNT/NORSAR
P.O. Box 51
N-2007 Kjeller, NORWAY (3 Copies)

Prof. Keith Priestley
University of Cambridge
Bullard Labs, Dept. of Earth Sciences
Madingley Rise, Madingley Road
Cambridge CB3 OEZ, ENGLAND

Dr. Jorg Schlittenhardt
Federal Institute for Geosciences & Nat'l Res.
Postfach 510153
D-30631 Hannover , GERMANY

Dr. Johannes Schweitzer
Institute of Geophysics
Ruhr University/Bochum
P.O. Box 1102148
4360 Bochum 1, GERMANY

Trust & Verify
VERTIC
8 John Adam Street
London WC2N 6EZ, ENGLAND